AD-A064 389 JOHNS HOPKINS UNIV LAUREL MD APPLIED PHYSICS LAB F/G 5/2
DEVELOPMENTS IN SCIENCE AND TECHNOLOGY.(U)
1977 N00017-72-C-4401
UNCLASSIFIED APL/JHU/DST-5 NL

1 OF 2
AD A064389

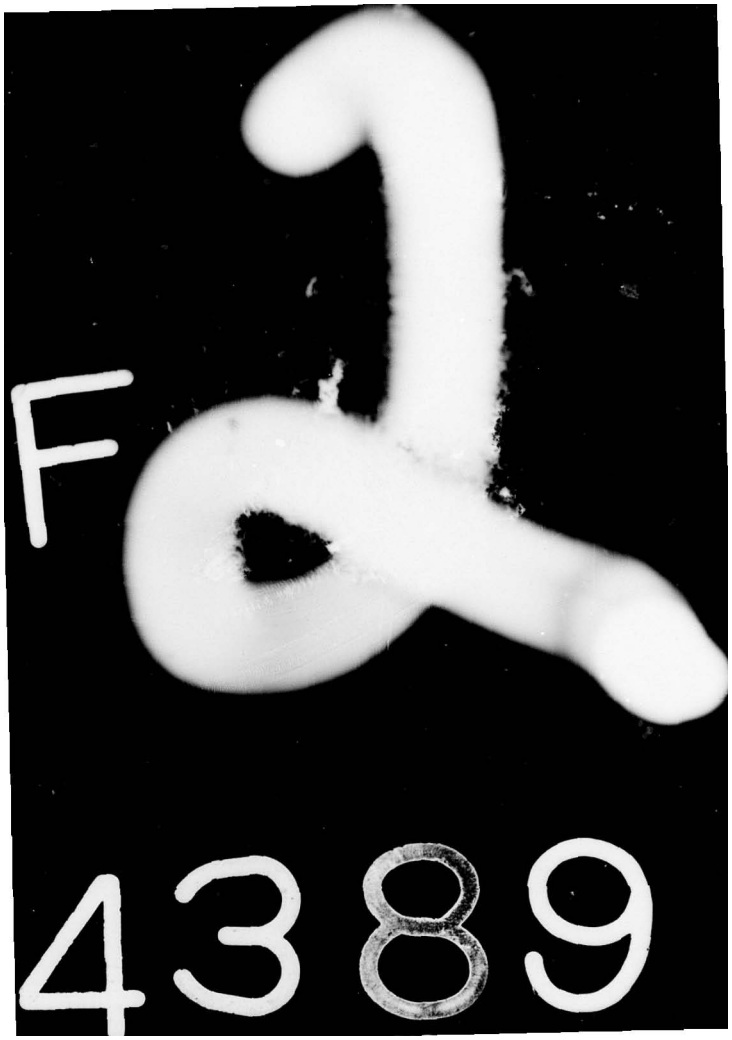
F
4389

APL/JHU DST-5
FISCAL YEAR 1977

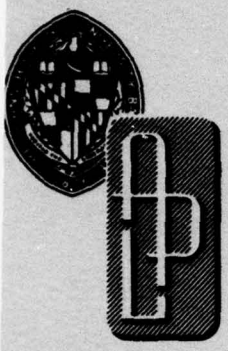

APPLIED PHYSICS LABORATORY

DEVELOPMENTS IN SCIENCE AND TECHNOLOGY

Approved for public release; distribution unlimited.

THE JOHNS HOPKINS UNIVERSITY • APPLIED PHYSICS LABORATORY
Johns Hopkins Road, Laurel, Maryland 20810
Operating under Contract N00017-72-C-4401 with the Department of the Navy

(14) APL/JHU/DST-5
FISCAL YEAR 1977

(11) 1977

APPLIED PHYSICS LABORATORY

(6) # DEVELOPMENTS IN SCIENCE AND TECHNOLOGY.

(12) 121 p.

Approved for public release; distribution unlimited.

THE JOHNS HOPKINS UNIVERSITY • APPLIED PHYSICS LABORATORY
Johns Hopkins Road, Laurel, Maryland 20810
Operating under Contract N00017-72-C-4401 with the Department of the Navy
(15)

FOREWORD

The Applied Physics Laboratory (APL) of The Johns Hopkins University, with field activities in Florida, Utah, New Mexico, Virginia, New Jersey, California, and Heidelberg, Germany, is located in Howard County, Maryland, midway between Baltimore and Washington. Its work is carried out under a contractual agreement between the University and the Government, with about 80% of the effort devoted to the Department of the Navy. APL employs a staff of about 2400, more than 1200 of whom are professional scientists and engineers. Their ideas are implemented and extended through a network of associate contractors from coast to coast.

The primary mission of APL is to serve the nation through the application of advanced science and technology to the solution of problems of importance in both the defense and the civil sectors. APL conducts board programs in basic and applied research, exploratory and advanced development, component engineering, systems engineering and integration, and test and evaluation of operating systems.

The Laboratory was established in 1942 at the urgent request of the Office of Scientific Research and Development to demonstrate that science and technology could advance national security more effectively through an active partnership of military and civilian technologists than through the traditional buyer-supplier relationship. The concept was validated in less than a year when APL developed the first practical VT (variable time) fuze. This initial product proved to be a major contributor to the Allied victory in World War II.

After the war, at the request of the Secretary of the Navy, the University trustees agreed to continue the Laboratory as an important national security resource. APL quickly became a leader in guided missile and space technology as well as a contributor to fundamental knowledge in such areas as high-altitude physics, spectroscopy, flame propagation, the origin and evolution of the universe, supersonic and hypersonic aerodynamics, chemical kinetics, and magnetic resonance.

In addition to major contributions to national defense, effort is increasingly devoted to the solution of pressing problems in the civilian sector. A few examples of the areas to which attention has been devoted in recent years are biomedical research and engineering; transportation; fire research; pollution of the biosphere; energy, including ocean thermal, geothermal, and community storage; navigation satellite technology; leak detection in natural gas distribution lines; computer technology; and advanced education.

In its role as a University laboratory, APL performs research to advance the basic sciences underlying its technological development programs. In this area, APL has significantly contributed to Johns Hopkins' 100-year-old reputation for leadership and originality. Through unique applications of systems engineering, science, and technology to the needs of society, APL has enhanced the University's tradition of excellence while gaining worldwide recognition of its own.

This report contains a representative sample of APL technical accomplishments, primarily in the civil area. All results of these programs are fully available to the public.

during fiscal year 1977;

Subject areas include: Space Science and Technology; Biomedical Systems;

(cont on p. 8)

CONTENTS

SPACE SCIENCE AND TECHNOLOGY

BIOMEDICAL SYSTEMS

URBAN TECHNOLOGY

OCEAN SCIENCE AND TECHNOLOGY

ENERGY RESEARCH AND DEVELOPMENT

FUNDAMENTAL RESEARCH

JHU EVENING COLLEGE CENTER AT APL

PATENTS

PUBLICATIONS AND PRESENTATIONS 119

AUTHOR INDEX 130

SPACE SCIENCE AND TECHNOLOGY

INTRODUCTION

The Laboratory's involvement in space programs began in the postwar years when V-2 and Aerobee rockets carried Geiger tubes, magnetometers, and optical spectrometers high above the earth's surface. The flights provided the first high-altitude measurements of cosmic rays, the geomagnetic field, and atmospheric constituents such as ozone, and were conducted by pioneers James A. Van Allen, John J. Hopfield, and S. Fred Singer (who were then APL staff members). From these distinguished beginnings, the APL record of accomplishments includes the conception, design, and development of the Satellite Doppler Navigational System for the Navy.

The satellite activities spawned a multitude of "firsts" by APL, including development of the first gravity-gradient satellite, the first photographs (in black and white and in color) of the entire earth from synchronous satellites, the first solid-state particle detectors flown on a satellite, and the first extremely accurate measurements of the geomagnetic field.

The Space Development Department of APL has continued to maintain a strong balance between the development of spacecraft systems and hardware and basic research activities directed toward an understanding of the earth and the solar system. This applied and research expertise has been manifested in the past year with the successful launch of the APL-built TRANSAT satellite (designed to test elements of the U.S. Navy's Satellite Missile Tracking (SATRACK) System) and the launches of the Voyagers 1 and 2 spacecraft, bound for Jupiter and Saturn, carrying APL scientific experiments to measure charged particles in the solar system.

Research programs included scholarly investigations of ancient astronomical records, which led to the suggestion that Ptolemy was a fraud; the discovery of plasma acceleration regions behind the earth that can generate charged particles with energies up to hundreds of thousands of electron volts; investigation of the interaction between the interplanetary magnetic field and the geomagnetic field (a possible link between solar activity and terrestrial weather); and the discovery of the fact that Jupiter is a prominent source of

energetic particles in the vicinity of the earth (they previously were thought to originate in the sun).

While contributing to a fundamental understanding of the physical and chemical processes that occur in the vast region from the earth's upper atmosphere to the distant planets, APL staff members have advanced the state of the art of a wide variety of spacecraft instruments, from complete satellites (including attitude control and microprocessor systems) to complex scientific detectors. For example, the energetic particle detectors on board the Voyager spacecraft (which were designed, tested, and constructed at APL) are more complicated than the entire Mariner IV spacecraft that traveled to Mars.

NASA has selected scientists and engineers from APL to participate in a record number of interplanetary missions. (These missions include Voyagers 1 and 2, which will rendezvous with Jupiter in 1979; Galileo, which is scheduled to orbit Jupiter; and Solar Polar, which will orbit over the poles of the sun.) Support for the joint APL/Max-Planck Institute Active Magnetospheric Particle Tracer Experiment (AMPTE) was confirmed this year by NASA and the Federal Republic of Germany. The purpose of the experiment is to create an artificial ion cloud outside the earth's magnetosphere in order to investigate the mechanisms responsible for the formation of the Van Allen radiation belts (an appropriate study linked with the pioneering activities of Van Allen at APL).

In the incredibly short period of a few weeks, an energetic electron detector was designed, assembled, and tested at APL and successfully launched on the NASA International Ultraviolet Explorer (IUE) spacecraft this year. APL is presently building for NASA an earth-orbiting satellite called MAGSAT, to measure the earth's magnetic field with an accuracy not previously available on a worldwide basis. APL has also built principal instruments for the SEASAT satellite that will measure the general characteristics of the oceans on a global scale in all weather conditions.

TRANSAT TRANSLATOR

A translator has been designed, using microelectronic packaging techniques, to translate two UHF input spectra and a tracking aid ("pilot carrier") to a wideband spectrum at S band for retransmission to ground receivers. The translator has been incorporated into a Navy Navigation Satellite. The combination, known as TRANSAT, will provide a means for early checkout of surface stations and data-processing facilities of the Satellite Missile Tracking (SATRACK) System now being developed and evaluated at APL.

BACKGROUND

Designed to work with a constellation of Global Positioning Satellites (GPS) that transmit signals at 1575.42 MHz, the missile-borne translator tracks the signals by range difference and doppler methods. The translator also receives signals at 393.855 MHz from a ground transmitter. This lower-frequency signal is used to measure the ionospheric electron density as the missile transits the ionosphere; it is also used as a range safety signal. The spectra of these two signals, along with a pilot carrier signal derived from the translator's local oscillator, are translated to 2273.5 MHz (S band) and transmitted to tracking ground stations. Figure 1 illustrates the system.

By orbiting the translator as an add-on to a satellite, a permanent test vehicle will be available to simulate a Trident missile flight each orbit. Since the satellite chosen in this case is a Navy Navigation Satellite, it can be commanded to its normal navigation mode when the translator is not in use.

For redundancy, two translators were designed, space qualified, and incorporated into a penthouse structure on the satellite. Either may be activated by ground command.

DISCUSSION

Under ground station control, a translator is selected and commanded ON. The 2273.5–MHz signal is transmitted through four antennas mounted on four booms equally spaced around the diameter of the satellite. After 15 minutes, the translator will automatically turn off. However, an OFF command from the ground station will turn it off regardless of where it is in the ON cycle.

The translator is shown in Fig. 2, and Fig. 3 is a block diagram indicating the basic operation.

Design ranges for input signals for both the 393.855– and 1575.42–MHz channels (channels 1 and 2, respectively) are between −130 and −60 dBm. The channel 1 signal is amplified and mixed with a local oscillator (LO) derived from a 5–MHz source to provide 25.855 MHz at the summing amplifier. Likewise, channel 2 is heterodyned to 28.42 MHz. In order to aid the tracking of these signals, a pilot carrier is also added at the summing amplifier. This 25–MHz signal is coherent with the other LO signals since it is derived from the same 5–MHz temperature-compensated crystal oscillator.

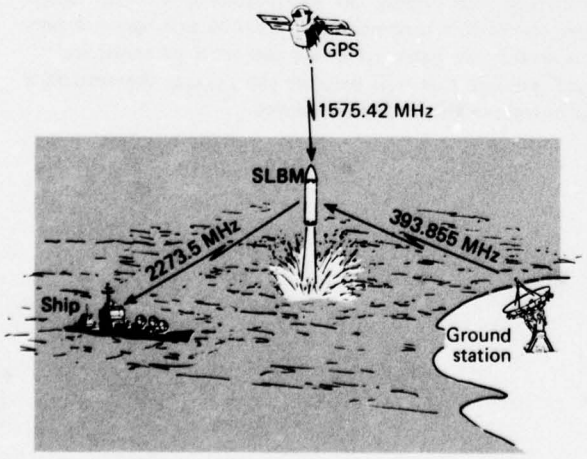

Fig. 1 The SATRACK system.

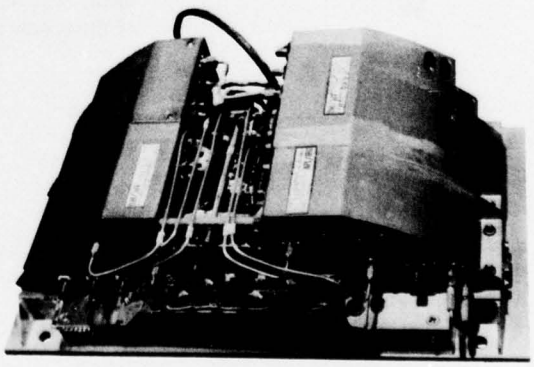

Fig. 2 The TRANSAT translator.

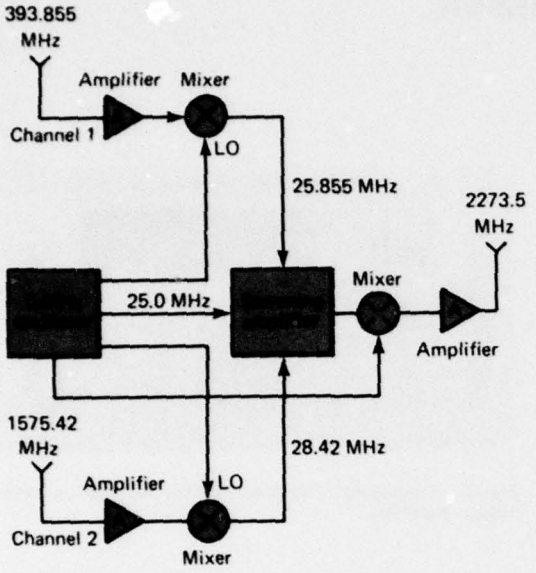

Fig. 3 Block diagram of the translator.

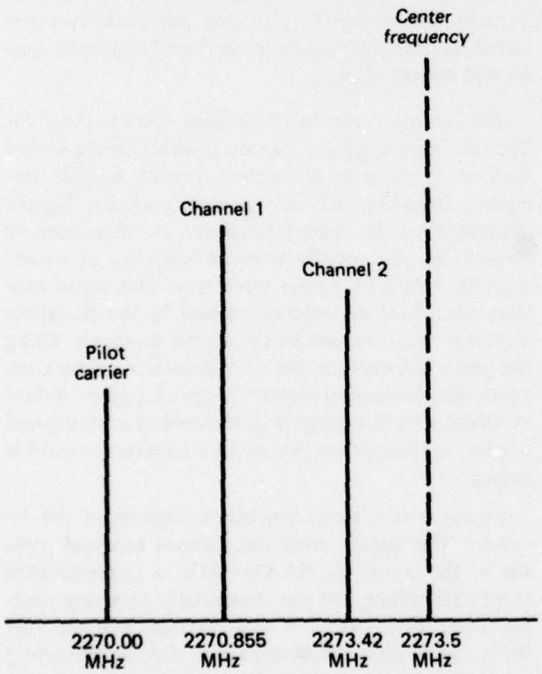

Fig. 4 Output spectrum of the translator.

Subsequent mixing and amplification results in the composite spectrum at the summing amplifier output being translated to S band with the spectral pattern shown in Fig. 4 and a power level of −3 dBm.

Frequency synthesis by phase-locked loop techniques was used to derive the mixing, or LO, signals. This allowed the use of off-the-shelf integrated circuits with resultant savings in power and space.

The output power requirements of the translator were 5 W (37 dBm) with 30-dB intermodulation distortion products. Intermodulation distortion of this magnitude at high power levels is difficult to obtain when weight and volume are at a premium. Since a gain of 40 dB (−3 to 37 dBm) was required, the output power amplifier was divided into two sections: a low-level section, −3 to 20 dBm, consisting of four stages, and a high-level section, 20 to 37 dBm, consisting of a hybrid two-stage amplifier. It was difficult to meet the intermodulation requirement in the high-level stages and some new development was required. The final device consisted of three RF transistors in a series/parallel hybrid configuration. Each transistor consisted of a five-cell pellet from adjacent areas of the original silicon wafer. The typical power output from the transistors was 2.9 to 3.2 W at 30-dB intermodulation distortion. Temperature-compensated bias networks provided linearized class B operation for the common-base configuration.

To provide a means for evaluating overall translator performance, several power levels and temperatures were telemetered from the spacecraft to ground tracking stations. The parameters included power supply current, input signal levels, temperatures, and output power.

Because of the space and weight constraints of the satellite, microelectronic packaging techniques were used to the fullest. Modular construction consisted of several Kovar chemical milled chassis. Active circuits utilized microstrip substrates and miniature chip components. Therefore, both electrical isolation and the mechanical integrity dictated by the spacecraft launch environment were achieved.

TRANSAT has passed all electrical and environmental tests at APL under vibration and thermal-vacuum conditions. It was shipped to Vandenburg Air Force Base for launch on a Scout D rocket scheduled for early October 1977.

Author: *C. S. Morris*

Support: *Strategic Systems Projects Office*

RF SYSTEM FOR THE TIME-TRANSFER RECEIVER OF THE NAVIGATION TECHNOLOGY SATELLITE

An RF system has been designed and developed for a timing receiver that NASA will use to obtain global submicrosecond timing. The compact, low-cost receiver passively receives sidetone ranging signals from the Navigation Technology Satellite (NTS) and, under the control of a microprocessor, is capable of a precision of better than 0.5 μs. It is potentially useful to anyone with a need for an inexpensive time-transfer capability.

BACKGROUND

The NASA Goddard Space Flight Center (GSFC) Laser Tracking Network, currently being implemented, requires worldwide clock synchronization of ±1 μs. Recognizing that this precision is not achievable by conventional time-transfer systems such as Loran C or by extended portable clock trips, GSFC initiated the development of a single-frequency time-transfer receiver to provide suitable remote-clock synchronization data. Using ranging signals from the NTS, the receiver will provide NASA with timing data into the early 1980's. Among the non-NASA users are other United States Governmental agencies and several foreign countries.

The NTS receiver is the result of a joint development effort by APL and the Naval Surface Weapons Center (NSWC), Dahlgren, Virginia. NSWC was responsible for the digital and processor portions and the mainframe chassis. The RF and analog portions were designed and developed by APL.

DISCUSSION

The NTS receiver (Fig. 1) operates automatically under the control of an Intel 8080 microprocessor. Using ranging sidetones transmitted by the spacecraft, it provides an "observed" measurement of the spacecraft-to-receiver range in time units, once each minute that the spacecraft is in view.

To convert the range output by the receiver to useful clock error measurements, further non-real-time processing is required. Conceptually, the observed range may be compared with a theoretical range based on known ground and spacecraft positions to yield an error that is relatable to the real difference between a spacecraft clock and a ground station clock. In actual practice, however, similar measurements are made at two sites, a reference site with a "master" clock and a remote site whose relative clock time is in question. If the two observations are made as closely in time as possible, the spacecraft clock may effectively be eliminated and the comparison made directly between master and remote clocks.

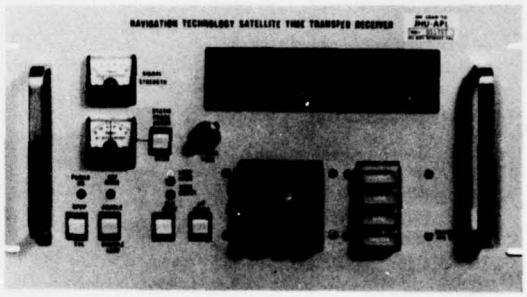

Fig. 1 Time-transfer receiver for the Navigation Technology Satellite.

The receiver comprises three basic systems (Fig. 2). The RF system uses a carrier tracking phase-locked loop as a reference to remove carrier doppler frequency from the received ranging sidetones. Signals generated by the digital processor are then used to convert the sequentially received sidetones to a common 30-kHz TTL square waveform. This signal contains the phase information carried by the successive sidetones and extracted by the digital processor. Using the phase information, the microprocessor system computes the observed spacecraft range at a given instant of GMT, and this range is distributed to a front-panel display, a Teletype output, and a computer-compatible output.

Figure 3 is a simplified block diagram of the RF system. The signals from the antenna terminals consist of the carrier at 335.355 MHz, a reference tone at 335.325 MHz, and ten sequentially occurring ranging tones from 335.324 900 through 328.925 000 MHz. Each signal may contain a doppler frequency offset. In the RF section, the band of frequencies is amplified and converted to an intermediate frequency (IF) in which the tracked component doppler frequency is reduced by nine-tenths.

In the IF section, a 9-MHz bandpass filter establishes the IF bandwidth, and automatic gain control

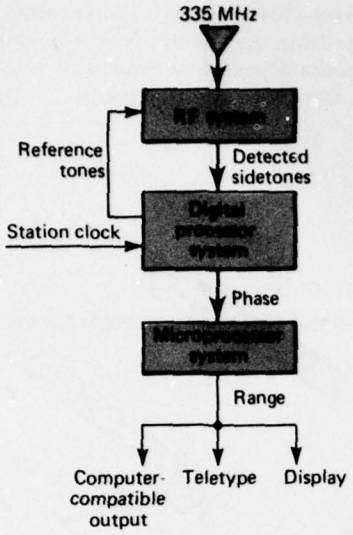

Fig. 2 Block diagram of the NTS time-transfer receiver.

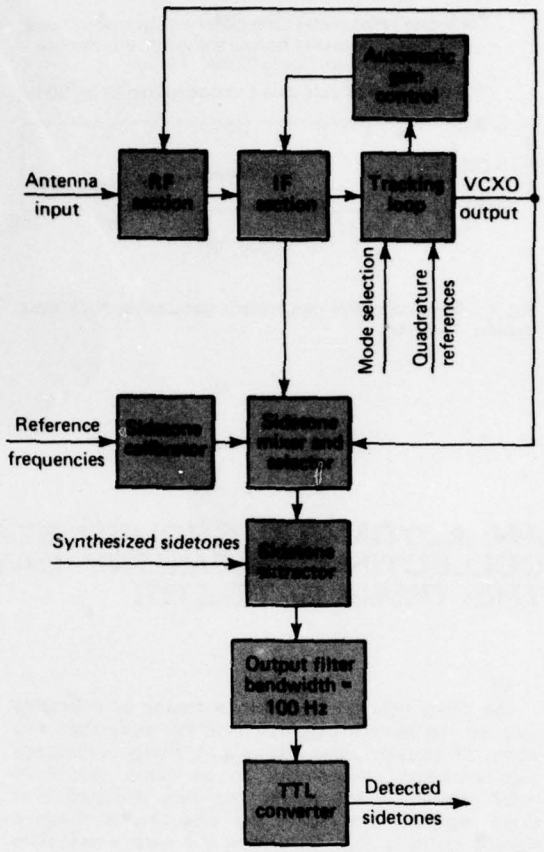

Fig. 3 RF system of NTS time-transfer receiver.

(AGC) is applied to the composite signal. The tracking loop, which operates with a 30-Hz (double sided) bandwidth, supplies a frequency reference to the sidetone mixer and selector, where carrier doppler frequency is removed from the sidetones, which are shifted to near-baseband frequencies. The tracking loop also supplies AGC voltage by using quadrature references from the digital system.

Synthesized sidetones generated by the digital system are used in a combination of double- and single-sideband techniques by the sidetone extractor to convert the received sidetones to 30 kHz. The sidetones are filtered through a 100-Hz bandpass filter and detected by a threshold-crossing TTL converter. To permit checkout of the digital processor, a circuit for generating calibration sidetones has been included.

The RF system is capable of operating in two modes: in one, the continuous carrier is tracked; in the other, the system tracks the reference tone, which is present only during the burst of ranging sidetones. In either of these modes, the tracking loop voltage-controlled crystal oscillator (VCXO) may be tuned manually or automatically by the microprocessor for rapid acquisition.

The receiver has a system noise temperature of approximately 600 K. This permits a tracking loop tracking threshold sensitivity (about +3 dB signal-to-noise ratio) of about −153 dBm. However, because of the wider sidetone filter, the data signal-to-noise ratio is 0 dB at about −151 dBm.

Several months of data have been taken by NTS receivers over the past year. The data shown in Fig. 4 are representative of the receiver's performance. The figure shows the clock error measured between a master clock at the NRL tracking station at Chesapeake Beach, Maryland, and a remote clock at the NASA tracking station at Kennedy Space Center in Florida. The data were taken between days 233 and 268 of 1977. Data points show the determined error in the NASA clock for the minute during each day's pass that the spacecraft was at the minimum range from the receiver. At minimum range, the errors arising from spacecraft motion and atmospheric effects are minimum. No corrections have been made for these effects, nor have other corrections been made to provide greater accuracy. However, the rms value of

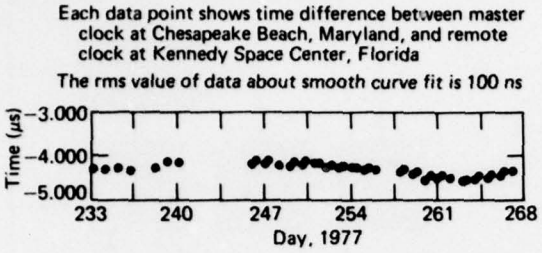

Fig. 4 Representative clock error data using NTS time-transfer receiver.

the data about a best-fit curve is approximately 100 ns. Similar data taken over shorter periods processed with updated spacecraft trajectory predictions have yielded rms values about one-half that amount.

Author: *G. G. Whitworth*

Support: *NASA Goddard Space Flight Center*

AN AUTOMATIC GROUND STATION FOR COLLECTING TELEMETRY DATA FROM THE TRIAD SATELLITE

The Triad satellite has been a means of collecting data on the earth's magnetic field for more than five years. Its circular polar orbit allows nearly continuous high-resolution observations to be made over both polar regions of the earth. The data acquired over these regions have led to the discovery of massive electric currents that flow along the earth's magnetic field lines into and away from the auroral regions. A completely automatic ground station has been designed, constructed, and tested for the unattended collection of telemetry data from Triad. This system represents a third-generation improvement over stations now operating in Resolute, Canada, and McMurdo, Antarctica, to collect Triad data in the North and South Polar regions.

BACKGROUND

The Triad satellite was launched into a circular polar orbit at 800 km altitude in September 1972 to test several techniques for improving the U.S. Navy Navigation Satellites (Ref. 1). A principal component is a highly precise magnetometer that measures the geomagnetic field along the three principal axes of the spacecraft to determine attitude. After the navigation improvement tests were performed, the satellite was devoted to collecting magnetic field data in the polar regions for auroral studies (Ref. 2). The effort, supported by the Office of Naval Research and the National Science Foundation, has required the use of telemetry collection stations in remote parts of the earth. In order to operate this equipment and still remain within the limited budget, several steps have been taken to make the data gathering as simple and automatic as possible.

The first Triad station, established in 1973 at Fairbanks, Alaska, was manually operated. It produced an analog tape that was converted to digital form at APL for computer processing and archiving. The second station, set up in 1974 at McMurdo, Antarctica, included automatic equipment to record analog tapes that likewise were converted to digital form at APL. The Fairbanks station was backfitted in 1975 with the automatic analog recording equipment and was subsequently moved to Resolute Bay, Northwest Territories, Canada, in 1976. In 1977, a plan was conceived to assemble an additional station in Scandinavia so that Triad data might be correlated with data collected by the European GEOS satellite. This presented the opportunity for further automation of the collection process.

DISCUSSION

Two costly elements in the production of Triad magnetometer data are the shipping of magnetic tape and the conversion of data from analog to digital form. The third-generation Triad station was designed to eliminate this conversion by producing digital tape directly at the collection station. Digital tape has a

packing density nearly 20 times greater than that of analog tape; thus, shipping costs are reduced. In order to include the appropriate time and control data used on other Triad digital data tapes, a considerable amount of digital logic is required at the collection station. This is supplied by using a microprocessor as the tape controller. The presence of the microprocessor, in turn, allows more complex acquisition logic in the collection station. The stations now at McMurdo and Resolute accept any signal on Triad's frequency, which in recent times includes signals from three additional satellites. The new station, with its ability to identify Triad data, can eliminate the recording time currently spent on these other signal sources.

The third-generation Triad data-collection station was assembled at APL using a prototype microprocessor. Preliminary tests indicate an improvement in data quality through the on-site digitizing process. The integral microprocessor opens the door to further automation of the highly productive Triad data-collection effort.

Figure 1 is a block diagram of the Triad 3 station. The omnidirectional antenna is mounted on the roof of the equipment site, and all other equipment is contained within the building in two 4-ft-high relay racks. The instruments include the preamplifier, receiver, phase tracking filter, and synchronizer and are used to produce digital Triad telemetry data. The time code generator, beep word detector, and time code reader (in the tape controller) form the basic timing system, which produces epoch time. The tape controller (including the microprocessor) and the tape recorder form the data-recording elements.

The processor in the tape controller performs three functions. It annotates time; inputs, formats, and qualifies telemetry data; and outputs data for digital recording. The time is input in IRIG-B serial time code. A decoder packs the bits into words that are converted to binary by the processor. The telemetry synchronization pattern is used to establish the data frame beginning and end. If the data are of good quality, the frame is released for recording on tape. If the data are from another source, they are rejected, and the tracking filter is returned to the search mode. The recording element writes data records consisting of time and telemetry data on the digital magnetic tape.

Control functions performed by the processor make use of the three basic elements to force the tracking filter to search for another signal and to close data files at the end of satellite passes. Each time a good data frame is received, a time-out is set to two minutes. When this delay is timed out at the end of a pass, the search system closes the pass data file on tape and forces a new search. If a file is closed, the search is set to delay for one hour, when the tracking filter is again directed to search. After the delay, and until more good data are received and recorded, the search command is given every two minutes.

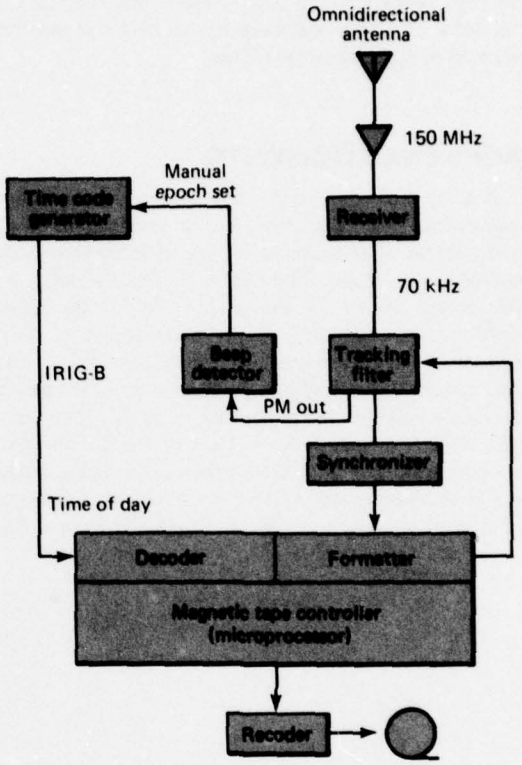

Fig. 1 Block diagram of the Triad 3 station.

Since the Triad satellite moves at a speed of more than 8 km/s, an accurate time base is required to correlate the data with the actual satellite position. Local time standards are available in the McMurdo and Resolute stations, but none is available at the potential sites in Scandinavia. The station receiver is therefore equipped with an alternate crystal to allow reception of the Navy Navigation Satellite signals, which include a precision two-minute time mark. The time mark is used to check and correct the local time epoch. In the Triad 3 station, this will be done manually as part of a local maintenance check of the time code generator. Considering the oscillator's stability of 1 part in 10^8, the drift is estimated to be less than 1 ms

per day. Weekly testing would allow timekeeping on the order of 10 ms, sufficient to calculate the satellite position to approximately 100 m.

ACKNOWLEDGMENTS

Any contribution that the Triad magnetometer experiment may have made to an understanding of solar-terrestrial phenomena is due to the efforts of a number of scientists. The late A. J. Zmuda and J. C. Armstrong played an important role in the initial development of the Triad magnetometer; S.-I. Akasofu of the University of Alaska assisted in the data acquisition from College, Alaska; A. J. Tucker of the University of Texas assisted with the McMurdo data collection; and J. K. Walker of the Department of Energy, Mines and Resources of Canada assisted with the Resolute data collection. Invaluable assistance in data processing was provided by S. Favin of APL.

REFERENCES

1. J. Dassoulas, "The Triad Spacecraft," *APL Tech. Dig.* **12**, No. 2, 1973, pp. 2–13.
2. J. C. Armstrong and A. J. Zmuda, "Triaxial Magnetic Measurements of Field-Aligned Currents of 800 Kilometers in the Auroral Region: Initial Results," *J. Geophys. Res.* **78**, No. 28, 1973, pp. 6802–6807.
3. T. A. Potemra, T. Iijima, and S. Favin, "Field-Aligned Currents in the North and South Auroral Regions Measured with Triad," *EOS* **56**, 1975, pp. 617–618.
4. T. Iijima and T. A. Potemra, "The Amplitude Distribution of Field-Aligned Currents at Northern High Latitudes Observed by Triad," *J. Geophys. Res.* **81**, No. 21, 1976, pp. 2165–2174.
5. M. Sugiura and T. A. Potemra, "Net Field-Aligned Currents Observed by Triad," *J. Geophys. Res.* **81**, No. 21, 1976, pp. 2155–2164.
6. T. A. Potemra, "Aurora Borealis: The Greatest Light Show on Earth," *Smithsonian* 7, No 11, 1977, pp. 64–70.
7. T. A. Potemra, "Large-Scale Characteristics of Field-Aligned Currents Determined from the Triad Magnetometer Experiment," *Dynamical and Chemical Coupling of the Neutral and Ionized Atmosphere*, D. Reidel Publishing Co., Boston (in press).

Authors: ***J. M. DuBrul and J. J. Neary***

Support: ***National Science Foundation and Office of Naval Research***

COMPLETION OF THE ORBIT DETERMINATION PROGRAM

An orbit determination program has been completed for the Navy Navigation Satellite System. This large and complicated program is the culmination of seventeen years of effort in space technology. Coded in PL/I computer language, it is designed to serve the needs of the Navy Navigation Satellite System through 1990 and beyond. In addition, it will serve as a valuable research tool for APL.

BACKGROUND

A major component of the Navy Navigation Satellite System is a computer program that models satellite orbit trajectories. The precision of the system depends on the ability of this program to determine and predict orbits.

Prior to 1960, the feasibility of doppler tracking was researched and demonstrated. This resulted in the current orbit program, implemented on the IBM 7094 computer at the Navy Astronautics Group in California since 1963. That program, written entirely in assembly language, is very large (more than 400 000 machine instructions and more than 20 core overlays on the 7094 computer). Orbit computations for the current constellation of five satellites require approximately eight hours of computer time per day. During its 14–year life, the program was subjected to a number of revisions and improvements, but fundamental limitations remain.

In 1968, the design of a replacement program to run on a third-generation computer system, such as the IBM 360 series, was started. However, implementation was delayed because the 7094 continued to be reliable and because it was necessary to obtain a waiver from the Navy to use the PL/I language (in 1968 PL/I was not a "standard" computer language). The scheduled cessation of 7094 maintenance by IBM at the end of 1979 prompted completion of the program and acquisition of an IBM 360/65 computer, which is roughly equivalent to the 7094.

DISCUSSION

The new Orbit Determination Program (ODP) is written almost entirely in the PL/I programming language. This higher-level language will make maintenance of the program easier because it is more readable than assembly language. Also, since PL/I is now a national standard language, more computers can run the program. ODP is still a large program, occupying about 700 000 bytes of disk space and running with eight overlays in a region of 500 000 bytes of core storage. Orbit computations for the constellation of five satellites will require approximately five hours of 360/65 computer time.

Orbit determination and prediction involve many disciplines including geodesy, celestial mechanics, mathematics, and computer science. The requirement for interaction with Navy Navigation Satellite System hardware results in a very complicated technical problem. As a minimum requirement, ODP must predict orbit trajectories for satellites at an altitude of 1000 km about 48 hours into the future with a precision of 180 m. The prediction is based on an orbit determined from 36 hours of accumulated doppler tracking data. The program consistently does better than this, with prediction errors of less than 50 m. The predicted ephemeris must then be packed and formatted according to the design of the satellite memory.

The largest single subsection of the program is the computation of the forces that act on the satellite. The gravitational force model is a series expansion in harmonic functions of hundreds of terms. Other modeled forces include the attraction of the sun and moon, the indirect effect (body tides) of these bodies on the shape of the earth, the force due to sunlight (radiation pressure), and the "drag" of the thin upper atmosphere on the satellite.

The mathematics in ODP includes the numerical solution of a second-order differential equation by finite difference techniques, extensive use of polynomial interpolation schemes, and both least-squares and Chebyshev approximation algorithms. Interleaved with them are an abundance of coordinate transformations, models of the forces on the satellite, and models of the signal propagation. Underlying all is the theory of doppler tracking, the basis for the whole system.

Use of the orbit program as a research tool has produced a kind of bootstrap improvement. Experimental versions of the program were created to study certain phenomena, and the studies produced refined models of the phenomena that were then included in the operational program. Other refinements resulted from long-term studies of program performance and work by other investigators. As a result, there has been continuing improvement in the ability of the program to determine and predict orbits. Figure 1 shows the improvement in prediction precision over the years. The improvements have resulted from changes in geodesy, atmospheric drag models, tropospheric correction, and numerical techniques.

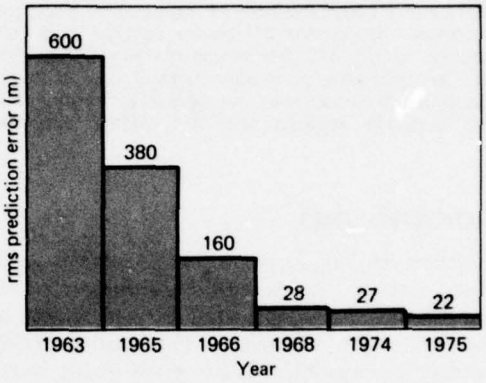

Fig. 1 Chronology of prediction improvement, indicating years when program changes were implemented.

ODP will be delivered to the Navy Astronautics Group in January 1978. Comparison runs with the 7094 program will be made during 1978, and the program is scheduled to become operational in 1979. Preliminary comparisons indicate that ODP is more precise than its 7094 counterpart. It is also more efficient, requiring roughly half the time of the 7094 program (when running on a comparable computer), and is easier to maintain since it is coded in a higher-level language.

REFERENCES

1. A. Eisner and S. M. Yionoulis, *The Semiannual Variation in the Upper Atmosphere (900–1200 km) at Solar Minimum*, APL/JHU TG 1314, September 1977.
2. H. D. Black, R. E. Jenkins, and L. L. Pryor, *The Transit System, 1975*, APL/JHU TG 1305, December 1976.
3. H. S. Hopfield, *Tropospheric Effects on Signals at Very Low Elevation Angles*, APL/JHU TG 1291, March 1976.
4. V. L. Pisacane, B. B. Holland, and H. D. Black, "Recent Improvements in the Navy Navigation Satellite System," *Navigation* 20, No. 3, Fall 1973.
5. S. M. Yionoulis, "A Study of the Resonance Effects Due to the Earth's Potential Function," *J. Geophys. Res.* 70, December 1965; also 71, February 1966.

Authors: L. L. Pryor, W. L. Ebert, and A. Eisner

Support: Strategic Systems Projects Office, SP-243

NUMERICAL METHOD FOR SOLVING ABLATION PROBLEMS AS INVERSE HEAT CONDUCTION PROBLEMS

It is cumbersome to use conventional mathematical methods to account for ablation (removal of material) in the temperature analysis of a multidimensional reentry body. Because of the need for accurate, economical calculations of reentry ablation and temperatures by the APL Aerospace Nuclear Safety Program, an improved numerical method has been devised that eliminates the cumbersome features and yields accurate ablation and temperature histories.

BACKGROUND

Ablation resulting from melting or sublimation of exposed surfaces is an inevitable consequence of the severe heating that occurs when a space vehicle reenters the earth's atmosphere. The ablative process generally has a significant effect on the reentry body's surface and interior temperatures because energy that would otherwise heat the body is used for phase change.

The primary task of the Aerospace Nuclear Safety Program is to perform reentry-temperature and structural analyses of nuclear heat source assemblies that power radioisotope thermoelectric generators for such spacecraft as Pioneer and Voyager. Its object is to determine if the heat source assembly can survive reentry in the event of an abortive launch. For reentry protection, the assemblies have a graphite shell that ablates by sublimation. To perform the analyses, a numerical technique is needed that calculates the required temperature histories, taking proper account of ablation.

Since the heat-transfer equations and the system geometry are very complex, the equations are best solved by finite-difference techniques that satisfactorily approximate the procedure in which a continuous system is modeled with a discrete system of small cells (see Figs. 1 and 2). The cells contain the points for which temperatures are to be calculated. The finite-difference equations are approximations of the differential heat-transfer equations. Cell definition is made to guarantee compatibility between the difference and differential equations so that as the cells become smaller, the finite-difference solution approaches the exact solution.

Conventional finite-difference algorithms become cumbersome when ablation is introduced because the system of cells that represents the body has to be distorted continually to account for body shape changes (Ref. 1). Figure 1 shows a possible two-dimensional model distortion from an originally rectangular cell structure. This distortion is required in order to maintain compatible cell definition. Three-dimensional ablation problems are intractable when analyzed using conventional finite-difference techniques. The elimination of the cell distortion problem in the numerical method described here allows two- and three-dimensional problems to be treated more easily, permits simpler finite-difference equations, and yields faster and more accurate temperature and ablation predictions. Ablation problems that could not have been solved previously can now be solved easily and economically.

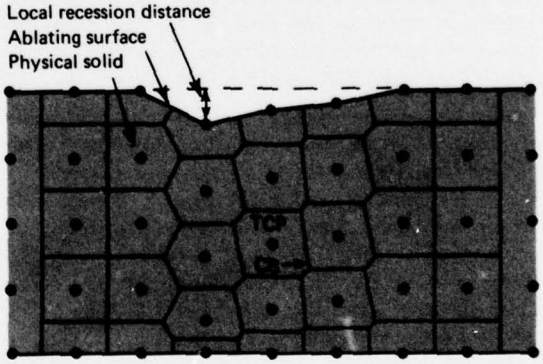

Fig. 1 Possible finite-difference cell structure for an ablation problem posed as a conventional heat-conduction problem. Only physical heating is applied to the exterior surfaces of the physical solid, which the finite-difference cells model directly. (TCP: temperature calculation point; CB: cell boundary.)

DISCUSSION

An undistorted cell geometry can be retained by embedding the ablation problem in an "inverse heat-conduction problem" that permits no material removal. Figure 2 shows how the cell distortion in Fig. 1 is eliminated by the introduction of fictitious solid in the ablated region so that a rectangular cell struc-

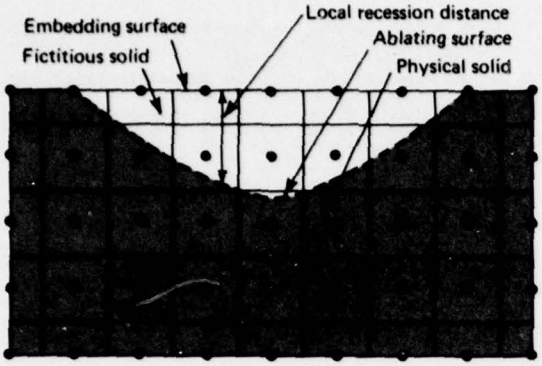

Fig. 2 Finite-difference cell structure for an ablation problem embedded in an inverse heat-conduction problem. Physical heating is applied to the ablating and nonablating surfaces of the physical solid. Fictitious heating is applied to the embedding surface.

ture is retained. To keep the heat transfer problem well posed, fictitious heating rates are applied to the embedding surface shown in Fig. 2. The rates are determined by relating them to the known ablating surface temperature, giving the problem its inverse character.

In contrast, the problem in Fig. 1 is a conventional heat-conduction problem because all enclosing boundary information is specified directly. Boley (Ref. 2) first proposed embedding ablation problems in inverse heat-conduction problems; the extension to finite-difference analysis was first proposed by the author in Refs. 1 and 3 and further elaborated in Ref. 4. A general-purpose computer program was written that uses embedding (Ref. 5) and is applicable to one-, two-, and three-dimensional rectangular, cylindrical, and spherical geometries.

The embedding computer program (designated SHTP–E) borrows heavily from APL's existing Standard Heat Transfer Program (SHTP, Ref. 6). It uses accelerated computational methods applicable to orthogonal geometries such as that shown in Fig. 2 but not to distorted ones such as that shown in Fig. 1. The ablation and temperature analysis is advanced in time steps small enough to guarantee numerical stability and accuracy but large enough for an economical calculation. Local fictitious heating rates are related to the ablating surface temperature and net heating; this provides a way to find the ablating surface temperature, location, and rate of movement as well as the fictitious heating rate. Once the fictitious heating rates are found, the temperature field in the entire body of the inverse problem is determined, and the calculation proceeds to the next time level.

References 1, 3, and 4 compare embedding results with those from more conventional methods. Other comparisons with a more exact solution can be found in Refs. 1 and 3. In the three references, the methods agree well with each other, and the superiority of the new embedding technique for the analysis of ablation problems is demonstrated.

Figure 3 is a comparison of SHTP–E predictions of recession distance (defined in both Figs. 1 and 2) for a spherical reentry body in axisymmetric flow with those made by CMA, a widely used conventional one-dimensional program for ablation analysis (Ref. 7). The SHTP–E model is axisymmetric, with the temperature depending on reentry flight time, radius from the sphere center, and angle from the forward stagnation point (the forwardmost point on the sphere with respect to the airflow). The air heating of the SHTP–E's sphere is distributed from a peak on the forward stagnation point to a minimum of 180° opposite it. The CMA model ignores angular temperature dependence and is subject only to stagnation point heating. For both models, reentry heating begins 11.06 s into a reentry flight and is characterized by a brief period of intense heating until the spheres decelerate and the heating decreases. Because of the angular distribution of heat conduction and external heating in the SHTP–E model, these results differ from the CMA results in an expected manner. Further details of the comparison are given in Ref. 4.

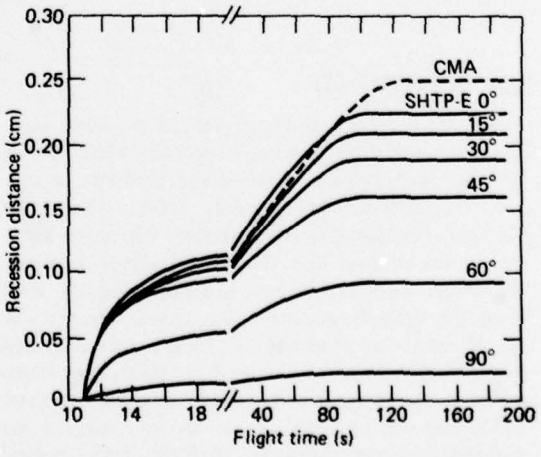

Fig. 3 Predictions of recession distances for a spherical reentry body in an axisymmetric flowfield. Angles are from the forward point of the reentry body facing the flow. The SHTP–E finite-difference model is axisymmetric and is subject to maximum heating at 0°, decreasing to a minimum at 180°. The CMA model ignores angular heating and has the maximum forward point heating applied to it.

REFERENCES

1. J. D. Randall, *An Investigation of Finite Difference Recession Computation Techniques Applied to a Nonlinear Recession Problem*, APL/JHU ANSP-M-15, March 1978.
2. B. A. Boley, "A Method of Heat Conduction Analysis of Melting and Solidification Problems," *J. Math. Phys.* **40**, No. 4, 1961, pp. 300–313.
3. J. D. Randall, "Finite Difference Solution of the Inverse Heat Conduction Problem and Ablation," *Proceedings of the 1976 Heat Transfer and Fluid Mechanics Institute*, Stanford University Press, Stanford, CA, 1976, pp. 257–269.
4. J. D. Randall, "Embedding Multi-Dimensional Ablation Problems in Inverse Heat Conduction Problems Using Finite Differences," presented at 1978 International Heat Transfer Conference, Toronto, Canada.
5. J. D. Randall, *SHTP-E, A Computer Implementation of the Finite Difference Embedding Method of Ablation Analysis*, APL/JHU CP 067 (to be published).
6. R. K. Frazer, *URLIM—A Unified Radome Limitations Computer Program*, APL/JHU TG 1293A, 1976.
7. *User's Manual, Aerotherm Charring Material Thermal Response Ablation Program, Version 3*, UM-70-14, Aerotherm Corporation, Mountain View, CA, 1970.

Author: ***J. D. Randall***

Support: ***Department of Energy***

SATELLITE PATH RAIN ATTENUATION CORRELATED WITH PREDICTED VALUES USING RADAR AND DISDROMETERS

The use of radar and raindrop size distribution measurements for determining path attenuation statistics has been demonstrated. These statistics are essential in order to determine margins for power transmissions and receiver sensitivities in designing a satellite configuration with a frequency, f, greater than 10 GHz.

BACKGROUND

Because of the increasing demand on earth-satellite communication systems, frequency bands below 10 GHz are becoming crowded and therefore prohibitive. To alleviate this problem, future systems are planned at frequencies above 10 GHz where the attenuation due to rain may represent a severe problem. To design higher-frequency systems, designers must know the attenuation distribution, that is, the percentage of time that attenuations (fades) exceed certain levels. Such information is used in establishing transmitter power margins and receiver sensitivity requirements and can be acquired directly by means of experimental geosynchronous satellites with ground receiving or transmitting stations.

An indirect way to determine fade distributions is to use predictive methods on radar measurements, thus minimizing the need to establish expensive and inefficient satellite communication systems. Predictive methods using radar and drop size distribution measurements to obtain case by case fade events as well as fade distributions were tested successfully against direct measurements with the COMSTAR beacon at 28.56 GHz. The results strongly suggest the greater use of radar for the acquisition of fade statistics for various frequencies and path configurations.

DISCUSSION

The experimental configuration consists of a phase-locked-loop receiving system operating at 28.56 GHz, an S-band radar (f = 2.84 GHz) located 30 m away, and a system of three rain gauges and two disdrometers (for measuring raindrop size distributions) located in the immediate vicinity of the receiving antenna. The receiving system has a maximum dynamic range of 33 dB below the free space cw power received, which is −106 dBm. Both the receiving and radar antennas have a beamwidth of 0.4° and look in the direction of the COMSTAR satellite (elevation 41.6°, azimuth 210°).

During periods of rain, the radar measures the backscatter of rain along the path with a range resolution of 150 m. A parameter known as the reflectivity factor, Z (mm^6/m^3), which is proportional to the backscatter but contains only the characteristics of the rain, is measured by means of the radar (Ref. 1) at each range bin.

The disdrometer is an electromechanical sensor that outputs an impulse voltage whenever a drop impacts on a 50–cm² cross-sectional area of a Plexiglas sensor (Ref. 2). For drops falling at terminal velocities, the voltage outputs are proportional to the drop momentums. Through calibration, the drop diameters may be related to the voltage outputs, and the ground drop size distributions are determined. By means of a given integration time interval (e.g., 30 s), the parameter Z may be calculated on the ground. The attenuation coefficient, k (dB/km) at 28.56 GHz, an additional parameter calculated using the measured drop size distribution, measures the attenuation per unit distance of propagation due to the sum total of all raindrops.

For each 30–s drop size distribution measured with the disdrometer, a pair of values for Z and k may be calculated. If log Z and log k are plotted against each other, a best-fit linear regression line with a relatively high coefficient of determination, r^2, may be established. The quantity r^2 measures the "goodness" of fit, 1 being perfect. A straight line on a log k versus log Z plot implies empirically that $k = aZ^b$, where a and b are experimentally determined empirical parameters.

An example of a regression line is given in Fig. 1, which corresponds to a 43–min sampling of rain during the evening of 14 September 1977 (20 h, 3 min through 20 h, 46 min GMT). The vertical and horizontal axes represent log k and log Z, respectively. Each of the 43 data points represents a 30–s integration of drop size distribution for which the rain rate exceeded 2.5 mm/h. The straight line is the best fit with $a = 3.47 \times 10^{-3}$, $b = 0.733$, and $r^2 = 0.95$. For this rain period as for others, the values of a and b were inserted into a computer program that determines the radar-predicted attenuation as a function of time. For the events considered in this study, the path length was taken only up to the 0° isotherm, above which ice predominates.

Figure 2 is an example of a corresponding attenuation event within the interval of time for the disdrometer sampling (20 h, 3 min to 20 h, 31 min GMT). The vertical scale represents the path attenuation due to rain and the horizontal scale the time in GMT. The solid curve represents measured attenuation at the satellite receiver (sampled every 3 s). The dashed curve represents the predicted attenuation using the radar reflectivities and the values of a and b determined from the disdrometer measurements. Also plotted (the dot-dashed curve) is the attenuation predicted using the radar reflectivities and the values of a and b derived from the well-known Marshall-Palmer (hereafter referred to as M–P) distribution

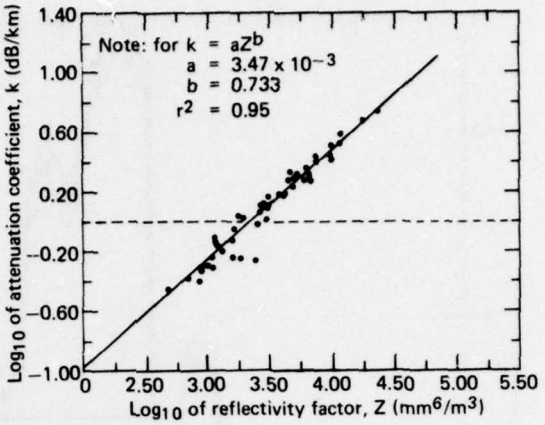

Fig. 1 Scatter diagram of $\log_{10}$ of the attenuation coefficient plotted versus $\log_{10}$ of the reflectivity factor. Each point represents a 30–s sample of drop size distribution for 14 September 1977 from 20 h, 3 min to 20 h, 46 min GMT and for rain rates exceeding 2.5 mm/h.

(Ref. 3), namely, $a = 2.01 \times 10^{-3}$ and $b = 0.773$. The radar-predicted levels were sampled every 10 s.

The receiver results apparently reached saturation at 29 dB. This represents a loss of lock condition where the overall receiver dynamic range of 33 dB is exceeded, the additional 4 dB being due to the diurnal variation of the satellite as well as to water on the antenna feedhorn. The loss due to the diurnal variation rarely exceeded 2 dB and is generally known to within ±0.5 dB. The reflection losses due to water on the antenna feedhorn were measured by controlled water spray tests and averaged 2 dB with an uncertainty of ±1 dB when a hydrophobic agent (Fusidox M) was used. The disdrometer-derived results and the M–P results are similar and show generally good correlation below 29–dB attenuation. Above this level, one to one correlation is not possible.

Since the designer of communications systems is interested in fades from a statistical point of view, radar-predicted fade distributions were compared with those measured directly. During the summer of 1977 (June through September), simultaneous data for five rain days were obtained. Table 1 summarizes the sampling days and times as well as the corresponding disdrometer results. When all the drop size distributions are considered together, the values of a and b are almost identical with those corresponding to the M–P distribution. This is attributed to the fact that the M–P distribution represents a large data base for the geographical region of Washington, D.C. (mid-Atlantic east coast). On an individual rain-period

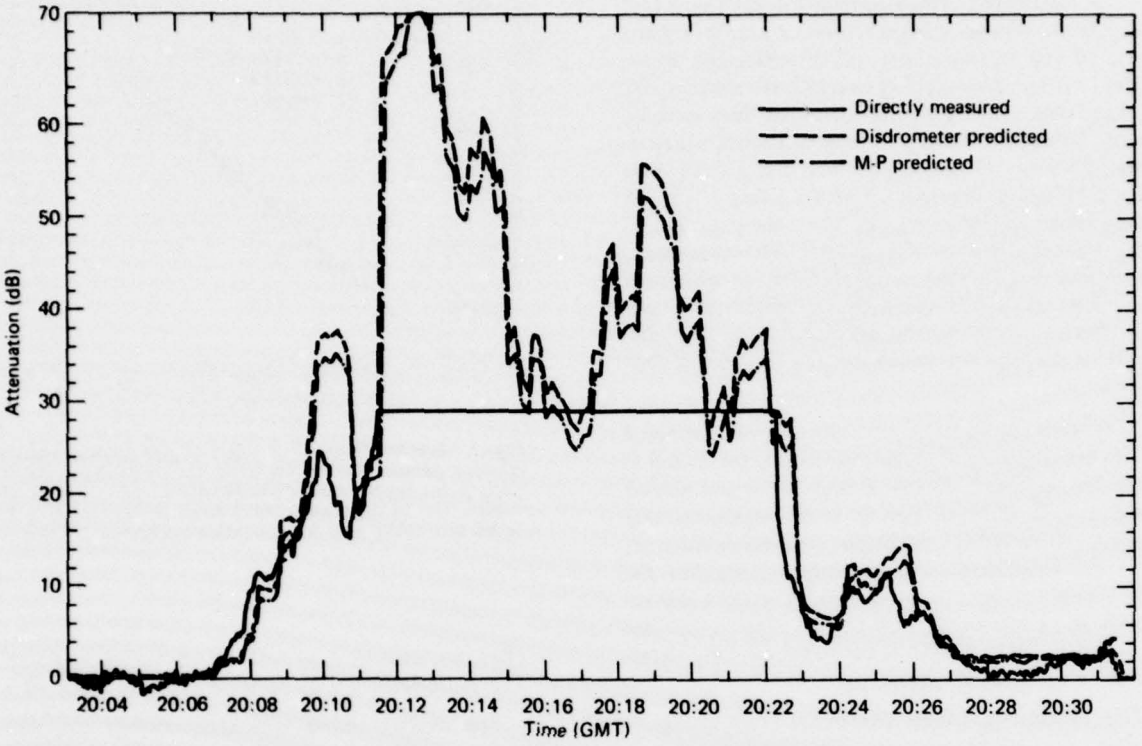

Fig. 2 Comparison of attenuation events measured directly with the COMSTAR receiver with those predicted using radar-disdrometer measurements and radar–M–P distributions. Event of 14 September 1977.

TABLE 1

SUMMARY OF SAMPLING DAYS AND TIMES AND CORRESPONDING DISDROMETER RESULTS

Date (1977)	Event No.	Sampling Time Intervals (h:min)		Disdrometer Best-Fit Parameters			
		Radar	Disdrometer	a	b	r^2	No. of Samples
6 Ju	1	21:26–21:55	21:26–22:45	1.17×10^{-3}	0.825	0.93	123
	2	21:57–22:26					
	3	22:36–22:48					
9 Jun	4	12:44–13:13	12:44–14:49	7.36×10^{-3}	0.617	0.75	180
	5	13:24–13:53					
	6	14:41–14:50					
24 Aug	7	14:56–15:24	14:21–16:30	1.23×10^{-2}	0.492	0.60	102
	8	15:38–16:07					
	9	16:09–16:25					
24–25 Aug	10	23:35–23:59	23:30–00:52	1.45×10^{-3}	0.806	0.94	107
	11	00:05–00:34					
14 Sep	12	20:03–20:32	20:03–20:46	3.47×10^{-3}	0.733	0.95	53
	13	20:33–20:48					

Notes: Overall radar sampling time = 304 min
Overall disdrometer sampling time = 458 min (565 samples)
Best fit, $a = 1.87 \times 10^{-3}$ (all disdrometer samples for all days)
Best fit, $b = 0.775$
Best fit, $r^2 = 0.89$

basis, the values of a and b may be markedly different from the M–P distribution (as indicated for the 24 August period). The M–P levels of attenuation for this period disagreed with the directly measured attenuation, whereas the disdrometer-predicted values were in relatively close agreement.

The fade distributions from the approximately five rain days of sampling (corresponding to 13 attenuation events and 5 h of simultaneous radar data) are shown in Fig. 3. The vertical scale represents the probability that the attenuation exceeds the abscissa, and the abscissa corresponds to various attenuation levels. The solid and open circles and the squares represent the directly measured, the disdrometer-radar predicted, and the radar–M–P predicted distributions, respectively. On an absolute basis, the disdrometer predicted curve is in good agreement with the directly measured one, whereas the M–P curve shows significantly poorer agreement.

These results demonstrate the utility of using radar in conjunction with disdrometer measurements for predicting fade events as well as long-term fade distributions associated with satellite communications through rain.

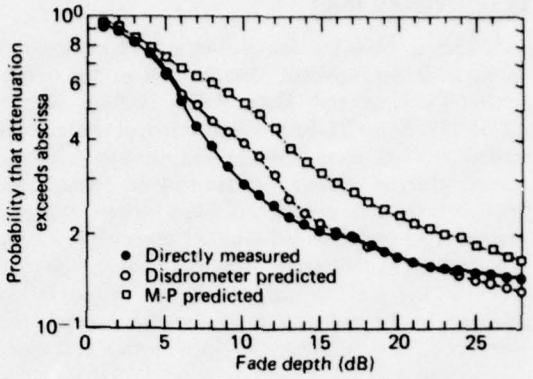

Fig. 3 Comparison of fade distributions measured directly with the COMSTAR receiver with those predicted using radar-disdrometer measurements and radar–M–P distributions. Curves correspond to five hours of simultaneous rain data covering five rain days and 13 attenuation events.

ACKNOWLEDGMENTS

The author is grateful to John R. Rowland for developing data processing instrumentation, including the disdrometer system. The useful comments and suggestions of Isadore Katz are very much appreciated.

REFERENCES

1. L. T. Battan, *Radar Observations of the Atmosphere*, University of Chicago Press, Chicago, IL., 1973, p. 43.
2. J. R. Rowland, L. W. Bennett, and R. E. Miller, *Description of the APL Disdrometer-Raingage System*. APL/JHU F1E–75U–026, 1976
3. J. S. Marshall and W. McK. Palmer, "The Distribution of Raindrops with Size," *J. Meteorol.* 5, 1948, pp. 165–166.

Author: *J. Goldhirsh*

Support: *NASA Goddard Space Flight Center*

NASA CONTROL CENTER DESIGN

An original data system design has been developed and will soon be implemented by NASA at the Goddard Space Flight Center (GSFC). The $5 million multiple-computer data system will satisfy the functional requirements (Ref. 1) of a new Network Control Center (NCC) that will be used to support the worldwide NASA Spaceflight Tracking and Data Network during 1980–1990. NCC is responsible for all NASA spaceflight tracking and data acquisition operations that are not associated with the Deep Space Network. It must ensure that data from scientific satellites and manned spacecraft are constantly supplied to the users. It must also provide a communications link between a spacecraft and its control center and/or experimenters, who may be located at a university or other non-NASA location.

BACKGROUND

NASA is planning for greater use of automation in network management, due in part to the operational Tracking and Data Relay Satellite System (TDRSS). Since TDRSS will enable a single ground station to cover most satellites and manned missions, several overseas ground stations may be phased out. However, the data system still must support approximately eight conventional Ground Spaceflight Tracking and Data Network sites along with the one TDRSS site, and typically 20 to 40 spacecraft. In addition to the automation of network control, the new NCC must also handle much higher data rates and be fault-tolerant.

One of the design objectives is to automate as many activities as practical but to allow for human intervention for critical decision-making. To satisfy this objective, a large, centralized, on-line data base is required for maintaining files on NCC operations. A software system for interactive data base management is also necessary to allow network operators to monitor and control the operations.

Input data rates of up to 10 megabits are required, more than an order of magnitude greater than the present NCC system. This reflects the increased data requirements of most satellites and manned space missions, and the greater number of spacecraft that will be in operation in the future.

NCC must provide data-processing services 24 hours per day, seven days per week. Operations must be near real time in order to respond to network anomalies arising from link failures, loss of data, or equipment failures. These conditions often require the network operators to reconfigure resources interactively and perform emergency scheduling. At times, test and simulation are required before this can be done. Mandatory performance requirements were imposed on the data system design to ensure sufficient fault-tolerance.

Finally, the design must be made cost effective by minimizing special hardware/software designs and by using off-the-shelf systems. Also, to allow for competitive bidding, it must not be limited to a single system.

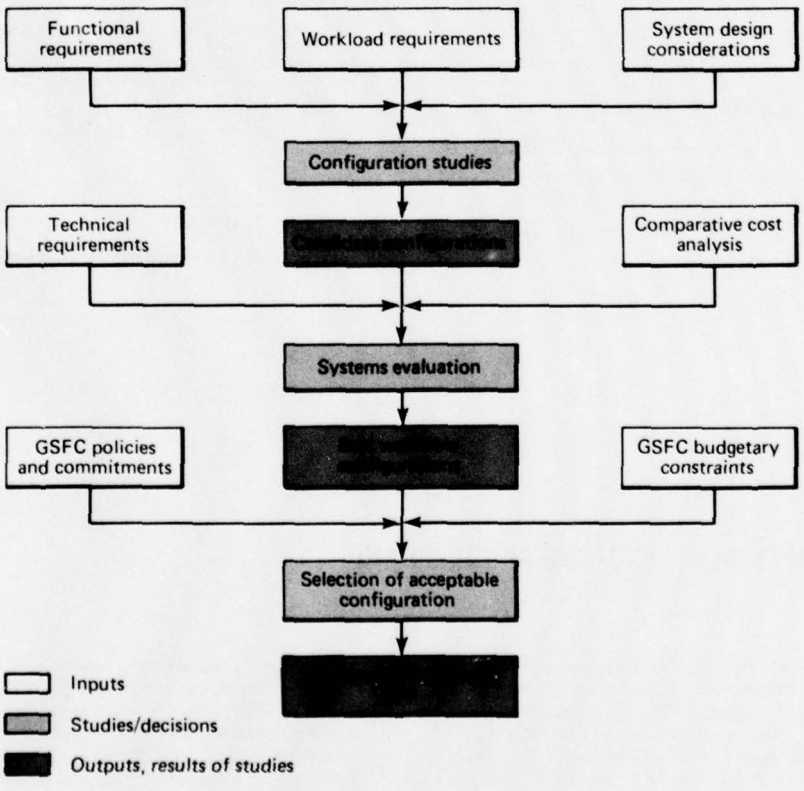

Fig. 1 Design methodology.

DISCUSSION

The engineering methodology used for the data system design is illustrated in Fig. 1. Various inputs were identified and trade-off analyses were performed to determine which functions are best centralized as opposed to those best distributed. It was determined that a configuration for both centralized and distributed functions provided the best solution. The requirement for providing a large interactive data base that is accessible and functionally assignable to a large number of terminals was best satisfied by a

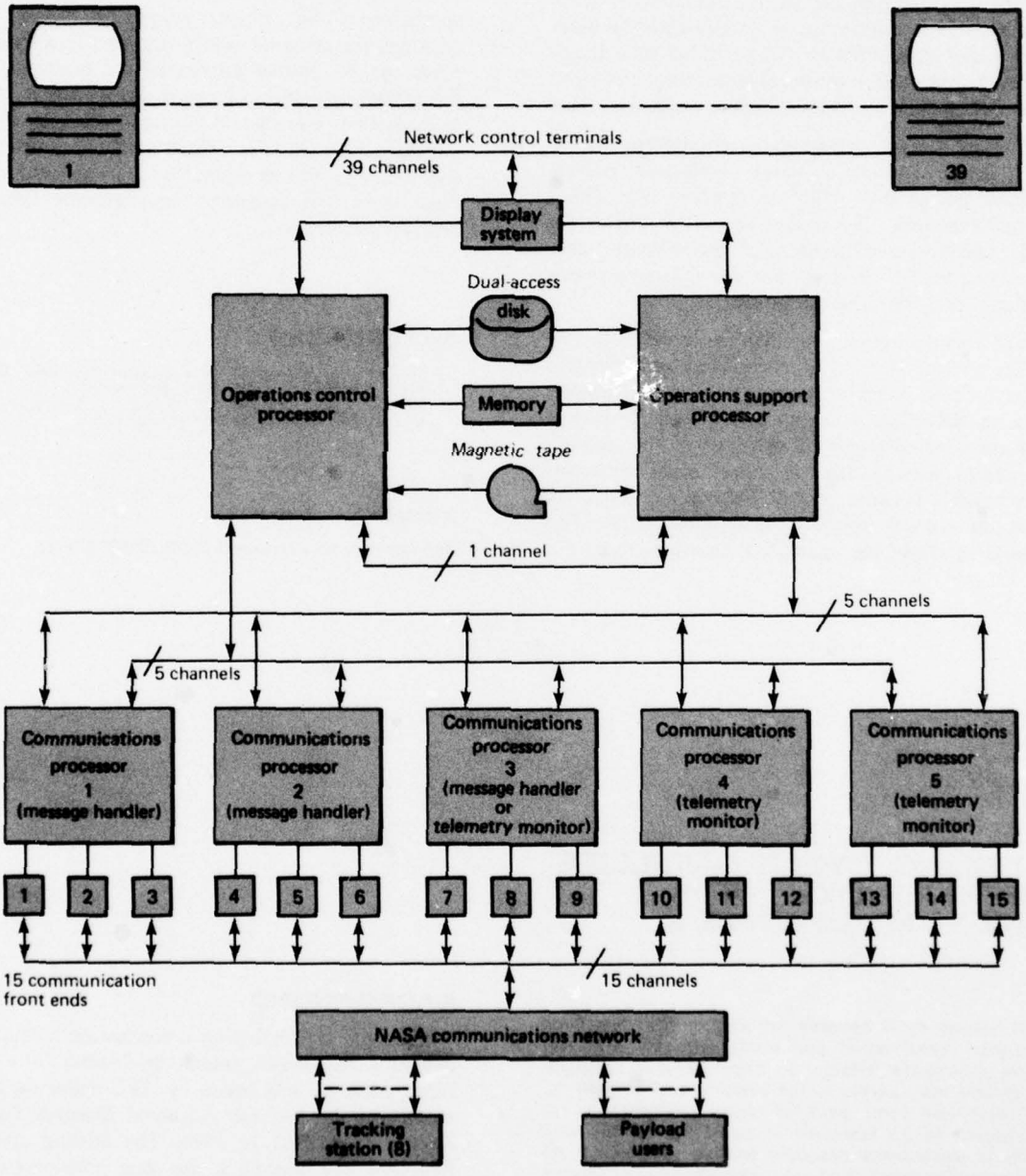

Fig. 2 Configuration of NCC data system.

centralized system. Trade-off analyses performed on the flow of communications data showed that these functions must be distributed to accommodate the number of links and the high data rates.

Additional trade-off studies were made on the use of hardware versus software while minimizing special designs. A study of the communication links revealed that a considerable amount of data formatting/reformatting, packing/unpacking, and frame synchronizing could be performed more efficiently by hardware rather than software. This resulted in a design that required special communication front-end units that could handle messages or monitor telemetry data.

The mandatory performance requirements called for a design that would tolerate single-point failures without losing the ability to support time-critical control functions. The design must also provide for both scheduled and unscheduled maintenance, without disruption of services. The configuration shown in Fig. 2 provides these capabilities.

The communication functions are accomplished by means of four identical minicomputers and front-end units, each of which can process message or telemetry data. A redundant processor is required for backup and software development. Analysis of the network operations showed that an almost equal separation was possible between control and support functions, with the control functions being time-critical. This separation allows the operational functions to be distributed between two identical operational processors, thereby avoiding unnecessary redundancy. The design also provides for a "tightly-coupled" multiprocessor system with shared dual-port memory and dual-access peripherals for auxiliary storage. Should either processor fail, the high-priority control tasks will continue and the support tasks will be delayed pending repairs.

Detailed equipment and software procurement specifications (Ref. 2) were supplied to NASA. They provided for extensive potential growth and the flexibility for the further distribution of functions after the system becomes operational. Sperry Univac Computer Systems was selected to provide the total system, which will consist of a Univac 1100/20 multiprocessor, five V77–613 minicomputers, 15 communication front ends, and associated intercomputer interfaces and system software.

REFERENCES

1. *Network Control Center—Data Systems—Functional Requirements*, NASA/GSFC STDN 203.3, February 1977.
2. *Network Control Center (NCC)—Data System Specification*, NASA/GSFC GSFC–S–812–57, February 1977.

Author: ***I. R. Hunter***

Support: ***NASA Goddard Space Flight Center***

STIRLING CYCLE SATELLITE REFRIGERATOR WITH ONE-YEAR LIFETIME

A Stirling cycle satellite refrigerator that has been designed, constructed, and tested will cool a germanium gamma-ray detector to liquid nitrogen temperatures and will operate in the satellite environment for at least one year. Four of these refrigerators are scheduled to be launched in mid-1978 on the first satellite experiment designed to use mechanical refrigerators to obtain high-resolution gamma-ray spectra in space.

BACKGROUND

The task of developing a mechanical refrigerator to cool a germanium gamma-ray detector for a satellite experiment was begun by APL under the sponsorship of the Defense Advanced Research Projects Agency (DARPA) in 1973. The Stirling cycle refrigerator was selected as the most promising candidate, and six refrigerators have been constructed.

Previous attempts to cool radiation detectors in orbital flight, using either solid cryogens or mechanical refrigerators, are reviewed in Ref. 1. In the few instances they have been used for infrared detectors, mechanical refrigerators have not operated more than a few hundred hours and have performed erratically. The ability of the Stirling cycle refrigerator to cool detectors to cryogenic temperatures of about 77 K with relatively good efficiency has been well known for some years. However, it has been difficult to obtain lifetimes greater than several hundred hours and to cope with the environmental factors associated with satellite launch and flight.

DISCUSSION

In addition to providing the required cooling capacity, a satellite refrigerator must meet stringent requirements for weight, power consumption, vibration transmitted to the detector, torques transmitted to the satellite, and survival during launch. The APL/DARPA refrigerator (Fig. 1) has met the following specifications:

Output refrigeration	
First stage	140 K at 1.5 W
Second stage	65 to 75 K at 0.3 W
Power consumption	30 to 35 W
Speeds (three ground-selectable)	850, 1000, 1150 rpm
Weight	15.8 lb
Heat exchange temperature	0 to 45°C
Vibration of cold point	<0.00013 in.
Starting torques	<0.01 in.-oz
Launch vibration	18.9 g rms for 2 min each axis
Lifetime	7200 hours, test continuing

Five of the refrigerators have been delivered to the Lockheed Palo Alto Research Laboratory (LPARL), which will fly four of them in a satellite experiment. The remaining refrigerator is being life tested at APL. The cryogenic portion of the refrigerator was manufactured by Philips Laboratories under subcontract to APL. The electronics package was built at APL; it contains the switching circuitry for the brushless DC drive motors, the speed-control circuitry, and the signal-processing circuitry for the rpm, gas pressure, current, and temperature measurements of

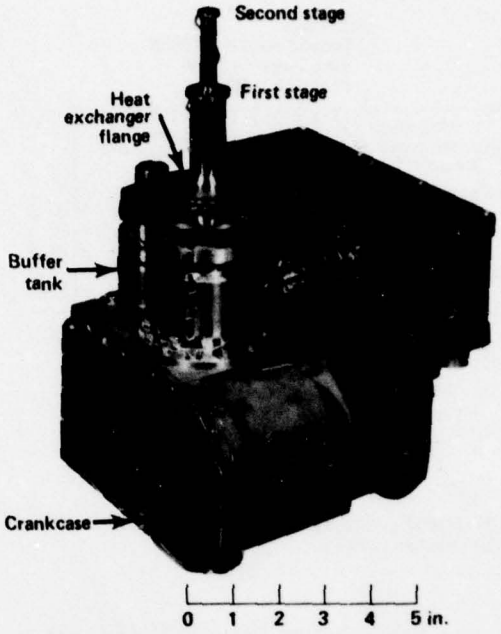

Fig. 1 The APL/DARPA refrigerator.

the motor, which are telemetered back to earth. All performance, qualification, acceptance, and life testing has been performed at APL.

The mechanical details of the interior of the refrigerator and the solutions to the construction problems are described in Ref. 2.

Unquestionably, the most interesting aspect of any satellite refrigerator is its performance as a function of time over long periods. The Serial No. 1 refrigerator being life tested at APL has accumulated an unprecedented 7200 hours of operation. Figure 2 shows the first- and second-stage temperatures as a function of time for a continuous run of 360 hours. The temperature rise is about 1 K per day for the second stage. When the refrigerator was stopped, allowed to warm up, and then restarted, it returned to (or almost returned to) its original performance. The rate of temperature climb shown in Fig. 2 is related to the purity of the helium gas within the refrigerator. The rise of 1 K per day or less can only be achieved with careful outgassing of the refrigerator under vacuum conditions and careful charging with clean helium.

Superimposed upon the slow daily temperature climb is a slower climb of the initial start-up temperature (Fig. 3). This slow rate of degradation can be caused by wear of the displacer seals, gas contami-

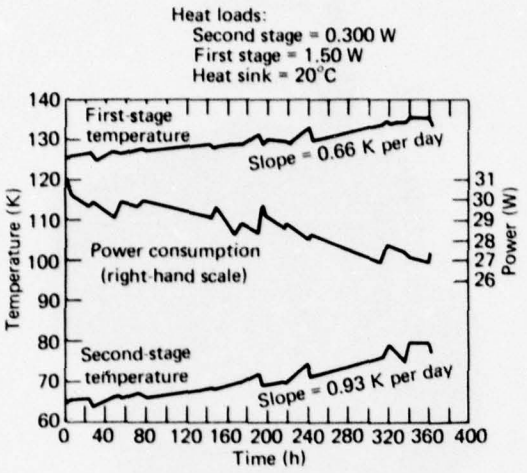

Fig. 2 Initial performance of Serial No. 1 refrigerator as a function of time.

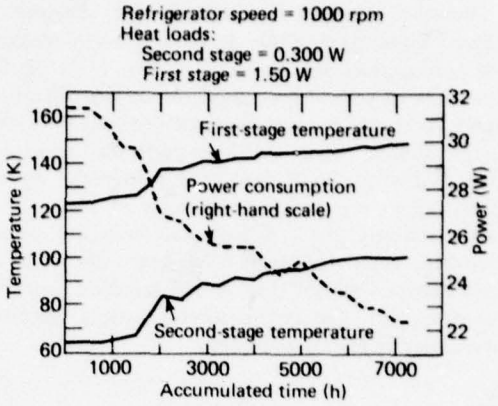

Fig. 3 Initial temperatures and power consumption (24 hours after start-up) versus accumulated hours of operation.

nants, and loss of helium pressure. The life test of the Serial No. 1 refrigerator has been conducted with no maintenance, disassembly, or gas recharging, and the contributions of the various factors to degradation of performance cannot be assessed until the test is completed. The results shown in Fig. 3 are for a refrigerator speed of 1000 rpm; if the speed is increased to 1150 rpm, the second-stage temperature will be about 75 K after 7200 hours of operation.

The intermittent gamma-ray experiment to which this refrigerator is fitted uses an intrinsic germanium detector. It does not require continual cooling nor is there a requirement for continual operation for periods greater than 200 hours. The resolution and sensitivity of the detector do not degrade at temperatures less than 120 K. Thus the results presented show that the APL/DARPA refrigerator meets the requirements of the experiment for which it was designed.

REFERENCES

1. T. C. Nast and D. D. Murray, "Orbital Cryogenic Cooling of Sensor Systems," presented at American Institute of Aeronautics and Astronautics, AIAA Paper No. 76-979, October 1976.
2. C. Balas, C. S. Leffel, Jr., and C. A. Wingate, "A Stirling Cycle Cooler: Approaching One Year of Maintenance-Free Life" (to be published in *Adv. Cryog. Eng.* 23, 1977).

Author: ***C. S. Leffel, Jr.***

Support: ***Defense Advanced Research Projects Agency***

BIOMEDICAL SYSTEMS

INTRODUCTION

The Johns Hopkins University School of Medicine, the School of Hygiene and Public Health, and APL have collaborated in a program of biomedical research and development since 1965. An important objective of the program is to apply the "know how" of engineering and physical sciences, acquired by APL in defense and civilian research and development, to solve problems in medical research and health care delivery. The program has included collaboration with nearly all of the clinical departments and with many of the basic science departments of the medical divisions. More recently, a collaborative program has been established with the Johns Hopkins Hospital. There are active programs in molecular biology, nuclear medicine, ophthalmology, neurosensory research and instrumentation development, radiology, cardiovascular systems, prosthetic systems, computer support and clinical information systems, and clinical engineering.

This application of state-of-the-art technology has contributed to many areas of basic medical research and to clinical diagnosis and therapy through the improvement of instrumentation, techniques, and knowledge. The application of systems engineering techniques has helped solve problems of the health care delivery system. These activities have a focus in the Department of Biomedical Engineering at the Johns Hopkins Medical Institutions. In addition, a new educational program developed in collaboration with members of the Department of Biomedical Engineering leading to a Master's Degree in clinical engineering was established in September 1973 at the Medical School.

The results of the research and development in this program are reported in the open literature, principally in biomedical, biological, and medical journals. During the program's relatively short life, more than 150 papers and several book chapters have been published, and more than 70 instruments for research and clinical application have been developed. A number of APL staff members have assumed line responsibility for JHMI in areas where technology can make specific contributions to patient care and to the health care delivery system. These areas include radiation physics, information

processing, and the definition of technical requirements for the maintenance of the highly technological medical equipment used for patient care.

At any given time, there are 40 to 60 active projects within the biomedical program. They range all the way from fundamental spectroscopic studies of model biological compounds—to the discovery of a method for observing the blood flow in usually inaccessible regions of the human eye—to the specification of monitoring equipment and communication systems for better patient care.

The projects reported herein include efforts in fundamental research and in the biomedical application of technology developed in other fields of APL activity. The first article demonstrates the utility of using a mathematical model to describe the transport of ions and fluid through the structured biological tissue making up the corneal epithelium. The next describes measurements of the effect of intraocular pressure on the small angle scattering of polarized light by corneal tissue. The third describes the development of exercise echocardiography, a new technique that shows promise in the early detection of heart disease. The fourth deals with the incorporation of a microprocessor into the command and control system of a medical manipulator for patients with high spinal cord injury, thus vastly reducing the number of instructions needed to control the manipulator.

The last three articles describe accomplishments at the Johns Hopkins Oncology Center. A computerized information system gives doctors rapid access to medical histories for treatment or research. A program for testing and calibrating radiation treatment machines has been developed and implemented. Finally, a monitoring system using data telemetry has been developed for use with ambulatory patients.

Of course, the articles that follow are only a sample of the broad range of activities within the collaborative biomedical engineering program. Other projects will be highlighted in subsequent *Accomplishments* volumes.

COMPUTER MODELING OF TRANSPORT IN BIOLOGICAL TISSUE

A mathematical model of transport in structured biological tissue has been constructed and used to examine the transport and electrical properties of the corneal epithelium. By incorporating a primitive structure into the model, it becomes possible to interpret experimental data on entire tissue in terms of more detailed processes taking place, without the errors that can result when structure is ignored.

BACKGROUND

The corneal epithelium is a multiple layer of cells at the very front of the eye, bathed by the tears on the surface and supported by the corneal stroma, a layer of gel-like connective tissue that makes up most of the thickness of the cornea (Fig. 1). Because of its gel-like character, the stroma has a tendency to swell, and stromal swelling is known to decrease corneal transparency. Since the epithelium is the only barrier preventing stromal imbibition of the tears, it is important to understand its physiology and role in the maintenance of normal corneal thickness. The complex set of transport pathways through the epithelium cannot be characterized fully by available experimental techniques; the purpose of this study was to gain useful information by analyzing experimental data in the context of a simpler structural model of this tissue.

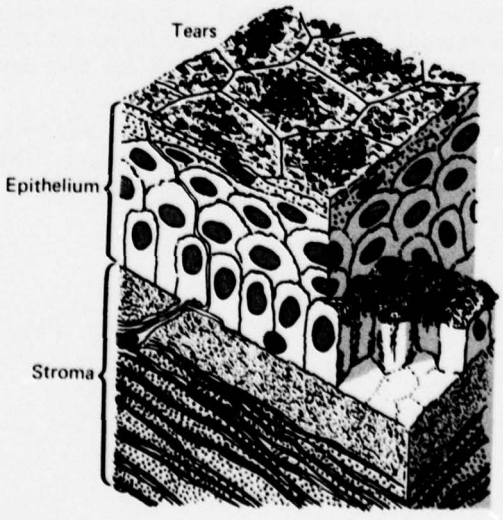

Fig. 1 Three-dimensional drawing of the corneal epithelium.

DISCUSSION

The structure of the epithelial model used in this work (Fig. 2) consists of a transcellular pathway in parallel with a shunt between the cells. This structure is much simpler than that of the real epithelium (compare Fig. 1) but is sufficient to explain many experimental data on this tissue. Also, because of the simplicity, the parameters of the model (e.g., the ionic permeabilities of the shunt and cell membranes and the rates of metabolically coupled ion transport into and out of the cell) are few enough to permit them to be evaluated from electrophysiologic data on entire tissue and microelectrode punctures of the electrically coupled epithelial cells.

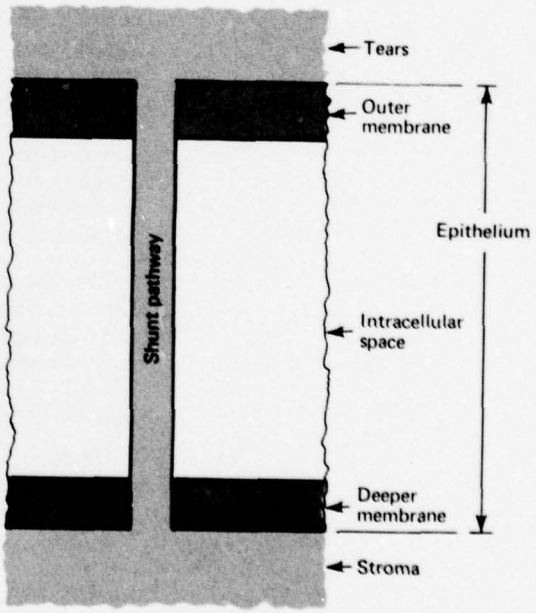

Fig. 2 Structure of the model epithelium.

In the model, the tears and stromal fluid can contain any number of permeant monovalent ions (typically Na^+, K^+, and Cl^-) and charged impermeants. Fluxes across the shunt and the cell membranes are given by the very general Nernst-Planck equations that relate ion flux to concentration and potential dif-

TABLE 1

PREDICTED AND EXPERIMENTAL THINNING RATES

Condition	Thinning Rate (μm/h)		
	Experimental, Refs. 2, 3	Calculated	
		R_s = 36 kΩ-cm² *	R_s = 9 kΩ-cm² *
Resting	−1.0 ± 0.2 **	0.08	0.2
Stimulated †	1.3 ± 0.1	0.7	1.9
Chloride-free bath, resting ‡	3.9 ± 0.6	3.2	5.6
Chloride-free bath, stimulated †‡	6.2 ± 0.6	4.6	7.6

* These bracket the experimental variation of the shunt resistance, R_s, which is variable because of its sensitivity to the traumatic effects of handling.

** Minus sign denotes swelling.

† On the basis of other data, stimulation is modeled as a fourfold increase in the permeability of the outer membrane to chloride ion.

‡ Chloride in tear-side solution replaced by impermeant sulfate.

ference driving forces. Kinetic expressions for the dependence of the active ion transport rates on substrate concentration are also included. The model is described in much fuller detail in Ref. 1.

The parameters of the model (e.g., the permeability of each barrier to each ion) were evaluated largely from intracellular and transepithelial potential measurements. The parameterized model has been used to predict the fluxes across the epithelium and the response of these fluxes and of the intracellular and transepithelial potentials to changes in ambient composition and passive permeabilities. Of more general interest, model calculations have demonstrated that several experimental techniques used to measure the transport properties of biological tissue can give misleading or erroneous results when the tissue has a structure even as primitive as that used here.

To illustrate the predictive capabilities of the model, consider an experiment (Refs. 2 and 3) in which a cornea is removed from the eye and fluid exchange at the back surface of the stroma is inhibited by a layer of oil. Because of the metabolic ion pumps in the epithelium, there will be a net salt flux into or out of the stroma. This will induce a corresponding water flow by osmosis, and the stroma will swell or thin. The rate of swelling or thinning can be influenced by altering the composition of the medium bathing the front surface of the cornea (changing the driving force for salt flow) or by agents such as adrenaline or theophylline, which alter epithelial membrane permeability. Experimental data on the stromal thinning rate for two ambient compositions, at rest and theophylline-stimulated, are compared with predictions in Table 1. The agreement is quite good.

REFERENCES

1. M. H. Friedman, "Mathematical Modeling of Transport in Structured Tissues: Corneal Epithelium," *Am J. Physiol.* **234**, 1978, pp. F215–F224.
2. S. D. Klyce, "Transport of Na, Cl, and Water by the Rabbit Corneal Epithelium at Resting Potential," *Am J. Physiol.* **228**, 1975, pp. 1446–1452.
3. S. D. Klyce, "Enhancing Fluid Secretion by the Corneal Epithelium," *Invest. Ophthalmol. Vis. Sci.* **16**, 1977, pp. 968–973.

Author: *M. H. Friedman*

Support: *Indirectly Funded R&D*

EFFECTS OF PRESSURE ON CORNEAL SMALL-ANGLE LIGHT SCATTERING

The scattering of polarized laser light by the cornea is investigated as a function of transcorneal pressure. Marked changes in the light scattering occur as the pressure increases. Also, the standard procedures used to prepare corneal tissue for electron microscopy have been modified so that a transcorneal pressure is maintained during the fixation step. This modification produces structural alterations that could explain the observed changes in light scattering with applied pressure.

BACKGROUND

The cornea is the clear, tough window in the eye that admits light to the photoreceptors in the retina. The cornea's mechanical strength is provided by its constituent rod-like collagen fibrils. The fibrils scatter the incoming light, and modern theories recognize that corneal transparency is the result of destructive interference among the light waves scattered in all except the forward direction (Refs. 1 to 3). These interference effects arise because the spatial arrangement of the fibrils is partly ordered. We have recognized that light scattering provides a noninvasive probe of structure and that it can be used to test the predictions of various structural models that have been proposed. Up to now, by comparing light-scattering measurements with theoretical calculations based on structures shown in electron micrographs (EM), we have been able to show that the wavelength dependencies of the observed light scattering are consistent with the structures depicted in EM.

Other researchers have been attempting to elucidate corneal structure by using the small-angle light-scattering (SALS) methods that have been a powerful tool in understanding polymer morphology (Refs. 4 and 5). SALS differs from our previous methods in that polarization effects are investigated; moreover, SALS probes larger structures. However, comparisons of the observed scattering with model structures for which the SALS is known and with corneal structures known histologically have not been satisfactory.

Despite these difficulties, our success with conventional scattering methods led us to believe that a similar approach should work with corneal SALS. In this regard, we noted corrugations in the lamellar structure shown in EM of corneas fixed conventionally in the absence of pressure (cf. Fig. 1a). These corrugations have a fairly regular period of several microns and, although no calculations have been made, we felt that the waves could influence corneal SALS.

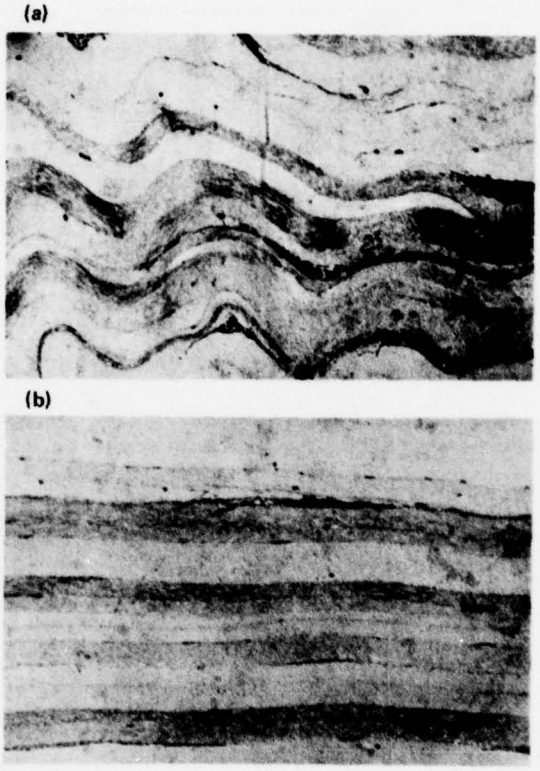

Fig. 1 Low-power EM of corneal stroma of pair eyes from same rabbit. (a) Fixation in the usual manner with no applied pressure. Note the waviness of the lamellae. (b) Fixed with applied pressure of 18 mmHg. Note that the lamellae are straight.

Moreover, J. Francois (private communication) had suggested that the waviness was reduced in EM where the normal intraocular pressure (IOP) was maintained during fixation. Previous SALS measurements were made without maintaining a transcorneal pressure; consequently, we set out to investigate the effect of IOP on corneal small-angle light scattering and to confirm Francois' suggestion (Ref. 6).

DISCUSSION

In the SALS technique, the cornea is illuminated with a collimated beam of polarized light from a laser. Light scattered with polarization either parallel or perpendicular to that of the incident beam is ob-

served at scattering angles of less than 5°. These scattered light intensities form patterns that are called the $I_{\parallel}$ *and* $I_{\perp}$ patterns, respectively. The $I_{\parallel}$ scattering pattern results primarily from isotropic optical density fluctuations within the scatterer, whereas the $I_{\perp}$ scattering pattern is caused by anisotropic optical density fluctuations. The $I_{\perp}$ pattern shows the most significant effects of transcorneal pressure.

Figure 2 shows the effect of increasing IOP on the $I_{\perp}$ scattering from the central region of a rabbit cornea (Ref. 6). The effect of corneal birefringence on these measurements was minimized by standard means (Refs. 4 and 5). The zero-pressure pattern is consistent with those in Ref. 5. As the pressure is increased, the zero-pressure pattern persists but its intensity decreases until it is barely discernible at the normal IOP (18 mmHg). Above zero pressure, a new, previously unobserved pattern becomes visible.

We suggested (Ref. 6) that the zero-pressure pattern arises from the waviness in the corneal lamellae that is seen in conventionally fixed EM of corneas (cf. Fig. 1a). Subsequently, we devised a relatively simple means for EM fixation while maintaining a transcorneal pressure. When fixed at 18 mmHg, the lamellae are almost perfectly straight (cf. Fig. 1b), which confirms Francois' suggestion and provides strong histological support to our suggestion for the origin of the zero-pressure scattering pattern.

Subsequent to our original experiments reported in Ref. 6, we have been attempting to explain the new inner pattern. We have shown that, in fact, it is not a SALS effect. The inner pattern is actually a projection of a cross that appears over the whole cornea when it is illuminated with polarized light and observed through a crossed polarizer (Ref. 7). In our original experiments, we did not eliminate the diffuse polarized light that fell over the whole cornea because we felt that it was insignificant compared to the intensity of the laser beam through the center. If this stray polarized light is carefully removed by means of apertures, both the corneal cross and the inner pattern can be eliminated. We note, however, that the origin of the corneal cross has never been satisfactorily explained, and we are presently attempting to learn its structural basis.

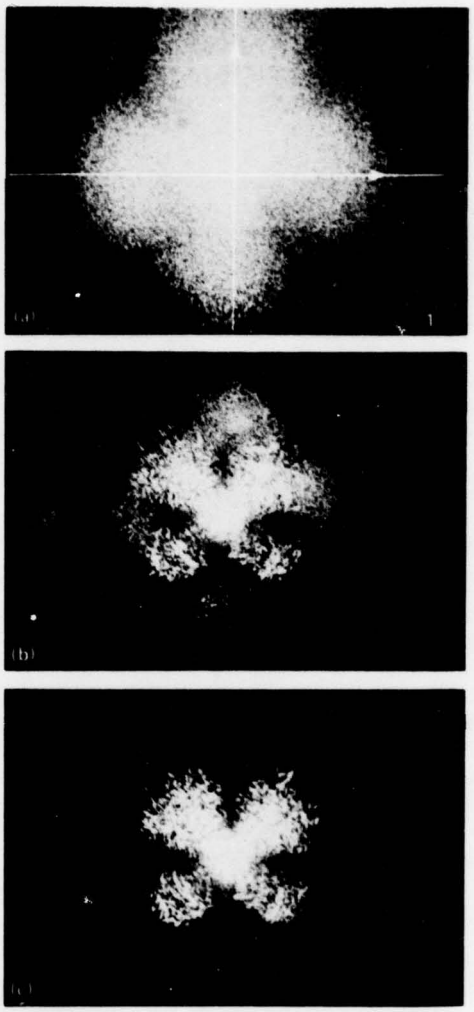

Fig. 2 Effect of increasing transcorneal pressure on the $I_{\perp}$ scattering pattern. (a), (b), and (c) are at 0, 9, and 16 mmHg, respectively. The arrows show the direction of the polarizer axes. The scale for the true scattering angle is given in (a). Each photograph received the same exposure and development.

REFERENCES

1. R. W. Hart and R. A. Farrell, "Light Scattering in the Cornea," *J. Opt. Soc. Am.* **59**, 1969, pp. 766–774.
2. R. A. Farrell, R. L. McCally, and P. E. R. Tatham, "Wavelength Dependencies of Light Scattering in Normal and Cold Swollen Rabbit Corneas and Their Structural Implications," *J. Physiol.* **233**, 1973, pp. 589–612.
3. R. A. Farrell and R. L. McCally, "On Corneal Transparency and Its Loss with Swelling," *J. Opt. Soc. Am.* **66**, 1976, pp 342–345.
4. F. A. Bettelheim and D. Kaplan, "Small Angle Light Scattering of Bovine Cornea as Affected by Birefringence," *Biochim. Biophys. Acta* **313**, 1973, pp. 268–276.
5. E. P. Chang, D. A. Keedy, and J. C. W. Chien, "Ultrastructures of Rabbit Corneal Stroma: Mapping of Optical and Morphological Anisotropies," *Biochim. Biophys. Acta* **343**, 1974, pp. 615–626.
6. R. L. McCally and R. A. Farrell, "Effect of Transcorneal Pressure on Small Angle Light Scattering from Rabbit Cornea," *Polymer* **18**, 1977, pp. 444–448.
7. D. G. Cogan, "Some Ocular Phenomena Produced with Polarized Light," *Arch. Ophthalmol.* **25**, 1941, pp. 391–400.

Authors: ***R. L. McCally and R. A. Farrell***

Support: ***U.S. Public Health Service Grant EY 01019***

QUANTIFYING HEART-WALL MOTION AND THICKENING BY NONINVASIVE TWO-DIMENSIONAL ECHOCARDIOGRAPHY

Newly developed ultrasonic imaging instruments that use two-dimensional electronic scanning have been applied to the visualization of individual planes through the heart and to the quantification of the resultant video data. These data, taken while the subject is exercising, can differentiate on a regional basis between normal motion of the heart wall on the one hand and abnormal motion and thickening of the heart wall on the other. The technique shows promise for the early detection of heart disease and, being noninvasive, is a candidate for screening people in the general population who are believed, because of other factors, to risk such disease.

BACKGROUND

For years, the two tests used most often to determine the presence of coronary artery disease have been cardiac arterial angiography and the electrocardiogram (EKG) taken during exercise. Although the EKG method is noninvasive, it is difficult to interpret, results in an undesirable number of false positives, and is not sufficiently sensitive to mild ischemia (inadequate oxygen supply). The angiography technique requires that a catheter be inserted into the aorta to deliver opaque contrast material to the coronary arteries, which are then viewed by X ray. This method is highly invasive and cannot detect mild ischemia. The echocardiographic technique is totally noninvasive and shows promise of detecting changes in heart wall motion and thickening resulting from changes in the elastic constants of the heart wall caused by mild ischemia.

DISCUSSION

Figure 1a shows one video frame (taken at the rate of 30 per second) of a cross section of the left ventricle of the heart (white represents tissue, black the blood-filled interior). Several frames taken at this section record the dynamics of the ventricle as the heart beats. In Fig. 1b, computer-generated contours are superimposed on the video frame of Fig. 1a and are modified by an operator who moves circumferential points (usually 16) equally spaced in an angle about the center of the area. The contours are smoothed, remodified as necessary, and stored. The next frame is processed similarly using the previous contours as the beginning approximation.

The contours are adjusted by the operator by translation, size change, and radial motion of a preselected number of points. After contouring N frames covering a full cardiac cycle, the N sets of 16 points

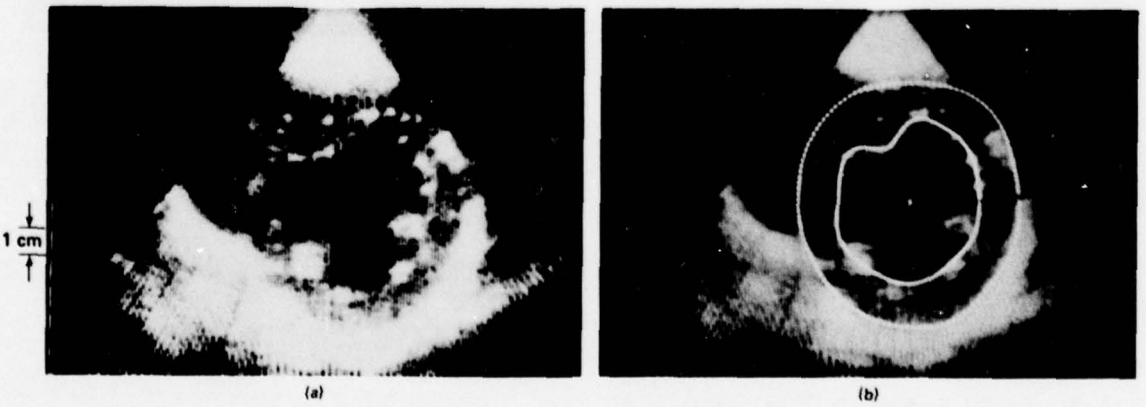

Fig. 1 (a) Normal two-dimensional echo cross section at end diastole at the level of the papillary muscles. (b) Same section with inner and outer wall contours superimposed. Papillary muscles are excluded from this contour.

are Fourier transformed, filtered, and inverse transformed to the desired number of time samples. Such data from planar sections can be combined to provide three-dimensional volume and regional wall measurements.

Figure 2 indicates the shortening of 16 segments around the left ventricle at the end of ventricular contraction (end systole) obtained by subtracting the segmental radius at the beginning of contraction (end diastole) from that at end systole. Figure 2a, for a typical heartbeat of a normal control subject, shows relative systolic radial shortening around the whole left ventricle. In contrast, Fig. 2b shows the same regional motion in a patient who has suffered considerable damage in the frontal portion of his left ventricle from a previous heart attack (anterior myocardial infarction). One can see the segments that exhibit reasonable motion, those that show relatively little motion (hypokinesis or akinesis), and those that show paradoxical lengthening (dyskinesis).

These and similar results demonstrate the ability of the system to obtain quantitative measurements of regional myocardial performance. The major efforts during the coming year will be to validate the ultrasonic results by comparing them with results from current techniques (e.g., angiography and gamma camera studies), and to explore techniques for automating the contouring system.

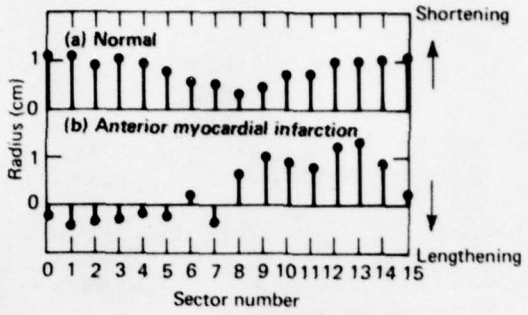

Fig. 2 Maximal segmental systolic shortening of the internal left ventricular radius (end-diastolic/end-systolic radius).

Authors: *J. B. Garrison (APL) and J. L. Weiss and N. J. Fortuin (JHMI)*

Support: *Frank T. McClure Fellowship in Cardiology and NIH Grant HL-19232 (NHLBI)*

MICROPROCESSOR CONTROL AND COMMAND FOR MEDICAL MANIPULATOR

The application of a microprocessor to the control and command system of an electrically powered medical manipulator, formerly implemented with discrete digital and analog circuitry, improved the manipulator's dynamic performance and versatility. Easily reprogrammable sequences command the manipulator through a variety of motion sequences to aid the quadriplegic patient with certain everyday tasks.

BACKGROUND

Quadriplegics are in the unfortunate position of having little or no control of their trunk and limbs but often retain the ability to move their head or their facial muscles. These muscles may be used to command a powered manipulator, thereby offering the quadriplegic patient some degree of independence in performing everyday tasks such as reading, typing, eating, and telephoning.

A six-degree-of-freedom electrically powered manipulator designed by APL (Ref. 1) gave the patient the ability to execute any desired sequence of motions with the aid of a chin commander (Fig. 1). Physical control consists of a linear and a discrete command, the linear command being proportional to the chin commander's vertical position and the discrete command emanating from a microswitch located at the

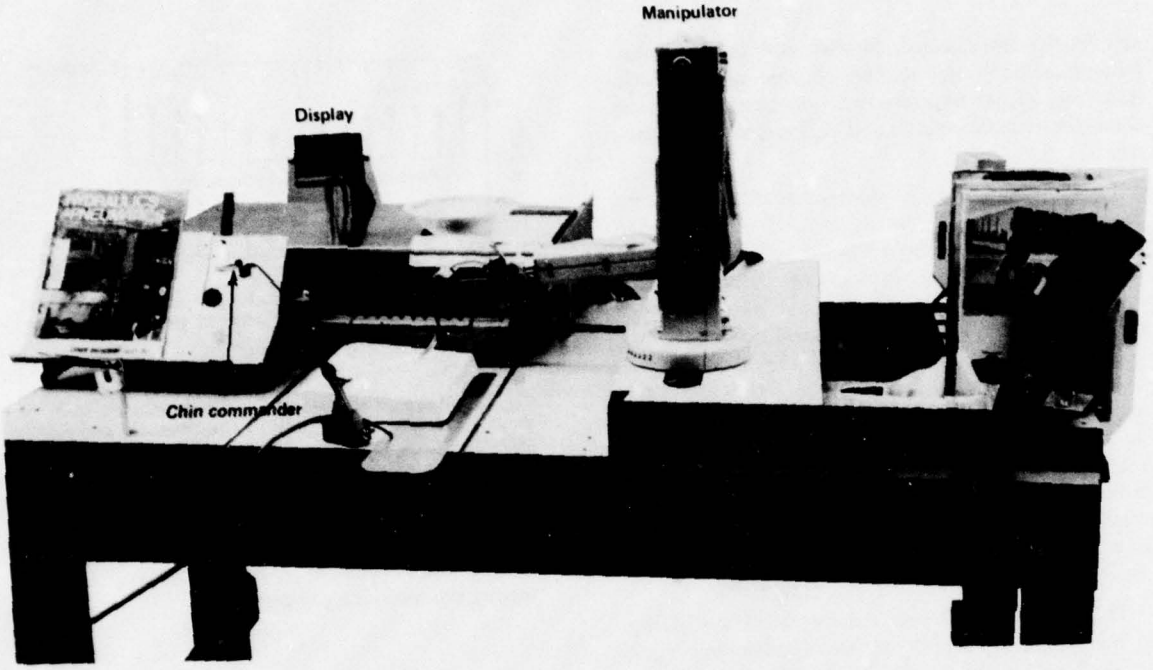

Fig. 1 Medical manipulator positioned on patient's worktable.

far end of the chin loop. Motion in each degree of freedom required selection and termination of that degree of freedom with the discrete command and positioning with the linear command by means of servocontrol.

Complex sequences of motions thus required many mentally demanding command sequences. The need was obvious for preprogrammed command sequences for the unvarying motions associated with many tasks.

DISCUSSION

The decision to use a microprocessor to provide the manipulator with the capability of executing preprogrammed command sequences also provided the opportunity to replace much of the discrete logic and analog control circuitry with microprocessor-executed programmed logic.

The microprocessor was designed to:

1. Scan the six degrees of freedom (or program menu) on the display to provide the patient an opportunity for selection,
2. Monitor the position states of the manipulator for display and control,
3. Update the display when necessary,
4. Monitor the linear and discrete commands for motion control and program sequencing,
5. Control the motion in each degree of freedom so that it is smooth and safe, and
6. Sequence the manipulator through the command sequences of the selected program.

The block diagram of the manipulator (Fig. 2) shows that three motors driven by one driver move the manipulator in six selectable degrees of freedom. All motions except track displacement are executed with cable-driven spring-return mechanisms. Motion in a specific degree of freedom begins with the establishment of a torque balance between motor and spring so that a solenoid lock can be unlatched to allow motion in that degree of freedom. Linear commands from the chin commander are processed to determine the direction and velocity of motion subject to constraints of maximum acceleration, maximum velocity, and position limits. Termination of motion involves deceleration to a minimum velocity to allow a smooth latching of the motion at the nearest latch point.

Position is determined with an 8-bit analog-to-digital (A/D) converter and high-quality potentiom-

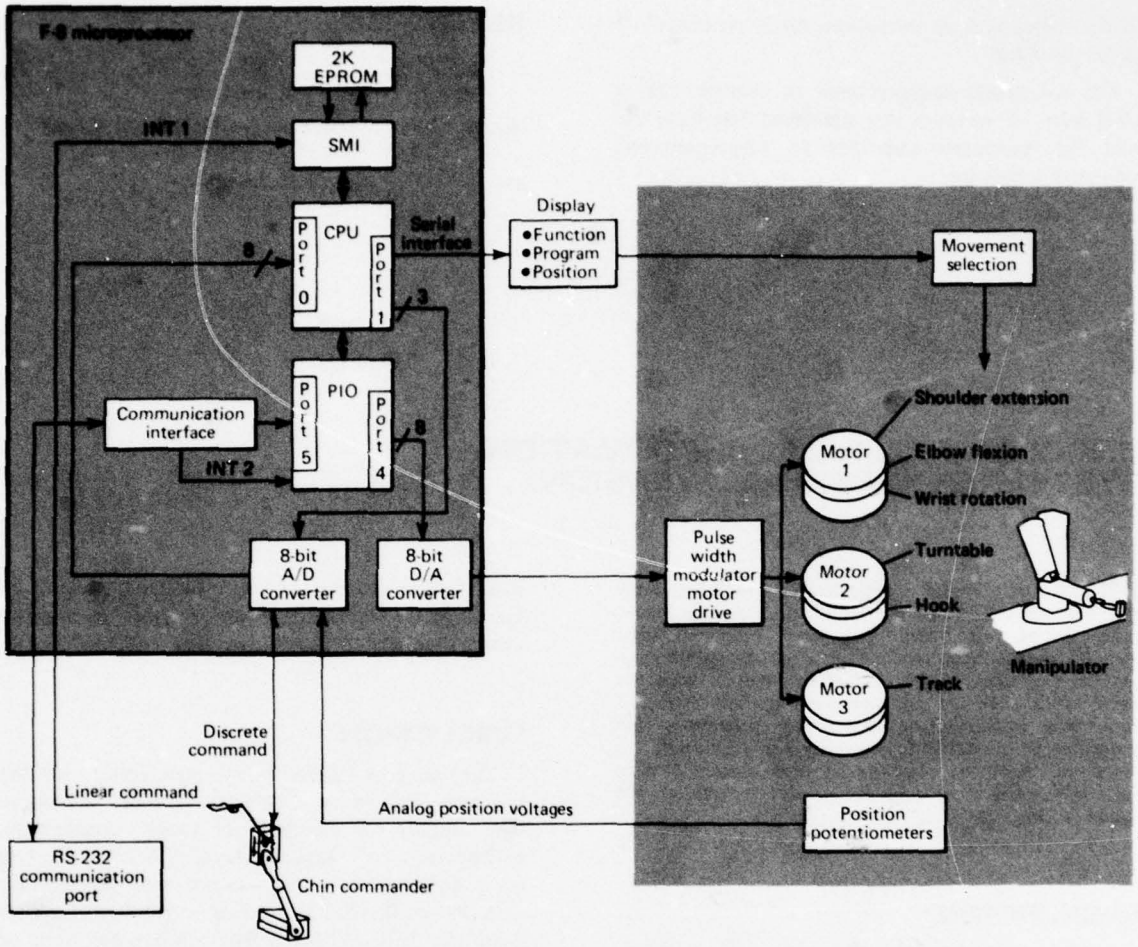

Fig. 2 Block diagram of microprocessor-controlled manipulator.

eters. The digital servomechanism extracts rate information from the position to preclude stalling under varying load conditions. The display and digital manipulator commands are serially updated at 200 Hz when the servomechanism is being used, as is the linear command to the motor driver that comes from an 8–bit digital-to-analog (D/A) converter.

The preprogrammed command sequences are executed by an interpreter that was designed to implement the following instructions:

1. Move in a selected degree of freedom, *D*, to position *P*.
2. Make the transition from programmed mode to manual mode. If *D* is selected in manual mode and the motion proceeds past position *T*, return to the programmed mode and continue the motion to *P*.
3. Branch to any interpreter instruction.
4. Halt program execution until commanded to continue by the discrete command.
5. Exit program to return to manual mode.

The F–8 microprocessor used to implement this particular design is a highly integrated, low-power, 8–bit controller. It consists of a central processing unit (CPU), a static memory interface (SMI), and a parallel input/output chip (PIO). Two interrupts, two clocks, 32 bits of input/output, addressability to

65 536 bytes, and an instruction execution time of 2 μs are provided.

The microcomputer performs its control task in 1500 bytes of memory. An additional 500 bytes are used for interpreter code for 12 preprogrammed command sequences.

REFERENCE

1. W. Seamone and G. Schmeisser, *A Powered Medical Manipulator for the High Spinal Cord Injured Person*, ASME Publication 77/WA/BIO-13, 17 August 1977.

Authors: ***W. Schneider and W. Seamone (APL) and G. Schmeisser, Jr. (JHMI)***

Support: ***Veterans Administration***

ONCOLOGY CLINICAL INFORMATION SYSTEM (PROVISIONAL VERSION)

The use of complex multimodality treatment plans and the necessity for the detailed, precisely timed collection of data quantifying tumor response, drug toxicity, biochemical markers, and other specific parameters of therapeutic evaluation have created the need for a clinically oriented data system than can assist the oncologist in organizing, collecting, and analyzing data related to research and treatment. To serve this need, a prototype computer-based system has been developed and is in routine use at the Johns Hopkins Oncology Center (JHOC).

BACKGROUND

JHOC is one of 18 Comprehensive Cancer Centers established throughout the country as part of the National Cancer Plan initiated by the National Cancer Act of 1971. The Center has major programs in laboratory and clinical research, education at all levels of training, and collaborative activities with community physicians. As part of its clinical activities, it provides cancer patents with specialized care using advanced techniques in chemotherapy, radiation therapy, surgery, and combined modality treatment.

The care of adult patients is centered in a 56-bed facility that also can serve 500 outpatients per week. Inpatients and outpatients are usually managed under the direction of similar, well-defined therapy plans that require the precisely timed administration of drugs and the timely collection of clinical and laboratory data quantifying tumor response, drug toxicity, biochemical markers, and other parameters of therapeutic evaluation. Because of the relative complexity of these plans and the need to maintain records to evaluate an individual's response compared to that of other patients receiving similar treatment, the Oncology Center has developed a prototype information system that is run on the APL computer.

DISCUSSION

The Oncology Clinical Information System (OCIS) has been defined as a network of three subsystems that support the functions of center management, patient care, and radiation therapy. Because funding for a dedicated computer was not immediately available, it was decided to develop a provisional system using the APL computer. The primary objectives of this provisional system are to provide useful support in patient management, to give designers and users an opportunity to refine system requirements, and to develop a data base for later versions of the system.

OCIS operates as an adjunct of the Johns Hopkins University Medical Information System, which provides on-line support in the areas of admissions, outpatient registration, inpatient drug distribution, and retrieval of selected clinical data such as radiology reports. The system also performs all billing functions and produces a variety of management reports. Thus, the capabilities of the prototype system are limited to supporting functions unique to the Oncology Center. The organization of the patient data base, the type of data displays and reports available, and potential uses of the system are discussed briefly below.

The patient data base is organized into three levels. The highest level contains summary information about all patients treated for cancer at Johns Hopkins

since 1964. Data for more than 20 000 patients are stored in records that contain identification, coded diagnoses, dates, and follow-up information. Because the data base may be listed in several categories, there is a search and tabulation capability. The primary purposes of this file are to serve as a master index to the paper records, to assist in follow-up of cancer patients, and to identify subsets of the data base for further analysis.

The second data level contains a complete abstract for each new Johns Hopkins Hospital cancer patient. A data base of 4000 abstracts has been accumulated since the initiation of OCIS. Each abstract gives all the data required by the Hospital Tumor Registry and serves as a nucleus for the Oncology Center patient records. The file combines fixed formatted information, coded information, and free text. A portion of a sample abstract is shown in Fig. 1.

The third level contains clinical data such as test results, medications, vital signs, and blood products. Such data are collected for all patients treated at JHOC and are available for almost 1000 patients.

The main purpose in collecting the clinical parameters is to produce effective data displays in order to understand the therapy process better. The provisional system prepares plots and flow sheets to display key

```
JOHNS HOPKINS HOSPITAL                    HISTORY NO:
ONCOLOGY CENTER                           NAME:
                                          DATE: 03/23/77

                                  PHONE                    CLASS  ONC
                                  SPOUSE
BALTIMORE, MD 21222               BIRTH DATE
ADMITTED  05/05/58    DISCHARGED  06/02/58
SEX  F    RACE  NON-W    MAR. STATUS  MARRIED      SERVICE  M


DIAGNOSIS

|     JHH DIAGNOSIS        05/58
|
|170    MALIGNANT NEOPLASM OF BREAST
|8502.3 INTRADUCTAL CARCINOMA EXTENT: REGIONAL
|
|BASIS OF DXI PATHOLOGY
|CARCINOMA OF RT. BREAST
|
|8500-2194 INTRADUCTAL AND SCIRRHOUS CARCINOMA WITH LYMPHOID STROMA.

| TREATMENT

|  FROM     TO   | TYPE | PURP | LOC | RSLT | COMP | DESCRIPTION
|05/07/58        | SURG | CUR  | JHH |      |      | NOTE  1
|05/58           | RAD  | CUR  | JHH |      |      | NOTE  2
|  NOTES
|  1 RIGHT RADICAL MASTECTOMY
|
|  2 5750R TO SUPRACLAVICULAR AREA.

HISTORY

|MEDICAL HISTORY      PARA 2002
|ONSET OF SYMPTOMS    MASS IN LEFT BREAST X 2 1/2 MONTHS
|OCCUPATION           CLERK
```

Fig. 1 Portion of sample abstract.

data interactions. Figure 2 is a semilog plot of platelet count, P, and white cell count, W, versus time. The plot also shows the interrelationships among

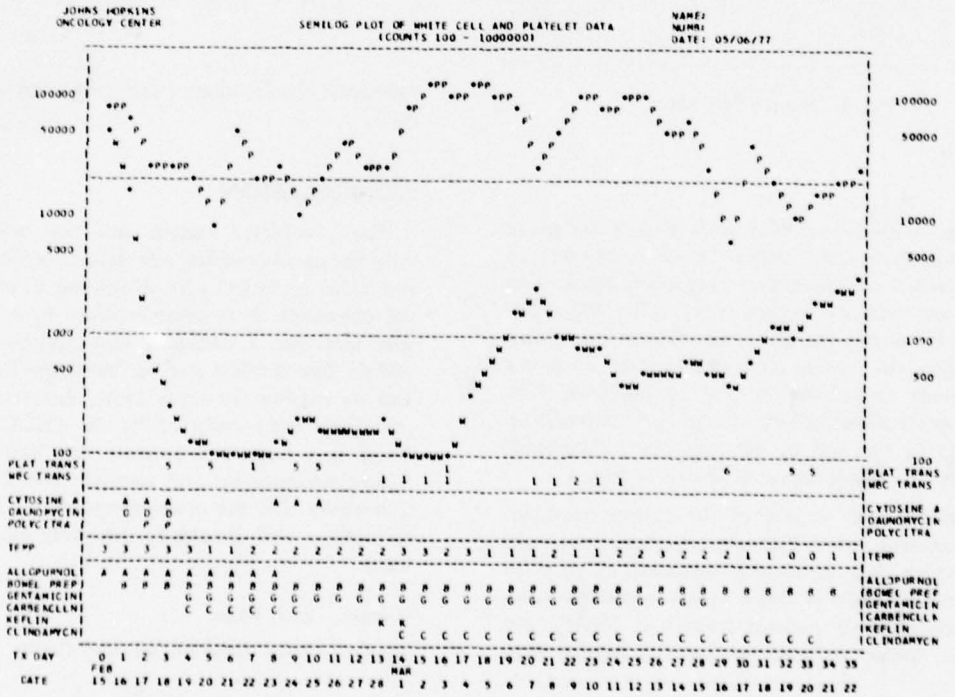

Fig. 2 Sample plot of white cell count and platelet data versus time.

platelet and white blood cell transfusions, chemotherapy, temperature (degrees above 37°C), and antibiotics. Alternate plot formats create histograms or scatter plots.

In addition to generating plots, the system also produces flow sheets that contain either a general summary or a detailed survey for a specific organ system. Depending on their use, flow sheets can be printed horizontally (Fig. 3) or vertically.

JOHNS HOPKINS ONCOLOGY CENTER

HISTORY NO: 0000000
NAME: DEMONSTRATION
DATE: 09/23/77

STANDARD FLOW SHEET

1975		MAR 4 WK 0	MAR 11 WK 1	MAR 18 WK 2	MAR 25 WK 3	APR 1 WK 4	APR 15 WK 6	MAY 6 WK 9
HEMATOLOGY								
HCT	%	39.0	37.0	35.0	36.0	36.0	36.0	36.0
WBC		9300	5910	4000	4900	4200	4500	4000
NEUTROPH	%							
LYMPHOCYTE	%							
PLATELETS	/MM3	2930000	2400000	2120000	2750000	2970000	1380000	
RETICLCYTE	%							
BLOOD PROD								
PLAT TRANS								
RBC TRANS								
WBC TRANS								
STATUS								
TEMP	DEG C	97.3	99.3	99.8	98.8	98.8	98.6	97.8
BODY WT AM	KG	67.4	67.3	66.6	68.8	68.8	67.9	67.3
LABORATORY								
SER UR NIT	MG/DL	18			14			18
SER CREAT	MG/DL	1						1
SER ALKPHO	U/L	70			21			30
SGOT	U/L	14			13			15
SGPT	U/L	1			1			1
LDH	U/L	350			300			420
SER UR ACD	MG/DL	5.9			6.0			5.3
TOT SER PT	GM/DL	7.9			7.9			7.2
SER ALBUMN	GM/DL	4.5			4.4			4.6
AMN PROT	GMS	1			1			1
SER CA	MG/DL	9.0			8.0			9.2
SER PHOS	MG/DL	3.7			3.3			4.3
TOT BILI	MG/DL	0.3			0.3			0.3
CHEMOTHER								
BCNU	MG	17			17		17	17
CYTOXAN	MG	1700.00			1700.00		1700.00	1700.00
VINCHIST	MG	2.0			2.0		2.0	2.0
PHENDNISONE	MG	750.0			750.0		750.0	500.0
MEDICATION								
OTHER MEDS								

Fig. 3 Sample flow sheet.

Finally, a special set of reports is prepared from the microbiology data. Because time is required to grow a culture and identify an organism, results frequently are delivered several weeks after the specimen has been collected. To make effective use of this information, the reports are sorted by date, by source of specimen (e.g., blood), and by organism. The sorted reports allow the physician to trace an organism from site to site and to note changes in antibiotic sensitivity. A sample report is shown in Fig. 4.

The provisional version of the system maintains an appointment system that schedules outpatient visits and prepares data summaries automatically prior to patient visits. There is also a census system to maintain records of all patients treated at JHOC, and there are special programs to support facility management, platelet donor matching, and other functions.

JOHNS HOPKINS ONCOLOGY CENTER

HISTORY NO:
NAME:
DATE: 03/16/77

SORTED BY SPECIMEN

DATE	SPECIMEN		REPORT	MP EC T 23 AG K+
01/12/77	NASAL	1	CANDIDA ALBICANS	
01/14/77	MOUTH	1	CANDIDA ALBICANS 2 DAYS	
01/01/77	STOOL	1	NG 2 DAYS	
01/12/77	STOOL	1	NO GENT RES ORGANISMS ISOLATED	
02/02/77	STOOL		STAPHYLCOCOCCUS ALBUS	AC AA A DA
12/20/76	BLOOD	1	NG 29 DAYS VIRAL CULTURE	
12/28/76	BLOOD	1	NG 2 WKS	
01/05/77	BLOOD	1	NG 1 WEEK	
01/05/77	BLOOD	1	NG 2 WKS	
01/05/77	BLOOD	2	NG 2 WKS	
01/11/77	BLOOD	1	STAPHYLOCOCCUS EPIDERMIDIS	AB AA A AA
01/23/77	BLOOD		NG CULTURE 2 WKS	
01/24/77	BLOOD		NG CULTURE 2 WKS	
01/26/77	BLOOD		RHI-BR GRAM POSITIVE COCCI	
02/03/77	BLOOD		RHGTS GRAM POSITIVE COCCI	
02/03/77	BLOOD		STAPHYLCOCOCCUS ALBUS	AC AA B DA
12/21/76	URINE	1	NG 28 DAYS VIRAL CULTURE	
12/28/76	URINE	1	<10000COL/ML	
01/05/77	URINE	1	NG <1000 COL/ML	
01/12/77	URINE	1	NG 1 WK	
01/12/77	URINE	1	NG 1 DAY	
12/20/76	CSF	1	NG 2 WKS	
12/20/76	CSF	1	NG 29 DAYS VIRAL CULTURE	
12/20/76	BMARR	1	NG 29 DAYS VIRAL CULTURE	
01/01/77	CATH	1	NG 1 WK	
02/02/77	FUNGA		CANCIDA ALBICANS FUNGAL CULTURE	
01/12/77	NASCP	1	CANCIDA ALBICANS	
12/20/76	RECTA	1	NO GENT RES ORGANISMS ISOLATED	
01/05/77	RECTA	1	NO GENT RES ORGANISMS ISOLATED	

M PEN	.2	.4	.8	1.6	16+	T TET	1	2	4	16	16+	G GEN	1	2	4	8	8+
P PEN	0.1	1	4	16	16+	C CPL	2	-	4	8	8+	K KAN	2	4	8	16	16+
E ERY	0.5	1	2	-	2+	S CEP	0.5	2	8	32	32+	N TOB	1	2	4	8	8+
C CLN	0.5	1	2	8	8+	A AMP	1	2	4	16	16+		A	B	C	D	E

Fig. 4 Sample bacteriology report.

CONCLUSION

The provisional system was put into operation with the opening of the new JHOC facilities in October 1976. In its first year, it satisfied all of the principal objectives. It is being replaced by a second version that uses a dedicated minicomputer located at JHOC. The medical staff is familiar with the system and its outputs; in many cases, disease-specific outputs have been designed by the JHOC physicians. There is a large and accurate data base to support patient management and research. Moreover, the requirements for the next-generation OCIS are well understood and should be relatively easy to implement.

Author: ***B. I. Blum***

Support: ***Johns Hopkins Oncology Center***

CALIBRATION OF RADIATION ONCOLOGY TREATMENT MACHINES

Emphasis on excellence of treatment in radiation oncology requires a major physics and engineering effort in operating and calibrating large linear accelerators used for therapy. During the preceding year, all major therapy machines in the Johns Hopkins Oncology Center were calibrated and are now in use. In addition, the elements of a quality-control program for accurate dose delivery were formulated and initiated. Future efforts will entail consolidation of the various activities into a unified program that includes machine maintenance and calibration, treatment planning, clinical dosimetry, and periodic dose verification to assure the high degree of excellence demanded in a modern radiation oncology facility.

BACKGROUND

The new radiation oncology wing of the Johns Hopkins Oncology Center opened in 1977. The facility has three major high-energy therapy machines. A Siemens ^{60}Co teletherapy unit with a nominal photon energy of 1.25 MeV is the facility's only isotopic gamma-ray source. In addition, two linear accelerators have been installed: a Varian Clinac–4 linear accelerator that produces X rays at 4 MeV and a Clinac–18 linear accelerator that produces X rays at 10 MeV and electrons at 6, 9, 12, 15, and 18 MeV. The three machines and a diagnostic simulator are now operational. More than 100 patients per day are being treated in the Center.

DISCUSSION

Before the machines were used, it was necessary to measure the dosage supplied by the beams. Initially, the dose rate of each machine was calibrated absolutely by measuring the beam ionization produced in a water phantom (equivalent to tissue) under standardized conditions. Baldwin-Farmer ionization probes and electrometers calibrated at the National Bureau of Standards were used to convert the measured ionization to absorbed dose.

In addition to the absolute calibration, relative dose measurements were made on each machine to define the treatment beam parameters. These data were obtained by driving a scanning probe (under computer control) through a water phantom that was being irradiated. This established the relative dose versus depth and also the relative dose over the lateral beam geometry. The data have been computerized and are used for the detailed planning of each patient's treatment by means of computer modeling. This work required approximately eight months of intensive effort.

A major program has been initiated to ensure dose accuracy and the repeatability of treatment. The major elements of the program are:

1. An aggressive preventive maintenance program consisting of daily checks of specific parameters and quarterly checks by the vendor of the therapy machine;
2. Daily checks for constancy and symmetry of the output level of the beam, by means of diodes, plus weekly checks by means of ionization chamber measurements;
3. A comprehensive weekly review of all patient charts for dose verification; and
4. An extensive program in clinical dosimetry (i.e., measurement on the patient) using diodes and thermoluminescent dosimeters (LiF).

Many of these elements are being incorporated into a computerized dose-quality-control program that will be the basis of a model system. The new system will include computerized chart checks and an automatic dose-measuring system.

In addition, all treatment planning and dose calculation algorthims are being reviewed in a continuing effort to maintain a library of only the most up-to-date computational techniques.

An investigation of the dosimetry of total-body-irradiation (TBI) patients is under way. Isodose contours of dose levels through various body sections have been obtained for adult- and child-size phantoms. The responses of hundreds of dosimeters placed in the life-size phantoms are processed and the data (plane by plane) are interpolated to establish the isodose pattern.

As a part of the overall program, a physics course appropriate for technologists and residents has been initiated. It is presented as part of the accredited Technologist School.

Authors: D. G. Grant (APL) and W. C. Lam (JHOC)

Support: Johns Hopkins Hospital

THE PATIENT MONITORING SYSTEM AT THE JOHNS HOPKINS ONCOLOGY CENTER

A complete physiological monitoring system has been installed and is operating at the Johns Hopkins Oncology Center. It provides information on basic vital signs at a bedside panel and also in central nurses' stations for all rooms in the 56–bed inpatient facility of the Johns Hopkins Oncology Center. The system meets physician/patient requirements and has improved patient care significantly.

BACKGROUND

The physiologic monitoring of patients covers an extreme range of physician/patient requirements. On the one hand, physicians require fundamental data such as electrocardiogram (ECG), respiration rate, heart rate, temperature, and blood pressure in a format that provides predictive trends and also has an alarm mode. On the other hand, the patient should be encumbered as little as possible in the gathering of such data and, in particular, should remain ambulatory if possible.

DISCUSSION

The Johns Hopkins Oncology Center is a 56–bed facility situated on two floors and serviced by four nurses' stations. Each nurses' station, the focal point of the patient monitoring system, serves 14 to 16 rooms. All rooms function identically (Fig. 1). Patient monitoring panels behind the bed relay some signals (temperature and infusion pump alarm) directly to the nurses' station and relay others (primarily ECG and blood pressure) to a second wall panel located in a position somewhat removed from the bed. This second relay panel is connected to a bedside cart that contains a modular amplifier for physiologic signals. The amplified signals are transmitted through the same panel to the central nurses' station. Each room has a pair of 36–conductor cables leading back to the nurses' station.

The Oncology Center monitoring system has provided for 16 hardwired ECG channels, 9 telemetry ECG channels, 15 respiration-rate channels, 16 heart-

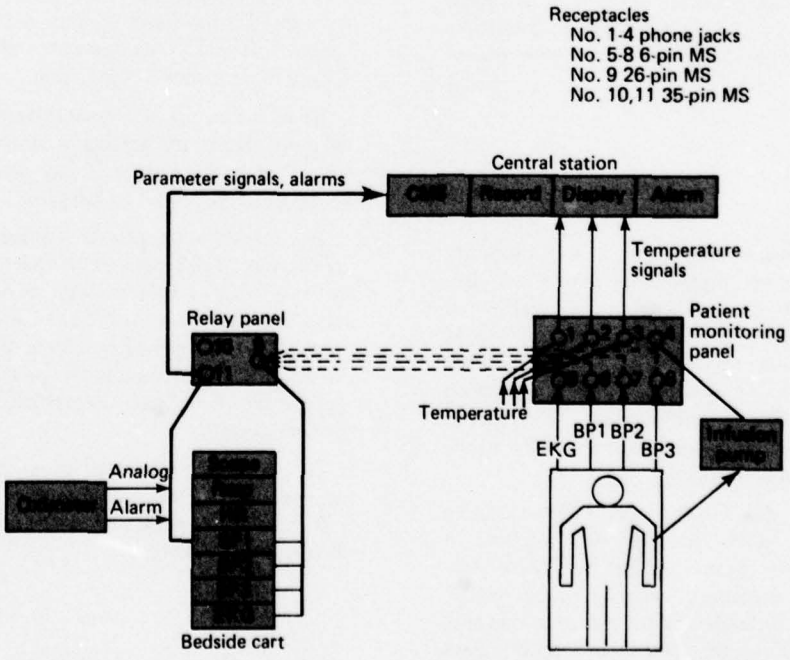

Fig. 1 Schematic of patient monitoring system.

rate channels, 9 pressure-monitoring channels, 2 sphygomomanometer channels, and 1 oximeter channel (two additional channels have been ordered), all of which can be distributed flexibly among all the patient rooms. Also, up to three simultaneous temperature channels are available from each room.

Installation of the patient monitoring system is 95% complete. Two cart formats, acute and intensive, are available, depending upon the severity of the illness. Signals for ECG (both hardwire and telemetry), heart rate, respiration rate, arterial and venous blood pressure, and patient temperatures are available. All vital physiologic signals have variable upper and lower alarm thresholds. Visual scope displays and chart recorders facilitate data interpretation. Future plans include more extensive applications of data telemetry.

Authors: ***D. G. Grant (APL) and E. Hertz and D. M. Riker (JHOC)***

Support: ***Johns Hopkins Hospital***

URBAN TECHNOLOGY

INTRODUCTION

The recognition that the great cities continue to play a key role in maintaining the vitality of the nation has spurred renewed interest in the institutional structures that support urban life. Through a variety of special projects, APL has participated in and contributed to programs directed at developing and applying modern technology to a variety of civil problems directly relevant to current urban issues. These programs have included transportation, fire research, siting of power plant facilities near urban centers, health care delivery systems, and, more recently, location of leaks in buried natural-gas distribution lines. While not all of these program areas are included in this section, several are brought together here in an effort to provide a unifying perspective on their scope and their relationship to urban life.

The articles in this section relate specifically to public transportation and to questions of public safety. The article on short-headway (hence, potentially high volume) automated guideway transit systems represents APL's continuing interest in improving urban transportation via systems analysis and technological innovation.

The article on leak detection in buried natural-gas distribution lines concerns safety and resource conservation. The explosion hazard from leaking buried gas distribution lines has been well documented, and several unsuccessful engineering attempts have been made to develop methods of pinpointing leaks.

However, the need for an effective method continues to increase since throughout the United States the gas distribution systems have reached the age where sharp increases are projected in the mean annual leak rate per mile. The APL program is directed at analyzing the active acoustic method as the only viable current method of leak detection. The project is both theoretical and experimental but, unlike prior attempts, has a research orientation and includes studies of acoustic propagation in soils, instrumentation development, and theoretical analysis.

The last two articles describe different aspects of the APL Fire Program. The first concerns the combustion characteristics of materials commonly involved in fire, including the quantitative determination of surface ignition temperatures and combustion products. The second concerns the clinical and technical evaluation of fire-related deaths. This work represents the broader Laboratory involvement in fire technology and fire-fighting tactics. The development of new materials for construction, including some that produce toxic agents on burning, has increased the threat of fire to both occupants and fire fighters. The mortality aspect of the APL program attempts for the first time to quantify specific contributors to deaths. A third component of this program concerning documentation and dissemination of information related to fire appeared in previous *Accomplishments*.

DATA RATE AND QUANTIZATION REQUIREMENTS FOR A SHORT-HEADWAY VEHICLE-FOLLOWER AGT SYSTEM

An important consideration in designing Automated Guideway Transit (AGT) Systems is the communication requirements for longitudinally controlling vehicles. Thus, trade-off studies are required to establish the communication data rates and accuracies needed to maintain an acceptable level of vehicle performance.

BACKGROUND

Vehicle following in an AGT system is a longitudinal control scheme in which the state of a vehicle is determined by the state of the immediately preceding vehicle. It has been shown (Ref. 1) that at headways (the time between successive vehicles passing a fixed point on the guideway) of less than 3 s, a fundamental kinematic constraint creates bounds on vehicle motion. This constraint dictates a minimum allowable spacing between vehicles that is a function of trailing vehicle state, preceding vehicle state, and the future maneuvering capability of each vehicle.

The difficulties encountered in controlling a vehicle subject to the kinematic constraint have been resolved by the use of a controller that is a nonlinear function of states (Ref. 2). The approach presented in Ref. 2 explicitly incorporates the kinematic constraint into the control law and consequently provides near-optimal performance while satisfying safety requirements under all operating conditions. The control law thus provides a baseline system for studying the effects upon vehicle performance of sampling, quantization, and time delays associated with intervehicle communication and control computation.

To implement a longitudinal control law, there are many ways to configure the overall system, that is, to measure vehicle states, to transmit this information between vehicles, and subsequently to control the individual vehicles. As a result, the problem of the required data rate creates various trade-offs related to vehicle/wayside control allocation and on-board digital/analog (D/A) interfacing. Control allocation determines whether control loops should be closed on board the vehicle (a "smart" vehicle) or through the wayside (a "dumb" vehicle). The specification of the many parameters involved in the problem is approached through analytically derived results using simplified linear models and then verification and expansion of these results with a detailed computer simulation.

DISCUSSION

The general system configuration that will be considered for this study is shown in Fig. 1. An on-board digital computer receives information from the wayside that is sampled, quantized, and delayed. The on-board digital/analog interface determines how much of the on-board control computation is performed digitally. The figure reflects a smart vehicle configuration where all control computation is performed on board the vehicle and where preceding vehicle information is received from the wayside in the form of spacing and its derivatives (relative velocity and acceleration). A dumb vehicle configuration would allocate control computation to a wayside computer. The parameters considered in this study that affect sampling rate and quantization requirements are:

1. Headway (0.5 and 3 s);
2. Smart or dumb vehicle;
3. On-board sampling interval;
4. Wayside sampling interval;
5. Bit number to represent wayside information;
6. Bit number for on-board computation;
7. Location of D/A conversion on board;
8. Bit number for D/A conversion; and
9. Inclusion of analog filtering following D/A conversion.

The first phase of the study was to consider closed-loop stability as a function of headway, wayside sampling rate, and control allocation. A z-transform analysis in conjunction with root locus plots is used for this purpose. From a stability viewpoint, the effects of sampling are more strongly related to the jerk and acceleration limits on the vehicle rather than to the particular operating headway. This is because the control law derivation is based on the kinematic constraint and thus controller bandwidth is largely determined by the gains that reflect this constraint, independent of headway.

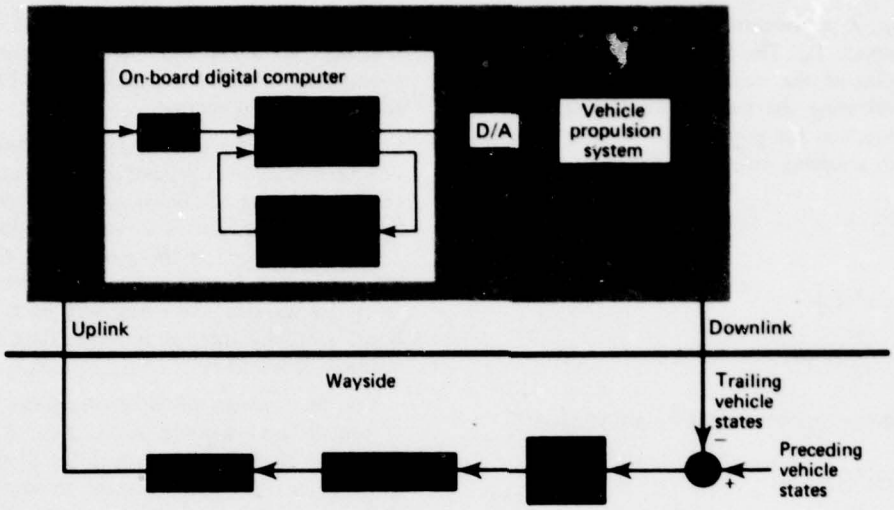

Fig. 1 General system configuration.

Another result of the analysis is that a smart vehicle offers an advantage over a dumb vehicle in that the required sampling rate from the wayside is lowered. For a service jerk limit (nonemergency) of 2 m/s³ and a service acceleration limit of 1.5 m/s², a dumb configuration requires a sampling interval of 0.35 s to maintain stability at a 0.5–s headway (Ref. 3). On the other hand, for a smart vehicle this requirement is relaxed to a sampling interval of 0.6 s. At a 3–s headway, the requirements are 1 s for a dumb vehicle and 2 s for a smart vehicle. Consequently, at either headway there is approximately a twofold reduction in the required sampling rate when a smart vehicle configuration is used.

The question of setting quantization requirements becomes more complex because of the many factors that influence the resulting noise levels. To determine the number of bits required for on-board computation and wayside information, a statistical analysis is used with quantization noise added at selected points in the linear model. A covariance propagation equation is derived, thus providing the variance in vehicle acceleration as the performance measure. The parameters considered are the on-board bit number, bit number for D/A conversion, wayside bit number, wayside sampling interval, and on-board sampling interval.

A linearized model of the closed-loop system with discrete vehicle dynamics may be represented as in Fig. 2. The index, i, represents updates at the on-board sampling interval, T_v. The discrete time state

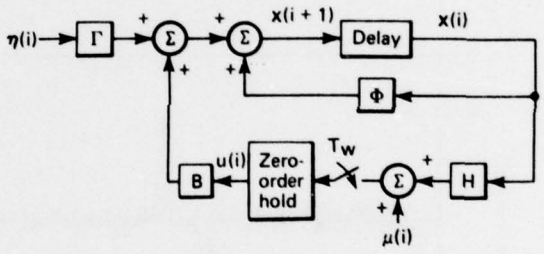

Fig. 2 General form of closed-loop system.

equations are then given by

$$\mathbf{x}(i+1) = \Phi\mathbf{x}(i) + \Gamma\eta(i) + Bu(i)$$

and

$$u(i) = H\mathbf{x}(k) + \mu(k)$$

where

$\Phi = n \times n$ system matrix.

$\mathbf{x} = n$-dimensional state vector,

$\Gamma = n \times m$ matrix,

$\eta = m$-dimensional vector of state noise,

u = scalar input,

μ = noise representing A/D conversion noise on wayside inputs,

$H = 1 \times n$ vector,

$B = n \times 1$ vector,

and the index, k, represents updates at the wayside sampling interval, T_w. The input, $u(i)$, is constant over N samples of the on-board computer; $T_w = NT_v$. By evaluating the state at wayside sampling instants, an equation for propagation of state covariance at wayside sampling instants is (Ref. 3)

$$P(i + N) = FP(i)F^T + G \qquad (1)$$

where

$$P(i) = E[\mathbf{x}(i)\mathbf{x}^T(i)]$$

$$F = \Phi^N + \sum_{j=0}^{N-1} \Phi^j BH$$

$$G = \sum_{j=0}^{N-1} [\Phi^{N-1-j}\Gamma Q(\Phi^{N-1-j}\Gamma)^T + \Phi^j BM\,(\Phi^j B)^T]$$

$$Q = E[\eta(i)\eta^T(i)]$$

$$M = E[\mu(i)\mu^T(i)].$$

Consequently, for given Q, M, and sampling intervals T_v and T_w, we first compute the matrices F and G. For an initial covariance $P(0) = 0$, the state covariance may be propagated using Eq. 1 to determine a steady-state noise level as a function of various quantization levels and sampling rates of the on-board and wayside computers.

With the above technique, the trade-offs between various digital/analog interfaces and sampling intervals are determined. Based on the results in Ref. 3, the selected configuration requires 8 bits for D/A conversion (placed at the acceleration command), 8 bits for on-board computation, and a total of 25 bits from the wayside. At a headway of 0.5 s, the on-board sampling interval is set at 0.02 s; for a 3-s headway, it is 0.05 s.

The final system problem considered is the effect of time-delayed wayside information. A modified z-transform analysis with root locus plots is used to demonstrate the rapid increase in system damping with increased time delay. From the simulation it is found that at a 0.5-s headway, a 0.05-s time delay may be tolerated with a 0.1-s wayside sampling interval. At a 3-s headway, a 0.5-s delay with a 1-s wayside sampling interval is acceptable.

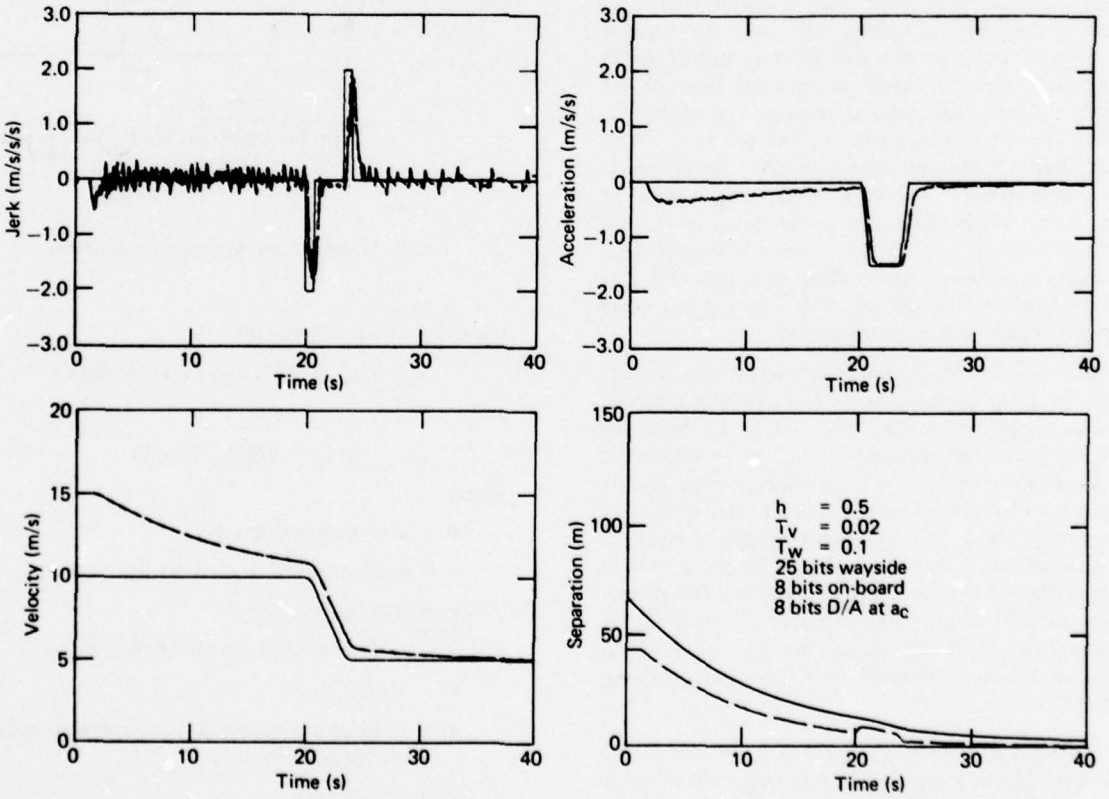

Fig. 3 Simulation example.

All the results have been verified with a detailed computer simulation of the system. The simulation includes quantization of wayside information, D/A conversion on board, and quantization at various stages of the on-board control computation. A separately excited DC motor model is used for the propulsion system, including nonlinear effects due to aerodynamic drag. An example of the system response with sampling and quantization is shown in Fig. 3. A trailing vehicle (dashed line) traveling at 15 m/s is overtaking a preceding vehicle (solid line) traveling at 10 m/s with an initial separation (tail to nose) of 67 m. The dashed line on the separation plot represents the kinematically required separation (which must always be less than the actual separation). At 20 s, the preceding vehicle decelerates on jerk and acceleration limits to a speed of 5 m/s. The resulting noise level is most pronounced on the plot of vehicle jerk and is within acceptable bounds.

Continuing study in this area includes further tradeoffs in terms of vehicle-wayside control allocation. All allocation computations considered in this study were performed either on board or at wayside. However, there are alternatives in which some information may be combined at wayside before being transmitted to the vehicle. Another major assumption in this work was the existence of ideal measurements of position, velocity, and acceleration. Hence, the effects of measurement noise will be studied to determine, for example, whether states may be estimated from position measurements alone.

REFERENCES

1. G. B. Stupp, H. Y. Chiu, and S. J. Brown, "Vehicle Following Control with Variable Gains for Short Headway Automated Guideway Systems," *J. Dyn. Sys. Meas. Control* 99, No. 3, September 1977, pp. 183–189.
2. A. J. Pue, "A State-Constrained Approach to Vehicle-Follower Control for Short Headway Automated Transit Systems," *Proc. Joint Automation Control Conf.*, San Francisco, CA, June 1977.
3. A. J. Pue, H. Y. Chiu, and S. J. Brown, APL/JHU TPR-041 (to be published).

Author: ***A. J. Pue***

Support: ***DOT Urban Mass Transportation Administration***

ACTIVE ACOUSTIC DETECTION OF LEAKS IN UNDERGROUND NATURAL-GAS DISTRIBUTION LINES

The most promising technique now being investigated for the detection of leaks in buried natural-gas pipelines is the active acoustic method. In support of an APL research program to provide fundamental information required in developing an optimal system of active acoustic leak detection, a theoretical and experimental investigation was made of the radiation accompanying the propagation of acoustic waves within an underground pipe. The investigation has shown that the radiated field consists of both shear and compressional waves. This result is significant because the coherent radiation from the pipe walls represents the largest obstacle to reliable leak detection by the active acoustic method. In a related development, a sensitive, non-earth-loading laser interferometer that can be used in the field has been developed to measure earth vibrations.

BACKGROUND

The detection of leaks in residential natural-gas distribution lines is a matter of concern to both industry and federal regulatory agencies. A research effort directed toward understanding the fundamentals of the active acoustic detection of leaks has been conducted at APL (Ref. 1). In this promising method, sound is injected into the pipe and the leak is detected by measuring displacements of the earth's surface caused by radiation emanating from the leak.

The program at APL consists of: (a) an experimental field test that makes use of an abandoned water line on the APL property to study radiation

from the walls of nonleaking and leaking pipes, (b) a theoretical investigation of elastic waves radiated from underground piping due to vibration generated by coupling of the pipe walls to the internal acoustic pressure variations and from leak-radiated signals, and (c) the development of improved detection instruments for measuring vibrations of the earth's surface.

In this article, we describe the results of an experimental and theoretical study of radiation from the vibrating walls of a buried, nonleaking pipe (Ref. 2). This problem is important to the overall effort because background radiation from the walls of a nonleaking pipe was the major reason previous investigators failed to develop an active acoustic leak-detection system. A portable field instrument for detecting vibrations of the earth's surface by optical means is also described.

DISCUSSION

Surface acceleration accompanying the propagation of plane progressive sound waves within an air-filled pipe was measured as a function of frequency by means of surface-mounted accelerometers. The pipe, a 20-year-old abandoned water line approximately 1000 ft long with an inside diameter of 2 in. and a wall thickness of 3/16 in., is buried 30 to 36 in. deep in clay earth. Before the pipe was instrumented, it was dried by pumping and was tested for leaks; none were found. The acoustic source was a standard electromagnetic unit of the type used to drive horns in public address systems. It was impedance-matched to one end of the pipe. Surface accelerations were measured by means of a Brüel and Kjaer type 5698 accelerometer located 122 ft from the driver and directly above the pipe. Checks were made throughout the course of the experiments to ensure that the disturbance measured at the surface of the earth was due to the transmission of acoustic energy in the gas within the pipe and not from the steel walls.

The results of a typical series of measurements are shown in Fig. 1 for pipe depths of 30 and 12 in. The accelerometer output, E_A, in microvolts is plotted against frequency. During these measurements, the sound pressure level at the driver was held constant at approximately 140 dB relative to 2×10^{-4} dyne/cm^2. The drop-off in signal with frequency is caused mainly by attenuation in the gas within the pipe, attenuation in the earth medium, variation in accelerometer sensitivity, and the mismatch of accelerometer impedance relative to that of the earth. The last two factors make it desirable to develop an alternative method (other than accelerometers) to measure earth displacements. The important thing to note in this figure in the case of the 30-in. pipe depth is the series of maxima separated by about 400 Hz, indicative of an interference phenomenon.

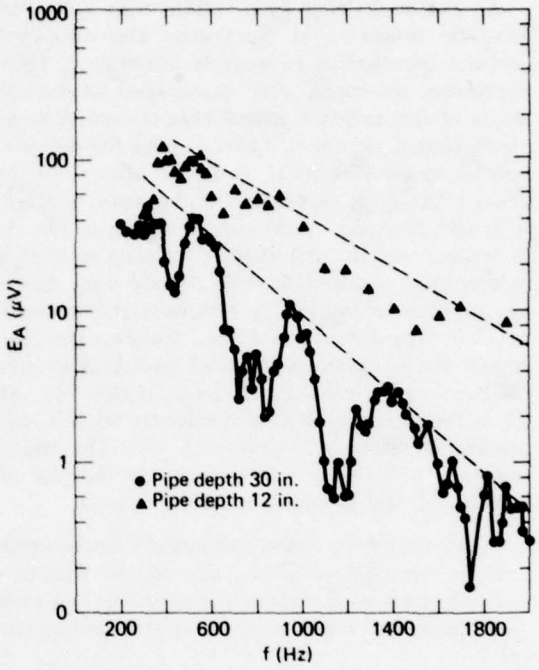

Fig. 1 Accelerometer output plotted as a function of frequency.

The case of an infinitely long steel pipe buried in earth modeled as an isotropic homogeneous elastic half-space was considered theoretically. The gas within the pipe conducts a plane pressure wave that induces radial and longitudinal displacements of the wall. These displacements excite compressional and shear waves in the earth medium that satisfy the wave equations (Ref. 3)

$$\nabla^2 \phi = \frac{1}{\alpha^2} \frac{\partial^2 \phi}{\partial t^2} \qquad (1)$$

and

$$\nabla^2 \psi = \frac{1}{\beta^2} \frac{\partial^2 \psi}{\partial t^2} \qquad (2)$$

giving the compressional and sheer potentials of ϕ and ψ, respectively. Here, α is the compressional wave velocity and β the sheer wave velocity; t is time. These velocities are related to the elastic constants of the earth medium.

The problem is solved by first determining the amplitudes of the radiated cylindrical waves satisfying Eqs. 1 and 2 by matching the boundary conditions at the pipe/earth interface. The waves radiate to the surface where, directly over the pipe, they are reflected as bulk shear and compressional waves, the magnitudes of which are determined by the existing boundary conditions (the vanishing of normal and tangential stresses). The radial and longitudinal displacements at the earth's surface directly over the pipe are given in terms of the incident and reflected compressional and shear potentials.

Theoretical vertical displacement is shown in Fig. 2 where the displacement, $|w|$, is plotted versus frequency for the case of a pipe buried 30 in. deep. The experimental vertical displacements also plotted in Fig. 2 were obtained by correcting the data in Fig. 1 for the aforementioned attenuation and accelerometer sensitivity and mismatch factors (Ref. 2). It is noted from Fig. 2 that the level of wall radiation from a buried pipe can be accounted for, within a factor of two, by means of theory, i.e., axisymmetric vibration of the pipe walls. This result stands in marked contrast to similar experiments with pipes in an air medium. There, radiation levels exceeded those due to axisymmetric excitation by more than an order of magnitude (Ref. 4) and have been found to be generated by coupling into the transverse bending modes. It is concluded that bending vibrations of a buried pipe must be strongly damped.

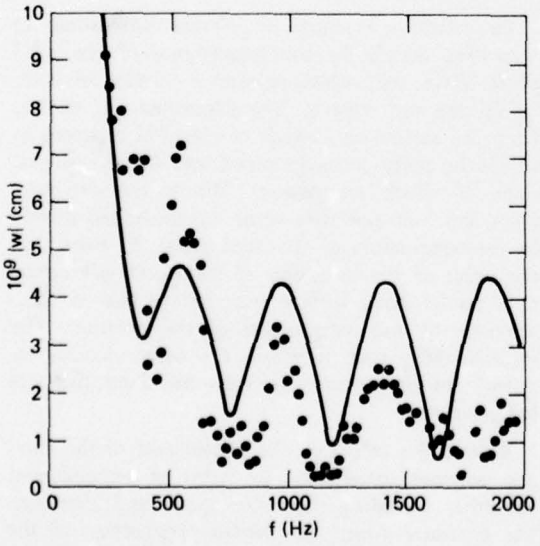

Fig. 2 Comparison of calculated and experimental values of earth surface displacement.

Another important result is that the amplitudes of the compressional and shear waves generated by the pipe wall vibration are comparable, leading to the interference evidenced by the experimental data. Values of the compressional and shear wave velocities, α and β, were chosen to give the best fit between theory and experiment. To the authors' knowledge, values of α and β *in situ* were never previously determined simultaneously.

In order to eliminate problems associated with surface-mounted accelerometers, a Fizeau laser interferometer (Ref. 1) was constructed and mounted on a tripod (Fig. 3). By means of electronic stabilization, the system was freed of many of the environmental instabilities that commonly trouble interferometers; hence it was suitable for field use. Extremely small displacements could be detected with this instrument. If the displacement of the earth, Δ, is represented by $\delta \cos \omega_s t$, where ω_s is the angular frequency of sound, the minimum displacement, δ, detected by this system was approximately 10^{-12} m (0.001 nm), a dimension considerably smaller than an atom.

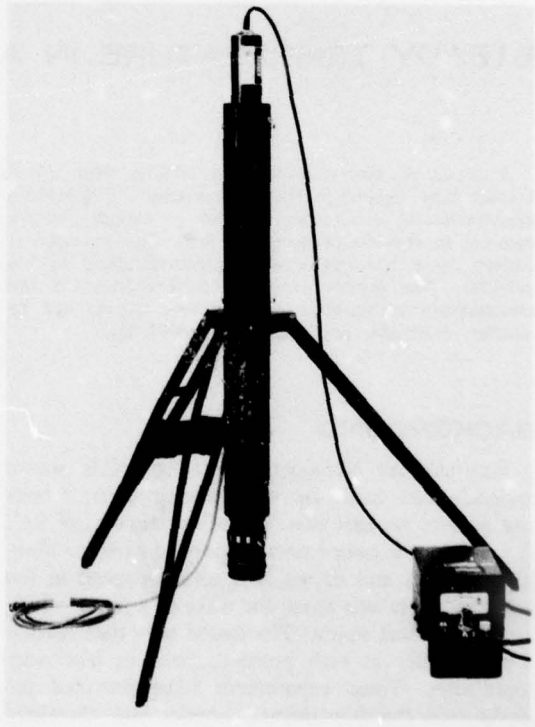

Fig. 3 Field-portable laser interferometer for detecting displacements of the earth's surface.

The detector was used to study surface or Rayleigh waves (Ref. 3) in sand and earth in the laboratory. The waves were generated by pulses from a piezoelectric driver in contact with the soil surface. The Rayleigh wave velocity in sand, V_R[8], was about 52 m/s. In earth, Rayleigh velocity ranged from 66 to 145 m/s, depending on soil compaction. The sand measurements agree with results obtained by other workers (Ref. 5).

REFERENCES

1. A. N. Jette, M. S. Morris, J. C. Murphy, and J. G. Parker, "Active Acoustic Detection of Leaks in Underground Natural Gas Distribution Lines," *Mater. Eval. (Res. Suppl.)* 35, No. 10, 1977, pp. 90–99.
2. J. G. Parker, A. N. Jette, and M. S. Morris, "Radiation Accompanying the Propagation of Acoustic Waves Within an Underground Pipe" (to be published in *J. Acoust. Soc. Am.*).
3. W. M. Ewing, W. S. Jardetsky, and F. Press, *Elastic Waves in Layered Media*, McGraw-Hill, New York, 1957.
4. G. F. Kuhn and C. L. Morfey, "Transmission of Low-Frequency Internal Sound through Pipe Walls," *J. Vib. Sound* 47, No. 2, 1976, pp. 147–161.
5. F. E. Richart, Jr., R. D. Woods, and J. R. Hall, *Vibration of Soils and Foundations*, Prentice-Hall, Englewood Cliffs, NJ, 1970.

Authors: *J. G. Parker, A. N. Jette, M. S. Morris, and J. C. Murphy*

Support: *American Gas Association*

STEADY TEMPERATURE IN A MOVING CYLINDER

A group of boundary value problems (Ref. 1) is solved that describes the steady-state temperature distribution in a circular cylinder of infinite length, moving in the direction of its axis. The cylinder is heated by a hot gas flowing perpendicularly to the cylinder. The theory supports experiments on the steady-state combustion of polymers carried out by Hunter, Fristrom, and Grunfelder (Ref. 2).

BACKGROUND

Polymers are commonly occurring solids whose molecules are made up of repeating units; fabrics and plastics are examples. In the experiments of Ref. 2, a polymer is coated on a supporting wire (or fiberglass strand) and drawn at a constant speed in the direction of its axis across the wake of a flame, which serves as a heat source. The coated wire then reaches a steady state at each position, fixed in laboratory coordinates. These experiments have provided insights into the fundamental physics and chemistry of polymer combustion. The present theory has aided in the interpretation of the data.

DISCUSSION

The chemical reactions in polymer combustion are controlled mainly by the temperature of the solid phase. First, combustion requires a mixture of flammable gas and oxygen. The flammable gas evolves from the surface as a result of chemical reactions in which the polymer breaks down into simpler species, some of which are gaseous. Which reactions take place and how fast they occur are controlled mainly by the temperature of the solid phase. In particular, the onset of the evolution of flammable gas occurs at a well-defined surface temperature that is characteristic of the composition of the polymer. The ignition delay time is simply the warm-up time required for the surface to reach the flammable gas temperature.

Reference 1 calculates the temperature of the moving polymer-coated wire in terms of experimental variables, including the wire speed and diameter, the exposure time, the thermal properties of the polymer, and the intensity of the heat source as a function of longitudinal position.

Figure 1 treats a simple case in which the polymer coating is very thin. The plot determines surface temperature, T, at a given (dimensionless) exposure time t^*, and a given (dimensionless) heat transfer coefficient, N; T_{av} is the angle-averaged temperature in the gas near the wire, and T_0 is the room temperature. The figure can be applied to the determination of the polymer's flammable gas temperature. The value of t^* at ignition is measured when T_{av} and N are known. The flammable gas temperature is then the corresponding value of T read from the chart. This would be difficult to measure directly, although it is possible in a few cases. In those cases, the agreement between theory (refined somewhat) and experiment is satisfactory.

The inverse of Fig. 1, in which exposure time is plotted against surface temperature, determines an ignition delay time when the flammable gas temperature is known. That kind of illustration has provided correlations of data obtained in different heat sources and with different wire sizes.

Currently, the results in Ref. 1 are being applied to studies of polymer combustion at low pressure. The evolving gases are sampled for chemical analysis, and the temperature of the surface where the sample is taken is then calculated from Ref. 1.

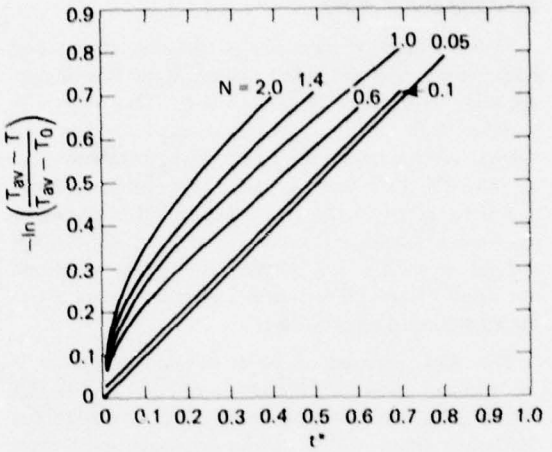

Fig. 1 Surface temperatures of a polymer-coated wire moving at constant speed in the direction of its axis through a cross flow of hot gas.

REFERENCES

1. L. W. Hunter and S. Favin, "Steady State Temperature Distribution in a Solid Cylinder Moving in the Direction of Its Axis Through a Cross-Flow of Hot Gas," *J. Heat Transfer* **99**, 1977, pp. 668–674.

2. L. W. Hunter, R. M. Fristrom, and C. Grunfelder, "Steady State Polymer Combustion," *APL Developments in Science and Technology, Fiscal Year 1976*, APL/JHU DST-4.

Authors: *L. W. Hunter and S. Favin*

Support: *National Fire Prevention and Control Administration, U.S. Department of Commerce, Grant NFPCA 76-033*

HEART AND CYANIDE STUDIES

The term "smoke inhalation" has been used to describe the cause of death of fire victims for many years. The term is imprecise since many physiological and toxicological interactions could have caused the death. The APL Fire Casualty Study was initiated in 1971 to clarify the mechanisms involved when a person dies as a result of insult to the respiratory system caused by the toxic atmosphere generated in residential fires.

Two segments of the ongoing study that have provided an insight into the fire fatality problem are the special heart and cyanide studies. The work through the middle of Calendar Year 1977 is discussed here, but the studies are continuing.

BACKGROUND

Smoke generated by a fire is complex, comprising both gaseous and particulate matter. Many constituents are toxic irritants to the human body. This view is at variance with previous general concepts, which considered carbon monoxide produced by combustion to be the only toxic part of smoke. No serious concern had been given to the possibility of other causes of the toxic atmosphere in a fire. Even now, this concept is held so solidly that hospital emergency rooms do not think of any other possible problems when treating smoke inhalation victims.

The APL program includes detailed autopsies of fire victims, including blood toxicology. The results of the initial work indicate that carbon monoxide was the lethal agent in 50% of the cases, but some other reason had to be found for the cause of death in the rest. With this fact in mind, the study effort was expanded in an attempt to determine whether preexisting heart disease or other toxic agents were involved.

One of the toxic agents considered was gaseous hydrogen cyanide. It can be produced by the combustion of nitrogen-containing materials such as wool, nylon, polyurethane, and acrylonitrile, and a special effort was made to determine if the fire victims had been exposed to it.

DISCUSSION

Heart Study

This study (Ref. 1), initiated and carried out by the Maryland State Office of the Chief Medical Examiner, explored the relationship between preexisting heart disease, blood carbon monoxide levels, and the incidence of fire mortality. Persons with preexisting heart disease might be expected to succumb to lower levels of carbon monoxide, that is, survive for a shorter period of time than healthy individuals in an atmosphere contaminated with carbon monoxide. This premise assumes that, in an individual with heart disease, the myocardial oxygen supply is in jeopardy even in a normal atmosphere.

The heart study population of the Maryland Medical Examiner's Office consisted of adult fire victims (20 years of age and older) who died during the course of a fire or within six hours thereafter. Because of the diversity of the group satisfying these criteria, comparative analysis required the group to be narrowed down to a more homogeneous population. Also in an effort to achieve some degree of uniformity regarding the terminal environment and the circumstances, only those who died as a result of a "typical" house fire were analyzed further. This excluded all victims of flash fires, automobile collision fires, etc.

The only readily measurable and quantifiable parameter of preexisting heart disease is coronary stenosis, which is the most important and widespread form of heart disease. The hearts of all victims in the study were examined. The coronary arterial tree was dissected from the heart and decalcified, and the arteries were serially sectioned throughout their lengths. The degree of luminal stenosis is expressed as the percentage of narrowing with respect to the original lumen. The arteries were divided into three segments: proximal, middle, and distal, based on the total length of each artery. The maximum stenosis for each segment of each major coronary artery was used in conjunction with the other autopsy findings to quantify the extent of heart disease in the victims.

One of the early and striking findings was that the amount of heart disease, expressed in terms of coronary artery stenosis, is higher in the fire victims than would be expected in the general population, particularly in the younger group. Of the 41 victims in the young group (20 to 39 years of age), eight had greater than 90% stenosis in at least one segment of the major coronary arteries. In addition, 40% of the overall total had at least one focus of stenosis of 90% or more, and more than half had narrowing greater than 75%.

Despite the fact that other toxic gases and substances may be generated during a fire, carbon monoxide poisoning remains the primary killer. The generally accepted minimal lethal level for carbon monoxide intoxication is 50% blood saturation. Whenever death occurs with a lower level, other contributory factors must be sought. The original analysis focused on individuals who succumbed with less than 50% blood carbon monoxide saturation.

If the presence of significant heart disease leads to a greater susceptibility to carbon monoxide poisoning, one would expect a considerable number of these victims to die with a low level of blood carbon monoxide. The relationship between blood carbon monoxide level and coronary artery stenosis was examined. No constant relationship between these two parameters was found. Of the victims with significant heart disease, a preponderance achieved a blood saturation level of greater than 50% before dying.

Why did such a substantial number not succumb to low carbon monoxide levels? It could be postulated that preexisting heart disease makes escape from the fire difficult but does not necessarily contribute to an

early death. The incapacitated group would then inhale variable amounts of carbon monoxide, accounting for the wide range of lethal levels found. This cardiac-based incapacity would also explain the high incidence of heart disease in our series since the heart disease would "select" fatalities. However, before accepting this explanation, another variable had to be considered.

Alcohol has long been known to be a factor in house fires, and various theories have been propounded regarding the interaction of carbon monoxide and alcohol as a cause of death. Blood alcohol determinations are made for all fire victims, and this parameter could readily be considered. Of the 119 victims, 92 had measurable amounts of alcohol in their blood at the time of death, including 67 of the 85 males. There is no evidence to suggest that the presence of alcohol *per se* has an effect on the level of carbon monoxide associated with death. In addition, although both are central nervous system depressants, there is no apparent additive effect.

Because the group was relatively small, only the males were sufficient in number to warrant further analysis. They were divided into "sober" and "inebriated" groups, the inebriated having a blood alcohol content of 0.15% or higher. Of the sober individuals, approximately half of those with significant heart disease died with a low level of carbon monoxide; the remainder achieved a level of greater than 50% before dying. In the inebriated group, 18 of 21 individuals with significant heart disease had a carbon monoxide level of greater than 50%. When these values are averaged for the two groups, we find that sober individuals with heart disease had a mean carbon monoxide level of 51%, while the inebriated victims had a mean level of 64%. Those without significant heart disease in both groups had similar levels, 63 and 62% in the sober and inebriated groups, respectively.

Apparently people with significant heart disease live longer in a fire when under the influence of alcohol than when sober. There are several possible explanations, the simplest being that the test group was too small for the results to be valid. Possibly alcohol so impairs judgment that the inebriated victims are unaware of the danger in the situation and do not panic, whereas some of the sober individuals die prematurely because of stress. However, if this were the case, one would expect the inebriated individuals without heart disease to have higher levels of carbon monoxide than the sober ones and this is not so. A more interesting speculation is that the inebriated individuals with heart disease survive longer because alcohol acts as a dilator of atherosclerotic coronary arteries.

Hydrogen Cyanide Study

The potential for the involvement of cyanide in fires has increased with the increasing use of polymeric materials in residences. An extensive study was undertaken by the Maryland State Office of the Chief Medical Examiner and APL to determine the possible role that cyanide might have in causing fire casualties.

An analytical method that would be accurate, repeatable, and acceptable to the toxicological community had to be defined. Suggested methodologies were evaluated (Ref. 2), and a modification of those suggested in Ref. 3 was selected. It is specific and sensitive to 0.01 μg/ml of cyanide.

The cyanide molecule is elusive in biological materials. It can be lost and it can be generated after death. The stability of cyanide in blood stored under various conditions after death was studied extensively in fire death victims and in simulated blood samples (Ref. 4). To minimize difficulties, the blood for analysis should be obtained within 24 hours after death.

A set of normal values was obtained by measuring blood cyanide levels in 32 living subjects, 64 random *nonfire* victims, and 22 airplane crash victims who died of impact injuries. The range of readings for the 118 cases was 0.00 to 0.22 μg/ml; therefore, values ranging from 0.00 to 0.25 μg/ml were considered normal.

Cyanide concentrations were determined in 256 fire fatalities that occurred in Maryland during the period 1 January 1975 to 28 June 1977 (Refs. 2 and 4). The distribution of the results of these analyses is shown in Table 1. Normal concentrations were found in 30% of the cases. Subtoxic concentrations (0.26 to 1.00 μg/ml) were found in 35% and would not be expected to elicit biological effects, although concentrations exceeding 0.26 μg/ml are indicative of the presence of cyanide precursors in building materials. Possibly toxic concentrations (1.01 to 2.00 μg/ml)

TABLE 1
DISTRIBUTION OF BLOOD CYANIDE CONCENTRATIONS IN 256 FIRE FATALITIES DURING 1 JANUARY 1975 TO 28 JUNE 1977

Cyanide Concentration (μg/ml)	Number	Percent
0.00–0.25	77	30
0.26–1.00	89	35
1.01–2.00	66	26
2.01 and greater	24	9
	256	100

were found in 26% of the cases, and probably toxic concentrations (2.01 μg/ml and greater) in 9%. These concentrations are indicative of exposure and toxicity and may result in interaction with other toxic substances and possible incapacitation.

The detection of cyanide in concentrations exceeding 0.26 μg/ml in 70% of the fire fatalities is a clear indication of the widespread distribution of nitrogen-containing polymeric materials in the average building or vehicle.

Blood cyanide concentrations correlated significantly with carbon monoxide saturation levels. When cyanide was high, carbon monoxide was high; when cyanide was low, carbon monoxide was low. Apparently, cyanide did not explain deaths not otherwise explained. However, its role as an intermediary agent (causing incapacitation and subjecting a victim to a prolonged exposure to carbon monoxide) has not been fully elucidated.

An automobile fire fatality was studied in which the vehicle contained a padded dashboard and plastic-covered seats filled with urethane foam. The blood cyanide concentration was 3.13 μg/ml, and the blood was 18% saturated with carbon monoxide. The blood alcohol concentration was 0.22% and the blood methadone was 0.03 μg/ml; these factors were contributory to the accident. Limited chest and bone injuries and the carbon monoxide were insufficient to cause death, but the cyanide concentration was toxic and hence was the primary cause. The study of future cases will probably reveal similar situations that point clearly to the toxic role of cyanide. A similar case was recently observed in Virginia; the saturation level of blood carbon monoxide was 6% and the cyanide concentration was 3.1 μg/ml. The fire was of the smoldering type and no other factors were evident.

REFERENCES

1. A. M. Dixon and R. S. Fisher, *Fire Fatality Study: Heart Study*, APL/JHU FPP TR33, July 1977.
2. R. E. Altman, *The Microdetermination of Cyanide in Fire Fatalities*, Ph.D Dissertation, University of Maryland, 1976.
3. G. C. Valentour, V. Aggarwal, and I. Sunshine, *Anal. Chem.* 46, 1974, pp. 924–925.
4. Y. H. Caplan, *Relationship of Cyanide to Deaths Caused by Fire*, APL/JHU FPP TR31, June 1977.

Authors: ***Y. Caplan, A. Dixon, and R. Fisher (Chief Medical Examiner's Office, State of Maryland), and B. Halpin (APL)***

Support: ***National Bureau of Standards Grant***

OCEAN SCIENCE AND TECHNOLOGY

INTRODUCTION

An understanding of the physics of the ocean environment is essential to APL in performing its mission in support of the Fleet. This area of physics includes propagation of electromagnetic and acoustic radiation; absorption and scattering both within and at the surface of the ocean; hydrodynamic phenomena such as surface waves, internal waves, and currents; and the effects of physical variables such as water temperature, pressure, salinity, and density on ocean dynamic phenomena. Central to APL's effort is the development of sensing and data-processing systems to detect and characterize signals propagated through or at the surface of the ocean. While analysis, simulation, and laboratory research are extremely useful, many phenomena of interest must be studied at sea. Accordingly, APL has developed the capability to conduct large-scale scientific studies in the open ocean.

Much of the ocean research is not reported here for reasons of national security, but a small sample has been selected to illustrate different areas of interest. Theoretical studies are exemplified by a mathematical analysis of the transient effects produced by the impulsive injection of fluid into a medium having a vertical density gradient, such as the ocean. The Navigation Information and Computing System, described in the next article, provides, for the first time, an automatic recording of ship position reference data and a real-time readout of ship position. As oceanographic research becomes more sophisticated, greater precision and accuracy are required in determining ship position.

Also reported are the first successful measurements of the earth's gravitational field from a fixed-wing aircraft. The final two articles describe work related to SEASAT–A, a NASA-sponsored satellite and the first dedicated to oceanographic research. One article describes a wideband data link for the transmission of synthetic aperture radar signals to the ground. The other reports the development of a device to simulate the radar return signal for the radar altimeter aboard SEASAT–A. The simulator was used to test the altimeter's capability to measure ocean wave height and satellite altitude.

Although APL's increasing expertise in ocean physics to date has been applied to Navy problems, it should be available in the future to enhance the specific understanding of the ocean environment and to assist in its peaceful exploitation. Site surveys for determining optimum locations for ocean thermal energy plant-ships is one example of many possible applications.

SINGULAR SOLUTIONS IN BUOYANT FLOWS

The fundamental solution for a system of equations that describes a model of buoyant flow represents an impulsive injection of fluid at a point. Examination of the velocity and displacement fields associated with this solution suggests that transient effects in general are likely to remain strongly localized near the region where they are generated and to last a long time.

BACKGROUND

In the flow of a fluid of variable density, such as the ocean, buoyant effects induced by gravity acting on the fluid can play a significant role. Among these effects are the well known slug flows at very low velocities, the pronounced oscillatory flows induced near the buoyancy frequency, and the steady-state flows caused by bodies moving at constant velocity.

Recently we have been able to find the fundamental solution for a system of equations that describes the transient flow of such a fluid in three dimensions. Our study (Ref. 1) of the fundamental solution, which corresponds physically to an impulsive injection of a unit mass of fluid at a point, graphically illustrates the fact that in this model of fluid behavior the transient motion remains largely localized in the vicinity of the original disturbance, does not propagate away, and lasts a long time.

This suggests that it would be unwise to use steady-state results for fluids that might be modeled similarly if transient effects are likely to be at all significant, even though in the real world the amplitudes would eventually dissipate because of viscous and nonlinear effects.

DISCUSSION

The usual conservation laws for an inviscid incompressible fluid with an initial stable unperturbed density, ρ_0, that depends only on the vertical coordinate, x_3, yield, when linearized about the static solution, a system of equations given by

$$\frac{\partial^2 w}{\partial t^2} + n^2 w + \frac{n^2}{\rho_0}\frac{\partial \varphi}{\partial x_3} = 0$$

and

$$\frac{\partial^2 \varphi}{\partial x_1^2} + \frac{\partial^2 \varphi}{\partial x_2^2} + \rho_0 \frac{\partial}{\partial x_3}\frac{1}{\rho_0}\frac{\partial \varphi}{\partial x_3} + \rho_0 \frac{\partial w}{\partial x_3} = 0 \quad ,$$

to be satisfied at every point away from regions where there are sources or body forces other than gravity. The quantity n^2 stands for $-(g/\rho_0)d\rho_0/dx_3$. The velocities, which are the most important quantities associated with a solution of these equations, are given for the horizontal components, u_1 and u_2, by

$$u_\alpha = \frac{1}{\rho_0}\frac{\partial \varphi}{\partial x_\alpha}, \qquad \alpha = 1, 2$$

and for the vertical component by

$$u_3 = w + \frac{1}{\rho_0}\frac{\partial \varphi}{\partial x_3} \quad .$$

When n and ρ_0 are treated as constants in these equations (a frequently made approximation), the fundamental solution discussed in Ref. 2 can be obtained explicitly. Analytical details of the solution are given in Refs. 2 and 3. Here we note that the velocities are purely radial into and out from the disturbance, and that they can be integrated exactly to obtain the radial displacement field.

The impulsive source for which we show velocity and displacement graphs emits a unit sphere of fluid at $t = 0$. Initially the fluid is pushed out radially to accommodate the injected fluid. The subsequent flow develops slowly. Above and below the disturbance the fluid velocity is vertical and oscillates sinusoidally at the buoyancy frequency. Horizontally, the fluid velocity is steadily outward from the origin and tends in time to the value $1/(3r^2)$, where r is the horizontal distance from the origin.

The first series of graphs (Fig. 1) shows the velocity field development. The flow is axially symmetric about the vertical axis and symmetric with respect to the horizontal plane through the origin; hence one quadrant suffices to show everything. Since the velocities are radial, they are plotted radially; the scale is such that the maximum velocity above the origin is of magnitude one. For visual reference, the 0 and ± 5 values of the velocities are shown.

The six graphs of Fig. 1 show the development of the velocity field at quarter-period intervals through the first one and one-half buoyancy periods. Its further development is shown at each period from the second through the tenth in Fig. 2. Significant in these graphs are the steady oscillation at the buoyancy frequency above the disturbance, the develop-

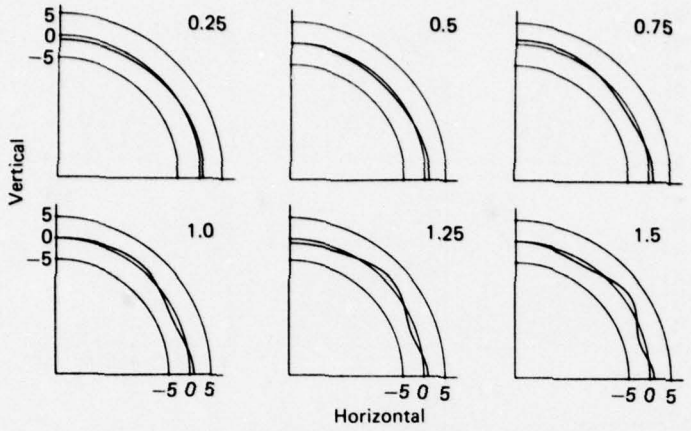

Fig. 1 Impulse source velocities at quarter-period intervals from 0.25 to 1.5 periods.

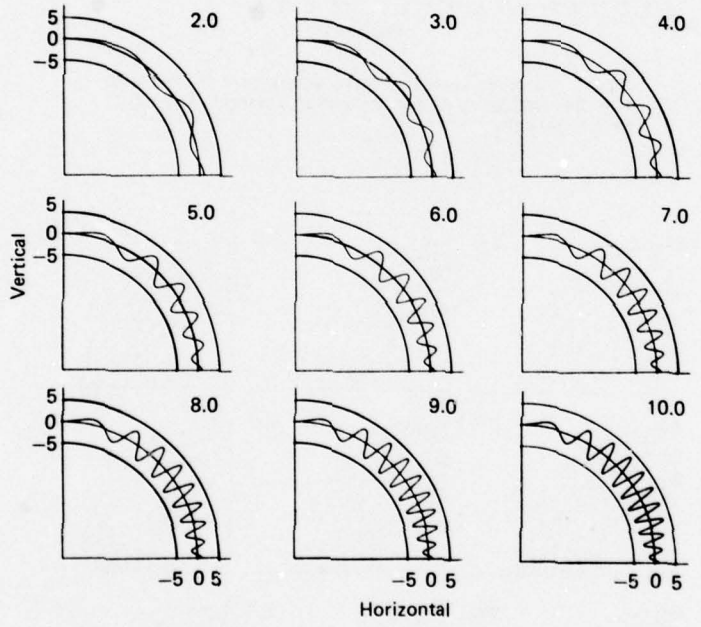

Fig. 2 Impulse source velocities at one-period intervals from 2 to 10 periods.

ment of convolutions or waves in the velocity as time passes, and the rapid approach to a steady outward flow in the horizontal plane. It is also evident that the vertical oscillations above and below the source propagate toward the horizontal plane to give a convoluted and wavy velocity field as time passes.

The next series of graphs shows the displacements that result from the same impulsive source. Figure 3 shows what happens to spherical shells at quarter-period intervals to one and one-half periods. The shells are originally at the positions shown in the first graph of Fig. 3. The second graph of Fig. 3 shows the radial displacements of these shells immediately following the impulse. Figure 4 shows the subsequent development of the displacements at each period through the tenth. The displacements, like

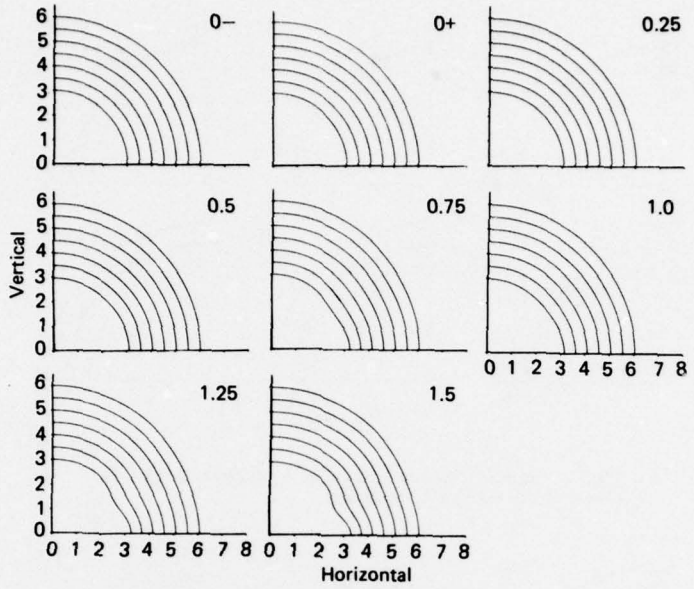

Fig. 3 Impulse source displacements at $t = 0-$ and $t = 0+$ and then at quarter-period intervals from 0.25 to 1.5 periods.

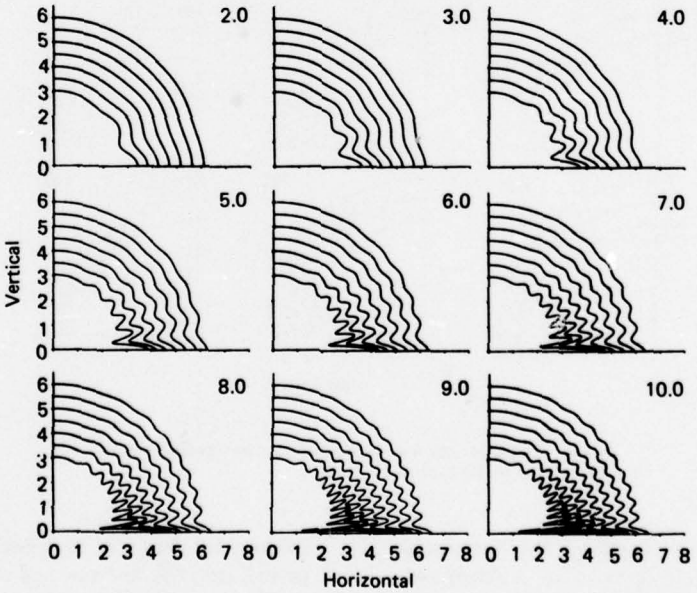

Fig. 4 Impulse source displacements at one-period intervals from 2 to 10 periods.

the velocities, also oscillate steadily above the source, become convoluted with waves that move toward the horizontal, grow steadily outward in the horizontal plane, but do not propagate away from the source.

REFERENCES

1. D. W. Fox and V. G. Sigillito, "Singular Solutions in Buoyant Flows, Part I" (to be published in *Z. Angew. Math. Phys.*).
2. D. W. Fox, "Transient Solutions for Stratified Flows," *J. Res. Nat. Bur. Stand.* **80B**, 1976, pp. 79–88.
3. D. W. Fox and V. G. Sigillito, "Singular Solutions in Buoyant Flows, Part II" (to be published in *J. Angew. Math. Phys.*).

Authors: *D. W. Fox and V. G. Sigillito*

Support: *Indirectly Funded R&D*

NAVIGATION INFORMATION AND COMPUTING SYSTEM

The Navigation Information and Computing System (NICS) was developed to provide a real-time display and a permanent record of a submarine's position as well as to predict the submarine's location at the time of missile launch. NICS can perform these functions using one or several position measurement systems, selecting or combining the outputs of each system as directed by the operator.

BACKGROUND

Evaluation of the performance of submarine navigation systems requires accurate measurement of the submarine's position while at sea. Recent advances in digital electronics and signal processing, and an increasing demand for the precise determination of ship position for such purposes as offshore oil exploration, have contributed to the development and marketing of several new position reference systems. To determine the suitability of these systems for the evaluation of navigation systems, the Navy's Strategic Systems Projects Office requested APL in 1975 to conduct a field demonstration, comparison, and performance evaluation of several position reference systems (Refs. 1 and 2). A special-purpose interface device was designed and built by APL to provide time coordination and simultaneous data recording for as many as six systems (Fig. 1). The reliable performance and convenient operation of the interface and control unit (IFCU) motivated further development and the subsequent production of two NICS units.

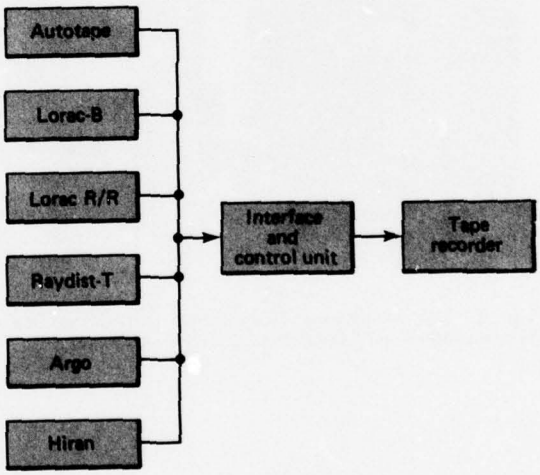

Fig. 1 Interface and control unit configuration for demonstration of position reference. Six position reference systems were interfaced to the tape recorder by the predecessor of the NICS.

DISCUSSION

NICS (Fig. 2) comprises several commercially available hardware components as well as the specially designed IFCU (Ref. 3). Included are a Hewlett-Packard 9825 programmable calculator with thermal printer and X–Y plotter peripherals, a cartridge-type tape recorder, and a graphics unit with

a cathode ray tube (CRT) display. The IFCU functions as the interface between the several position reference systems and the calculating, displaying, and recording equipment (see Fig. 3). It also contains the system clock and an intervalometer, which controls the transfer of data to the tape recorder.

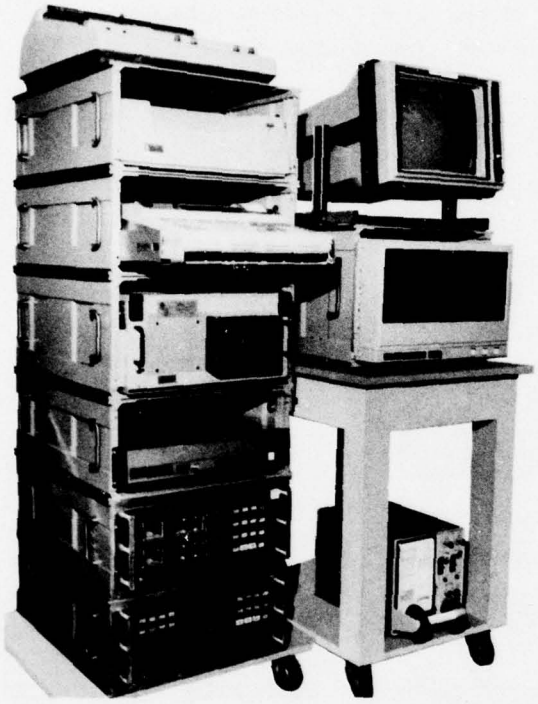

Fig. 2 The Navigation Information and Computing System, shown with Lorac hyperbolic equipment.

The data-recording function of NICS is independent of calculator operation. Once each second, the output of each position measurement system is sampled and stored in a buffer. When the buffer has been filled, the calculator input/output status is checked. If the calculator is ready to accept data, the contents of the buffer are transferred to the IFCU data bus under calculator control. If the calculator is not ready for input or is not present, its control lines are disabled and a built-in counter transfers the buffer contents to the IFCU bus. If the intervalometer has counted down to zero, a buffer for the tape recorder is enabled and accepts the data on the IFCU bus for subsequent transfer to the tape recorder.

Data are transferred from the calculator to the thermal printer and the X–Y plotter via the manufacturer's interface. APL devised a means of displaying and plotting processed data on the CRT using the Megatek BP–741 graphics display interface.

The primary application of NICS (Ref. 4) is in Polaris and Poseidon submarine Demonstration and Shakedown Operations conducted near Cape Canaveral, Florida. The position reference system currently used is Lorac Hyperbolic. Lorac data in the form of Red Lane count and Green Lane count are transferred to the calculator every 30 seconds. These data are converted to latitude and longitude by the calculator and are output to the printer.

The CRT displays, located in the submarine navigation center and in the control room, show a representation of the nearby Florida coast, operating area boundaries, and the submarine's position. The calculator differentiates the calculated position and maintains an estimate of speed over ground and course. This velocity estimate is then used to calcu-

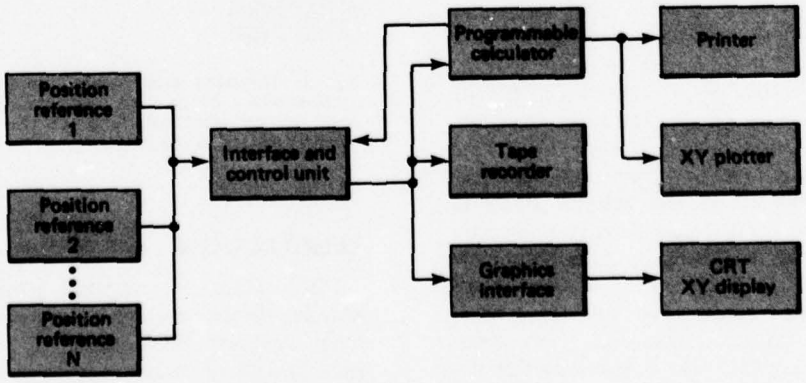

Fig. 3 Block diagram of the Navigation Information and Computing System.

late the effects of ocean current on ship movement and to predict the coordinates of the submarine position at the time of missile launch. Lorac lane count and time are recorded on magnetic tape and are converted to geodetic position for post-mission evaluation of the navigation systems.

REFERENCES

1. W. J. Peters, L. G. Parsons, and A. K. Halso, *DASO Position Reference Demonstration Test Plan*, APL/JHU POR-1810, May 1975.
2. A. K. Halso, L. G. Parsons, D. A. Brown, and W. J. Peters, *PREDEM Test Results*, APL/JHU POR-2040, December 1975.
3. G. E. Baer, C. R. Edwards, and A. J. Grillo, *Technical Manual for the Navigation Information and Computing System Interface and Control Unit*, APL/JHU S4S-1-174, July 1977.
4. M. C. Houbolt, *Navigation Information and Computing System Operators' Manual* (to be published).

Author: ***J. E. Boyd***

Support: ***Strategic Systems Projects Office***

AIRBORNE GRAVITY MEASUREMENTS

Gravity measurements made during Project Magnet flight tests proved the feasibility of airborne gravity surveys. Direct data processing provided gravity profiles accurate to five parts per million.

BACKGROUND

In November 1972, APL was funded to study the feasibility of using the Project Magnet airplane to conduct gravity surveys. The APL Gravity Study (Ref. 1) concluded that data from precision navigation and altimetry instruments would be needed to process data from a gravity meter. A precision navigation system was installed in the aircraft in 1974. Precision altimetry instruments and a gravity meter were installed in 1976. During a test flight on 1 November 1976, collected data proved that precision gravity measurements could be made from a fixed wing aircraft (Ref. 2).

DISCUSSION

GRAVITY MEASUREMENTS. The APL Gravity Study concluded that airborne gravity surveys could provide accuracies better than ten parts per million. The cgs unit of acceleration, the gal, is 1 cm/s^2. The acceleration of the earth's gravity is approximately 980 gal. This value varies by ±5 gal over the surface of the earth. Thus, a gravity survey accurate to ten parts per million means that the processed data are accurate to ±10 mgal.

The LaCoste and Romberg gravity meter measures the force required to balance a mass against the force of gravity. Two levels of force are established: a constant force of approximately 980 gal to cancel the bulk of the earth's gravity force, and a dynamic force to balance variations in the ambient gravity field. In an airborne survey, motions of the airplane cause variations in the force required to balance the mass.

The final product of a gravity survey is an area map depicting the gravity anomaly. The anomaly is the difference between measured and computed gravity values. The computed values are derived from a mathematical model of the earth's gravity field. In order to make an accurate comparison between the two gravity values, the exact position of the airplane must be known. For instance, in an area where the gravity changes 10 mgal/mi, a navigation error of 1 mi could cause a 10-mgal error.

Gravity surveys are conducted at constant altitude; an airplane flying at constant altitude over the surface of the rotating earth experiences centrifugal accelerations. The acceleration due to an east or west velocity component is approximately 7 mgal/kt.

The altitude of the airplane affects the gravity data in two ways. At survey altitudes, the acceleration of gravity decreases approximately 1 mgal for each 10 ft of altitude. Also, vertical motions of the airplane cause forces on the mass in the gravity meter, but the gravity meter cannot detect the difference between the force due to gravity and the forces due to airplane motion.

NAVIGATION SYSTEM. The Honeywell electrically suspended gyro (ESG) navigation system enables the Magnet airplane to navigate surveys with the accuracy required for gravity measurements. The accuracy of the ESG is specified to be 0.1 nmi/h. This means that the ESG navigation data will be accurate to within 1 nmi during a 10-h survey.

A conventional "local vertical" system attempts to maintain a level platform in order to align the horizontal accelerometers on the platform perpendicular to the force of gravity. Thus, the vertical accelerometer is aligned parallel with the local force of gravity. The gyros must be torqued constantly to track the local vertical.

The ESG is a space-stable inertial system. It is aligned initially in the local vertical mode. However, once aligned, the gyros are left to spin in the initial alignment. Thus, the accelerometers on the ESG platform measure the accelerations of the airplane in space-stable coordinates. A computer transforms the ESG gyro data to values computed for local vertical coordinates. The absence of perturbing torques reduces system errors by a factor of ten or better.

ALTIMETRY SYSTEMS. The Honeywell precision radar altimeter enables the Magnet system to determine the altitude of the airplane over water. This instrument provides altitude data that are accurate to 10 ft. In operation, a burst of radar pulses is transmitted by the altimeter, which then pauses to monitor the returning signals. When "locked on," the radar circuits detect and track the first signals returning from each radar burst. Timing circuitry computes the transit time between transmission and return, and this transit time is used to determine the altitude of the airplane.

The Rosemount pressure port calibrator compares the atmospheric pressure with a reference pressure. At survey altitude, a test valve is opened to fill a reference chamber at ambient pressure and is then closed to trap the reference pressure in the chamber. During a survey, changes of less than 1 ft in altitude can be detected.

GRAVITY SURVEY. On 2 November 1976, a gravity survey was conducted at 16 000 ft to escape unusual turbulence at lower altitudes. The airspeed was approximately 250 kt. The gravity data were recorded on magnetic tape by the LaCoste and Romberg Air-Sea Gravity System, and the navigation data were recorded on magnetic tape by the Magnet system.

The results of the gravity survey were analyzed, and gravity measurements accurate to 5 mgal were determined. Computations were made from data samples taken at 10-s intervals. Figure 1 (from Ref. 1) shows plots of the gravity anomaly for one track of the survey. This track was flown in an area for which the gravity anomaly is well known. One curve shows the gravity profile observed during a shipboard survey of the area. The second curve shows the profile extrapolated to depict the profile computed for an altitude of 16 000 ft. The third curve shows the profile obtained after subjecting the extrapolated data to a low-pass filter. This curve was used to evaluate the results of the Project Magnet gravity survey.

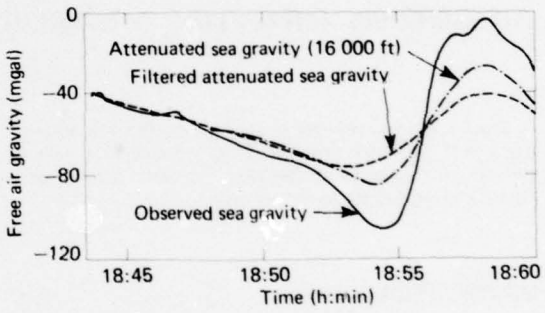

Fig. 1 Effect of attenuation and filtering on a gravity profile.

Figure 2 (from Ref. 2) shows a comparison of the observed air gravity profile with the reference profile. Dr. LaCoste made the following comments on this figure:

"The filtered attenuated sea gravity profile is the smoother of the two curves. However the observed air profile follows it closely. Since we have made no arbitrary systematic corrections to the observed air profile, its negligible average offset from the sea profile is significant. It indicates good performance of all the system components over the longer periods. The rest of the air gravity results for which we have comparison sea gravity are about the same as shown in [this figure]. Unfortunately, we do not yet have comparison sea gravity for about two-thirds of the data we have processed. Such data will be available

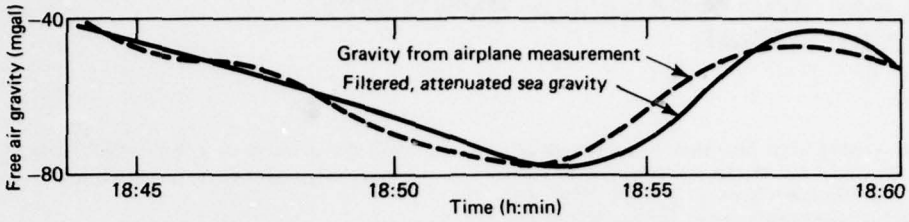

Fig. 2 Comparison of the gravity obtained by air with the gravity obtained at sea using the same filtering.

shortly. For the air gravity for which we have comparison data, the noise or roughness in the air gravity amounts to only about 4 or 5 milligals, which is as good as I had hoped for when I began analysing the data. Obviously the roughness can be reduced by more filtering but only with loss of detail."

Figure 3 compares readings from the gravity meter with data from three altitude sensors in the Magnet airplane. The pressure port calibrator gives the best correlation.

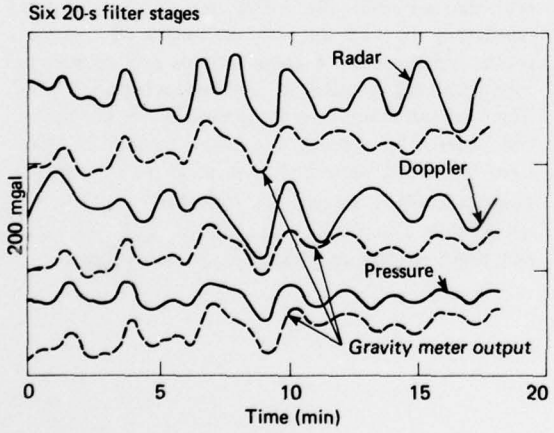

Fig. 3 Comparison of gravity meter readings with accelerations obtained from three types of measurement.

CONCLUSION

The Project Magnet gravity tests demonstrated the feasibility of airborne gravity surveys. Direct data processing provided gravity profiles accurate to 5 mgal. Estimates of system errors could be used to enhance these results.

The accuracy of the navigation data could be improved by applying Kalman filtering, which combines independent navigation measurements to provide a statistical estimate of system errors. Gravity surveys accurate to 1 mgal may be possible with this technique.

REFERENCES

1. J. A. Ford and L. J. Levy, *Gravity Study for Project Magnet*, APL/JHU S3-R-018, August 1973.
2. L. LaCoste, J. A. Ford, R. Bowles, and K. Archer, "Gravity Measurements in an Airplane Using State of the Art Inertial Navigation," presented at the 1977 meeting of the Society of Exploration Geophysicists, Calgary, Canada.

Authors: *J. A. Ford and L. J. Levy*

Support: *NAVOCEANO*

DATA LINK FOR SEASAT–A SYNTHETIC APERTURE RADAR

A wideband analog data link that has been developed by APL for NASA allows the transmission of both radar-return and timing-reference signals from the SEASAT–A synthetic aperture radar (SAR). Significant features of the data link include the realization of a linear (versus frequency) 20–MHz analog channel and the transfer of time from the spacecraft with a precision of better than 1 ns.

BACKGROUND

The SEASAT–A spacecraft will contain an experimental SAR developed by the Jet Propulsion Laboratory of the California Institute of Technology. The SAR will provide all-weather imaging of both land and sea surfaces with a resolution of 25 m. As originally conceived, the wideband radar-return signal was to be digitized at the spacecraft and the data were to be transmitted using one or more standard NASA S–band telemetry channels. However, a short study by APL revealed that, for full resolution imagery, the on-board digitizing approach consumed more transmission bandwidth than was readily available. As an alternative, APL proposed an analog data link that uses simple frequency translation of the L–band echo to S band, thereby minimizing the RF allocation problem.

In September 1975, the SEASAT project office directed APL to commence development of the data link. During the past year, the work was completed with the delivery of a flight electronics unit and three ground demodulators for satellite integration.

DISCUSSION

The SAR data link (Fig. 1) consists of a space segment and a ground segment. Inputs to the modulator/transmitter on the spacecraft consist of the radar echo obtained from the SAR receiver, the radar pulse-repetition-frequency (PRF) timing signal, and a sample of the radar oscillator signal called the STALO. Within the modulator/transmitter, the STALO signal is used to generate a coherent beacon signal centered in the middle of the radar return spectrum. It also generates the conversion frequency required to translate the L–band (1275 MHz) radar output to S band (2265 MHz).

The beacon signal is phase-modulated by a 4096–bit pseudorandom noise (PRN) binary code that is synchronized with the radar PRF input; the code subdivides the PRF interval, nominally 600 μs, into precise subintervals of about 160 ns and enables recovery on the ground to the subnanosecond level. The modulated signal is RF-summed with the beacon and radar echo signals, and the composite is translated to S band, amplified in a linear 5–W amplifier, and transmitted through a right-hand circular antenna with (nominally) 2.5 dB of gain. The data link flight electronics package is shown in Fig. 2.

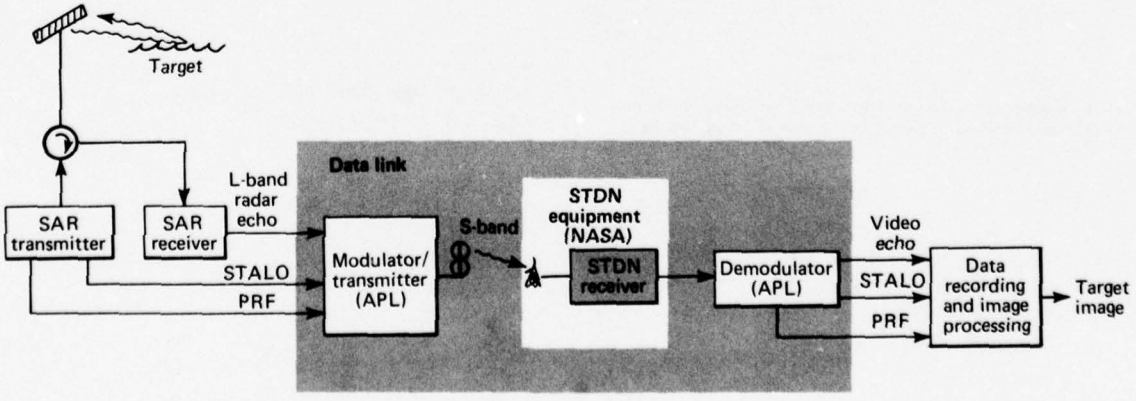

Fig. 1 SEASAT–A SAR data link.

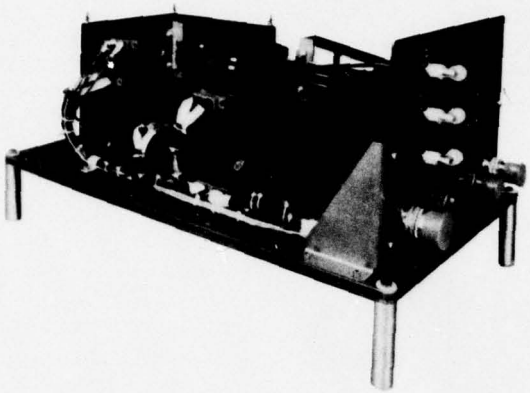

Fig. 2 Data link flight electronics (without cover).

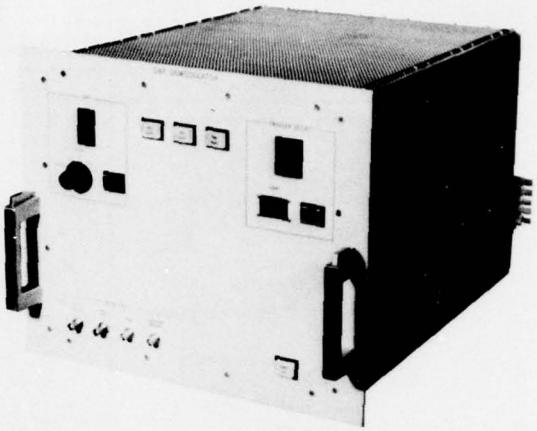

Fig. 3 Data link demodulator.

The ground segment of the data link comprises receiving equipment that is already available in the NASA Spacecraft Tracking and Data Network (STDN) stations and a demodulator unit unique to the SAR, developed as part of the data link by APL. The composite SEASAT signal is received by the STDN 30-ft dish antenna and then input to the receiving equipment. The STDN receiver phase locks to the data link beacon component and thereby removes both the amplitude and phase variations caused by the downlink slant-range dynamics. The output of the STDN receiver consists of the composite signal centered at 110 MHz and normalized in amplitude; the only amplitude variations left on this signal are due to target cross section and the geometry of the target link.

The function of the SAR demodulator unit is to decompose the composite signal from the STDN receiver and essentially regenerate the original input signals to drive the ground-based recording equipment. The PRF and STALO signals are recovered by a delay-locked loop that performs a real-time correlation between the received data link PRN code and a stored replica, producing a PRF output signal that matches the input. The delay-locked loop also recovers the STALO signal by using a special reference-signal input from the STDN receiver. This signal contains the real-time downlink doppler frequency required to preserve signal coherency.

The radar echo component is recovered by mixing the receiver output with a reference signal that has also been doppler-corrected to preserve coherency. The video-echo output is centered at 11.4 MHz and is equal in amplitude to the input level at the spacecraft. The demodulator hardware is shown in Fig. 3.

Because of its analog nature, the data link can be thought of as an extension of the SAR on-board receiver. The perfect data link would provide a unity transfer function (i.e., what comes out is identical to what goes in); the practical data link will exhibit errors due to such effects as bandwidth limitations, electronic nonlinearities, system noise, and oscillator instabilities. Specifications for the allowable data link errors were developed early in the program and can be grouped into two categories: those relating to the transfer function, which are measured by comparing the video output signal with the L-band input, and those relating to the recovery of the timing signals. The latter can be verified by comparing the input PRF and STALO signals with the recovered versions in the presence of a simulated radar return signal, which is the predominant source of timing jitter.

Table 1 compares the measured performance of the data link flight unit, the STDN receiver, and the SAR demodulator connected as an end-to-end system. Design specifications are also indicated. During these tests, the antennas were replaced by a hard-wired connection.

The first six entries in Table 1 show the performance of the transfer function. The gain variation occurs over a temperature range of -10 to $+40°C$, a much greater range than will occur in orbit. Over the more limited temperature range, the gain is well within ± 0.5 dB. Normally, a linear system driven beyond its linear range will exhibit a reduction in gain. This is not the case with the data link because the nonlinearity of the S-band power amplifier causes suppression of the data link beacon signal in the

TABLE 1

PERFORMANCE MEASUREMENTS OF SAR DATA LINK

Specification	Requirements	Measurements
Gain at center frequency	0 ± 0.5 dB	-0.5 to $+1.3$ dB
Output noise at $T = 88$ K	≤ -17 dBm	< -15 dBm at $T = 420$ K
Intermodualtion (two input tones at -3 dBm each)	≤ -20 dBc	< -25 dBc
Input level for 1 dB output expansion	$\geq +3$ dBm	$> +3$ dBm
Amplitude versus frequency ± 9.5 MHz	≤ 2 dB peak quadratic error	< 0.8 dB
Phase versus frequency ± 9.5 MHz	$\leq 26°$ peak cubic error	$< 10°$
Phase jitter of offset video at input of 0 dBm	$\leq 10°$ rms for $T = 5$ ms	$< 7°$
Timing jitter of PRF at input of 0 dBm	≤ 1 ns for $T = 2$ s	< 0.8 ns at 0 dBm $= 1$ ns at $+4$ dBm 0.7 ns for time gate on at all input levels

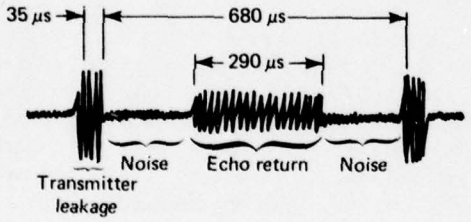

Fig. 4 Simulated SAR return signal.

presence of a larger radar echo; the STDN receiver reacts by increasing its gain to overcome the suppression, but the gain increment is also applied to the radar echo and leads to the expansion effect shown in the table.

To evaluate the phase and time-recovery performance, a SAR return simulator was used. It makes use of a white noise source, an active chirp generator, and RF-gating circuits to generate a repetitive pulsed-RF signal (Fig. 4). This signal is a fairly good approximation of the input to the data link in actual operation. As the table shows, the PRF time-recovery jitter exceeds 1 ns for input echo levels greater than $+4$ dBm; however, the demodulator has a special gating feature that eliminates the leakage and echo energy from the delay-locked loop and makes the time jitter independent of the radar echo level.

Author: *E. F. Prozeller*

Support: *NASA*

SIMULATION OF A RADAR ALTIMETER OCEAN-RETURN SIGNAL

Under the sponsorship of the National Aeronautics and Space Administration, APL has designed and developed a return signal simulator (RSS). It generates a signal with the expected characteristics of the ocean return for the SEASAT–A radar altimeter transmit waveform. With this equipment (Fig. 1), a means is provided for testing and calibrating the altimeter over the entire range of its specified performance capabilities.

BACKGROUND

The SEASAT–A radar altimeter is designed to measure the distance between the satellite and the ocean surface along the nadir-pointing axis. For this purpose, transmitted microwave pulses are modulated with a linear FM waveform. The processing of the ocean-surface reflections of these pulses yields precision altitude data and provides a sensitive measure of the surface roughness or "sea state."

To appreciate the implementation of the return-signal simulator, a basic understanding of the nature of the return signal from the ocean and the processing performed by the altimeter on this signal is required. The altimeter's function is to measure the time between the transmission of a pulse and its received reflection. The region of linear rise of the return signal (the leading edge) defines its time of arrival. The altimeter uses a linear FM transmit waveform and full deramp processing of the return signal. Figure 2 depicts the full deramp process.

The altimeter transmits a 3.2–μs pulse that has a linear 320–MHz excursion centered at 13.5 GHz. Reflections from the ocean surface over a wide range arrive at the altimeter as a packet of time-dispersed replicas of the transmit pulse. The altimeter generates a local oscillator (LO) pulse that is timed to match the arrival of the return signal. The characteristics of the LO are identical to those of the transmit pulse except that they are offset in frequency by an amount equal to the intermediate frequency of the altimeter receiver. Mixing of the LO pulse with the return signal results in a translation of the arrival of the return signal from the time to the frequency domain (Fig. 2). A spectral analysis of the mixer output and averaging of a sufficient number of reflected signals develop the average return. The power level of a spectral line indicates the surface area illuminated at a given range or time delay.

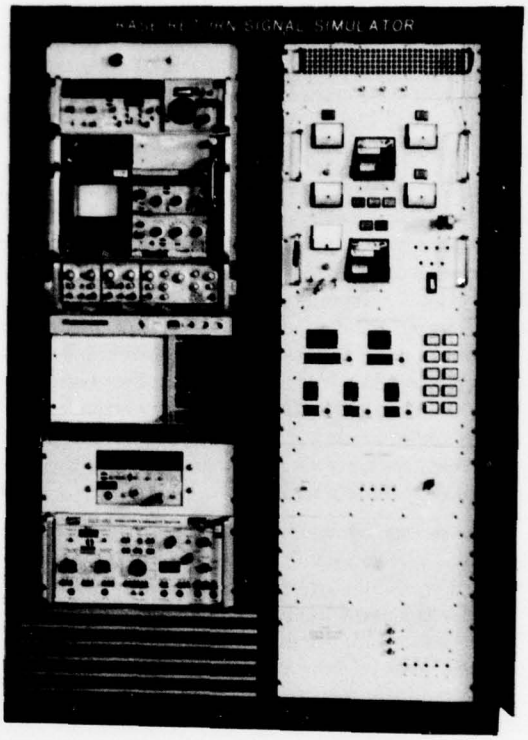

Fig. 1 The return signal simulator.

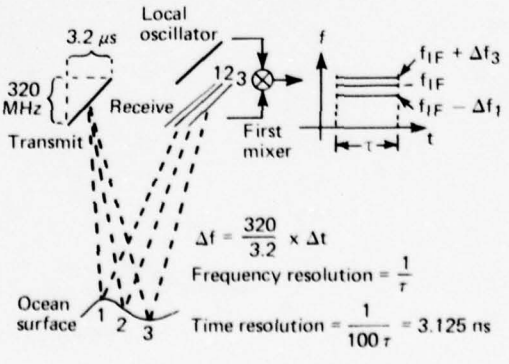

Fig. 2 Full deramp processing.

DISCUSSION

Instead of a packet of time-dispersed replicas of the transmit waveform (as is characteristic of the ocean reflections of the altimeter transmit signal), the return signal synthesized by the RSS is a packet of frequency-dispersed pulses that are generated simultaneously. Because of the equivalence of frequency and time dispersion with the altimeter's full deramp processing technique, there is no essential difference between the two types of representation.

The development of a composite return signal starts with the simulation of the average spectrum for the sea state condition. This is the reverse of the altimeter process, which develops the average spectrum from a composite ocean return. For each simulated return, the RSS adds independent phase and amiplitude noise to the spectral components to simulate the random character of the distribution of ocean wave heights. The resulting spectrum modulates a single linear FM pulse to produce the packet of frequency-dispersed pulses that is received and processed by the altimeter.

The average spectrum used to generate the return signal is derived from a mathematical model developed by Miller and Brown (Ref. 1). The model provides the normalized average power of the return signal versus time or frequency, when the effective transmit pulse width, the rms sea state, the altimeter antenna beamwidth, and the nominal altitude are known.

Synchronization of the altimeter with RSS timing is accomplished by closed-loop control of an 80–MHz voltage controlled oscillator in the RSS. The RSS receives the altimeter's linear FM transmit pulse and mixes it with an internally generated LO pulse with the same characteristics but offset in frequency. A frequency discriminator centered at the offset frequency detects misalignment between the two pulses and adjusts the RSS oscillator to null the error.

The RSS is a major component of a complement of equipment used for testing and evaluating the SEASAT–A radar altimeter. This test system is called the Radar Altimeter System Evaluator (RASE). It provides complete, automatic, computer-based testing and control of the altimeter. Options for partial or complete manual operation of the altimeter are also provided. Reference 2 gives a detailed description of the facility.

The RSS operation can be controlled and monitored by the RASE computer or by an operator at the front panel. Control consists of establishing the parameters that determine the sea state to be simulated, setting the altitude, including rate or acceleration, and adjusting the return signal power level. Once these basic parameters have been entered, the RSS generates the appropriate return signal, properly timed, solely in response to the altimeter transmissions.

In addition to the hardware that generates the return signal, a complement of commercial test equipment is included with the RSS. This provides a means of verifying the RSS operation and measuring the characteristics of the altimeter transmissions. Test points for these purposes are provided on the front panel of the RSS.

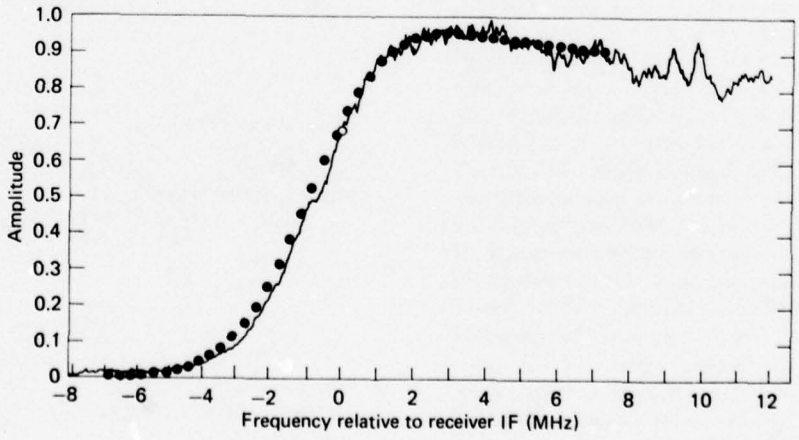

Fig. 3 Return signal spectrum.

Also for test purposes, a portion of the return signal is diverted to the receiver section of the RSS where full deramp processing takes place. Here the linear FM carrier signal is used for the LO. Spectrum analysis and averaging of the receiver IF output allow verification of the desired characteristics of the return signal.

Figure 3 is a plot of the average spectrum observed at the RSS receiver IF output for the ocean return simulation. Expected values determined from the mathematical model of Ref. 1 are presented on the plot for comparison.

REFERENCES

1. L. S. Miller and G. S. Brown, *Engineering Studies Related to the GEOS-C Radar Altimeter*, NASA CR-137462, May 1974.
2. *Radar Altimeter System Evaluator (RASE) Description*, APL/JHU SDO-4841, July 1977.

Authors: *P. C. Marth, K. H. Sanders, and E. E. Westerfield*

Support: *NASA, Wallops Island*

ENERGY RESEARCH AND DEVELOPMENT

INTRODUCTION

The development of energy systems and the assessment of the environmental impact of energy facilities have become significant program areas for APL. Work on these important civil challenges is increasing.

APL began studying the environmental impact of energy facilities in 1971 in collaboration with The Johns Hopkins University Department of Geography and Environmental Engineering and the Chesapeake Bay Institute. Since then, APL has had the responsibility to evaluate for the State of Maryland the potential environmental and social impact of all power-generating facilities proposed for development in the State. This work has led to projects and contributions in a wide variety of technical areas related to the impact of energy facilities, impact mitigation, and facility location.

One such project involves the prediction of probable locations for future power plants within a multistate region under various scenarios for the growth of power demand. The probable locations predicted by a computerized optimization model eventually will be used in analyzing the environmental impact of alternative future energy supply strategies. The first stage of this work is reported in the first article.

APL is contributing to the development of a number of new energy systems. By 1973, it had analyzed energy technologies and concluded that the use of low-grade heat will provide increasingly important alternatives to scarce fossil fuels. These sources include solar thermal, geothermal, and waste heat. Programs were initiated in-house in the areas of ocean thermal energy (solar energy stored in tropical oceans), geothermal applications, and annual storage systems that save summer heat for winter use.

Subsequently, APL has become a leader in developing the concept of utilizing ocean thermal gradients to produce ammonia. Domestic ammonia, used in nitrogen fertilizers, is now made from natural gas. The APL version of Ocean Thermal Energy Conversion (OTEC) could have a substantial impact on natural gas consumption in the United States. Efficient heat exchange at small temperature differences is important to the success of the OTEC concept, and APL's efforts have included heat exchanger design and evaluation.

Biofouling could degrade the performance of heat exchangers. In the second article, experiments to measure the rate of biofouling and its effect on heat transfer are reported. Preliminary studies of cleaning mechanism are discussed. Work is also proceeding on issues relating to the commercialization of OTEC. Studies are being initiated on the design and response to stress of the massive concrete pipe that would be required to bring cooling water from the deep ocean (3000 ft) to the surface.

The work reported in the third article on the Community Annual Storage Energy System (CASES) seeks to explain how summer heat can be economically recycled for use in winter by means of annual storage on a community basis. It is anticipated that subsequent phases of the effort will address site-specific questions and lead to a demonstration and evaluation program.

A number of other energy-related programs are continuing. Pioneering work has been done in the development of efficient flywheels from filamentary materials. The next phase of this work will be to demonstrate a complete low-cost flywheel energy-storage system based on 110 V, 60 Hz power.

APL is responsible for studies of geothermal resources in the Department of Energy/Division of Geothermal Energy Region 5. Scenarios are being developed that outline the potential magnitude of identified resources with development and use schedules, and problems that must be surmounted before the resource could be used are being identified. Site-specific studies of potential geothermal energy applications are being initiated at three locations.

In addition, institutional impediments to the development of low-head hydroelectric power are being studied. Research is being conducted on the systematic development of organic conductors and on the active acoustic detection of leaks in underground natural gas lines.

The articles included herein are only a sample of the energy work being done at APL. Many areas indicated in this introduction are not reported. These and other projects will be reported in subsequent *Accomplishments* volumes.

REGIONAL MODEL FOR LOCATING POWER PLANTS

Assessing the environmental impact of various courses of action to meet the Nation's needs for electric energy is impossible without some idea of the locations of future power plants. APL has developed a computer model that predicts probable locations for large numbers of future power plants within a multistate region.

BACKGROUND

In the past few years, "energy scenarios" have gained increasing favor among planners for the use of electric power. An energy scenario is a hypothetical course of events that might occur as the result of a given set of energy supply decisions, usually on a national level. Recently, planners have come to realize that projections of energy variables on a national level are of little help in estimating the chances of achieving a given energy supply/demand state and in assessing the possible ways to achieve it. Analysis at a finer geographic level is required. The concept of a multistate region is in favor because physical resources (e.g., river basins) often cover several states and because electric power production and distribution systems often extend over several states.

Current computer models produce schedules of power plants needed to implement a given electric energy scenario, on both a national and a regional basis. The regional versions simply provide a list of specified power plants that must be brought into service in a multistate region within a specified time. In order to deal with environmental impact questions, however, a finer geographic resolution is required. APL's computer model (Ref. 1) provides this finer spatial resolution by predicting probable locations within a multistate region for large numbers of power plants associated with the given energy supply scenarios. The locations are not precise enough for actual siting efforts; however, they are sufficiently accurate for use in studies that attempt to evaluate the cumulative environmental impact of the scenarios.

DISCUSSION

The model has a grid of cells, each 240 sq mi, which corresponds exactly to the 15-minute quadrangle map system of the United States Geological Survey. The cell is the smallest element of locational resolution. After manual screening to eliminate cells with obvious negative features (such as lack of adequate cooling water), the remaining cells are designated as potential power plant locations. Figure 1a shows the cell grid and potential location cells superimposed on a map of the mid-Atlantic test region.

The regional electric power demand for some future time (the year 2000 was used in initial tests) is input to the model, which allocates the demand to load centers across the region on the basis of population projections. The model then uses linear programming to locate nuclear and coal-fired power plants to satisfy the demand while optimizing a specified objective and while ensuring that a set of constraints is not violated. The objectives and constraints are intended to represent real-world goals and restrictions associated with power plant siting; a great deal of input from regional electric utility planners and state regulatory officials was needed in their formulation.

Constraints currently embodied in the model include limitations on consumption and withdrawal of cooling water, restrictions on the proximity of populations to nuclear plants, limits on coal availability, and standards for ambient air quality. The cooling water constraints are of special interest, since they are formulated for the entire region, which encompasses all or part of six major river basins. The model shows the effect on all downstream users of all consumptive withdrawals at any point in a basin and thus could be used as a planning tool for water resources.

The objectives chosen for the initial development of the model include the minimization of required electric power transmission, of required coal transportation, of required reservoir capacity (region-wide) necessary to provide low-flow augmentation, and of aggregate population proximity to nuclear plants. The first three objectives serve as surrogates for costs that depend on location, while the population objective reflects the component of regulatory and public opinion that favors siting away from population centers. The objectives can be used in weighted linear combinations, the weights being proportional to the supposed importance of the corresponding objectives. Interaction with State and Federal officials, industry planners, and the public is necessary to determine the relative importance of each objective.

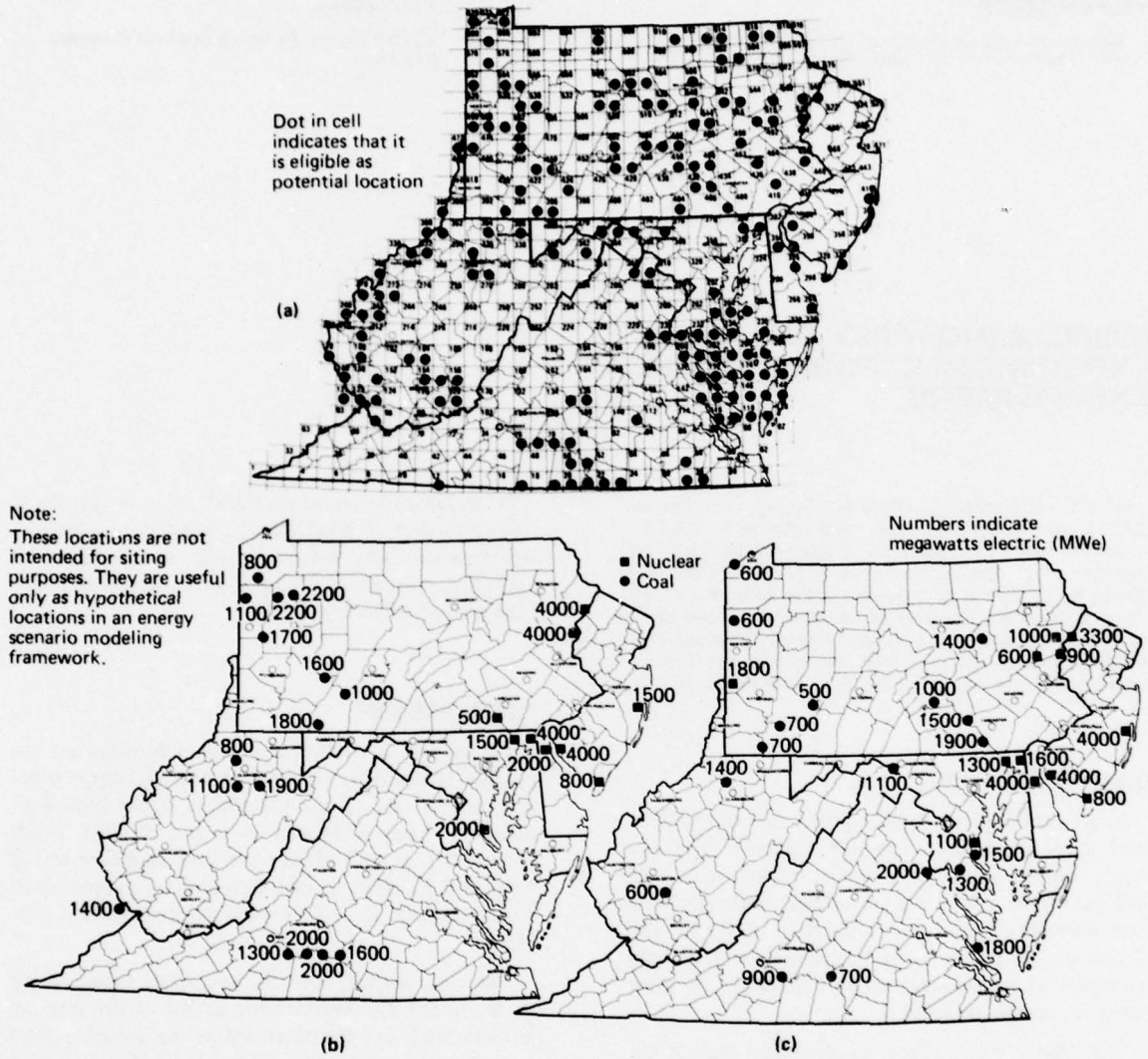

Fig. 1 Mid-Atlantic test region. (a) Eligible cells after screening; (b) location pattern that minimizes coal transportation; (c) location pattern that most closely resembles utility siting plans.

For initial testing, the model was exercised by requiring it to locate 25 000 MWe of nuclear capacity and 25 000 MWe of coal-fired capacity, an amount corresponding to a 2.7% annual regional growth rate from 1977 to 2000. Figure 1b shows the resultant locations for an extreme case in which the minimization of coal transportation was given the greatest weight. The location pattern that most closely resembles utility siting plans is shown in Fig. 1c. This pattern arose when minimization of transmission and of flow augmentation were given equal and primary importance, coal transportation was made much less important, and population proximity was not considered at all (beyond meeting legal regulations).

Future efforts will be directed toward determining definitive objective weights and extending the model to other regions of the United States.

REFERENCE

1. *Probable Distribution of Effluent Sources from Energy Supply and Conversion*, APL/JHU Final Report (to be published).

Author: *T. W. Eagles*

Support: *Electric Power Research Institute Contract RP953-1*

BIOFOULING AND CLEANING EXPERIMENTS FOR OTEC HEAT EXCHANGERS

In the APL Ocean Thermal Energy Conversion (OTEC) plant-ship concept, large-diameter (3-in.) aluminum tubes with ammonia flowing inside are being proposed for use as low-cost multipass heat exchangers. Experiments to measure the rate of biofouling and its effect on exterior heat transfer have been conducted by APL at the Natural Energy Laboratory of Hawaii, Ke-Ahole Point, Hawaii. The results are directly applicable to the design of the APL heat exchanger.

BACKGROUND

In an OTEC plant, warm surface seawater will be used in evaporators to vaporize ammonia. The ammonia vapor will drive a power turbine and then will be condensed by means of heat exchange with cold seawater drawn from a depth of 2500 ft. The electric power produced by the turbine will be used on board to produce ammonia, aluminum, or other energy-intensive products.

The plants will succeed commercially only if the overall system cost is low. A promising low-cost heat exchanger concept (Ref. 1) has arrays of large-diameter (3 in.) multipass aluminum tubes for both the evaporator and the condenser, with ammonia as the working fluid flowing inside the tubes. Seawater is pumped to head ponds above the tubes and flows vertically downward over them by gravity.

The use of large-diameter tubes results in a configuration that has sufficient space in the vertical planes between rows of tubes to permit a low-cost system of cleaning heads to remove the biofouling from the outside of the tubes.

Since biofouling is a critical factor that affects the long-term performance of the heat exchanger, experiments were needed to measure its effect and to develop low-cost cleaning methods in an environment similar to that of actual OTEC plant-ship operation. An apparatus was designed, built, and deployed in Hawaii, a potential OTEC site, and experiments have been conducted since mid-1977.

DISCUSSION

Figure 1 is a schematic of the biofouling test apparatus. It simulates an array of heat exchanger tubes arranged in one of the geometries under consideration. The array is located in a box through which seawater is passed. There are five lateral rows of tubes and 10 tubes in each longitudinal column, with a separation of 1¼ in. between adjacent vertical tube banks.

The first, fourth, seventh, and tenth tubes (tubes A, B, C and D, respectively) of the center row are instrumented as described below to measure heat transfer. The remaining tubes are made of Alclad 3004 aluminum and are vented to overcome buoyancy. These dummy tubes are held in position by 0.75-in.-thick spacers epoxied in place at the ends.

Each instrumented tube (Fig. 2) consists of a 6061 aluminum heat sink with an exposed length of 5½ in. One end of the tube extends through one side of the test box. The heat sink is heated by a 5½-in.-long, 400-W (nominal) quartz lamp that is inserted into a 1¼-in.-diameter axial hole. The heat sink is divided into four quadrants and instrumented with thermocouples so that heat transfer is measured on the top, bottom, and both sides. After the lamp is turned on, the heat sink reaches a steady-state temperature on each quadrant in approximately five minutes. The heat transfer coefficients are computed

from the magntiude of these temperatures, and the week-to-week changes in the coefficients determine the biofouling coefficients. (The biofouling resistance coefficient is defined as $R_f = 1/h_{fouled} - 1/h_{clean}$, where h is the measured heat transfer coefficient for the surface.)

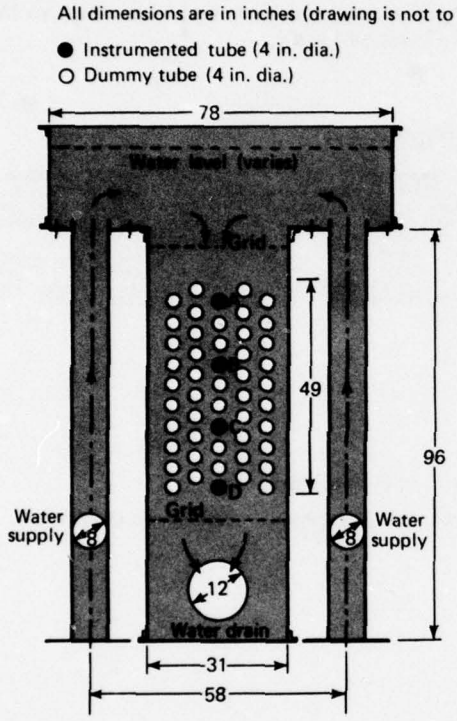

Fig. 1 Test setup showing the staggered tube arrangement simulating the full-scale geometry of the OTEC plant-ship heat exchanger.

As of September 1977, two series of tests have been run. During series I (30 May to 15 July 1977), the flow rate through the assembly was set at approximately 1775 gal/min, which gives a maximum flow velocity of 3 ft/s in the minimum gap of the tube array. The top of the test tank was left uncovered, and data were taken at approximately weekly intervals. Series II (10 August to 21 September 1977) duplicated the conditions of the first except that the top of the test tank was covered to exclude light from the upper parts of the test assembly.

Results from these tests are illustrated in Fig. 3, in which the average fouling coefficient for each tube is plotted against time; details of the fouling growth on each quadrant may be found in Ref. 2. An APL-designed scrubber mechanism using Scotchbrite pads that fitted into the spaces of the tube bank was used at the end of Series II. The following observations were made:

1. Bifouling accumulates at a rate to produce in six weeks a resistance to heat transfer measured as 0.00045 $Btu^{-1}ft^2$-h-°F with a standard deviation of 0.00011.
2. Light versus dark environment is indicated to have a significant effect on the rate of biofouling only in areas of low water velocity.
3. Tube sides tend to develop a smaller fouling coefficient than the tube top or bottom. The tube bottom tends to have the highest fouling coefficient, especially if there is no other tube directly below it.
4. The biofouling accumulation of six weeks is readily removed by light scrubbing with a plastic sponge (Scotchbrite).

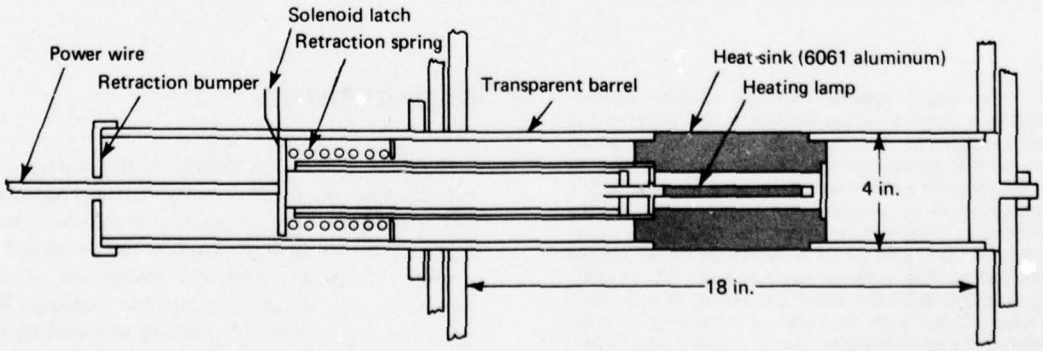

Fig. 2 Schematic of an instrumented tube.

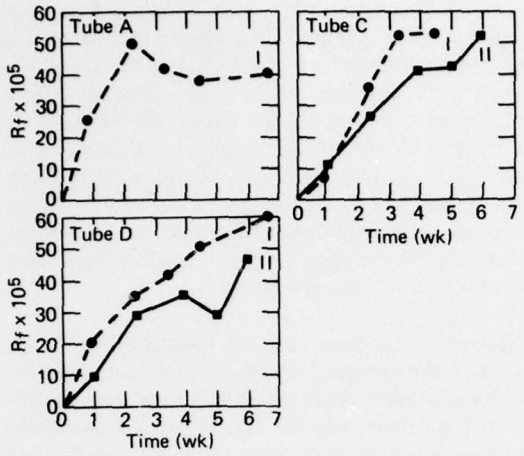

Fig. 3 Average fouling coefficients of tubes (four quadrants) plotted versus time for two test series, based on available data.

5. The cleaning mechanism was effective in cleaning the side quadrants of the array but was only partially effective on the top and bottom quadrants. The results are encouraging but indicate the need for improvement of the device.
6. The presence of iron oxide from the pumps may have affected the character and rate of growth of the biofouling layer.

Subsequent testing is planned with the apparatus in order to develop a cleaning system directly applicable to the APL/OTEC concept. Since several cycles of fouling and cleaning are necessary to determine the effectiveness for design purposes, the first tests give a preliminary indication that biofouling can be controlled cost-effectively.

REFERENCES

1. G. L. Dugger, H. L. Olsen, P. P. Pandolfini, and W. H. Avery, "Experiments on and Design of Low-Cost Aluminum Heat Exchangers for OTEC Plant-Ships," presented at the Fourth Ocean Thermal Energy Conference, New Orleans, LA, 22–24 March 1977 (sponsored by the Solar Energy Division of ERDA).
2. P. P. Pandolfini, W. H. Avery, J. Jones, and L. R. Berger, "Effect of Biofouling and Cleaning on the External Heat Transfer of Large Diameter Tubes," presented at the Biofouling and Corrosion Symposium, Seattle, WA, 10–12 October 1977.

Author: ***P. P. Pandolfini***

Support: ***U.S. Department of Commerce, Office of SEAGRANT***

SIMULATION OF A COMMUNITY ANNUAL STORAGE ENERGY SYSTEM

The Community Annual Storage Energy System (CASES) is a thermal utility that provides heating and cooling services to a community via water pipelines from a central energy-storage facility. A simulation by computer modeling has been developed for calculating the requirements of an entire community when heating and cooling is supplied by means of CASES. It calculates the size and cost of all water-source heat pumps and fan-coil cooling units in each building of the community together with the electrical energy they require each hour of the year to cope with varying weather conditions. It also calculates the size and cost of every pipe used to distribute heating and cooling water after first determining the peak flow condition in each pipe.

BACKGROUND

The key element in CASES is the storage of surplus thermal energy in a central facility. Much of the heat required by the community is collected "energy-free" at times of heat surplus and is stored until needed. Ice is also collected energy-free in winter and saved to be used for summer cooling. Water-source heat pumps supply heating and cooling whenever the store of energy-free ice and thermal water is inadequate for the community's needs.

Since much of the energy required for heating and cooling is collected as surplus summer heat or winter ice, energy from other sources for heating and cooling can be reduced by as much as 80%. It appears possible that the total capital invested for heating and cooling may be less than electric utility companies, building owners, and oil companies would have to invest for electrical air-conditioning and conventional heating systems. Building owners can subscribe to the CASES utility instead of purchasing independent heating and cooling equipment, thereby considerably reducing building costs.

SUMMARY

The CASES simulation begins by analyzing the heating and/or cooling required each hour for each distinct building type found in the community (the HCLOAD program module). The annual peak heating load is used to size the water-source heat pump in each building; the annual peak cooling load similarly determines the size of the fan-coil cooling units. Next, the demand (lb/h) for distribution-pipeline water at each building site corresponding to the heating and cooling load (Btu/h) schedules is calculated, making use of the performance characteristics of the selected heat pumps and fan-coil units.

The electrical energy required each hour to operate this heating and cooling equipment in each building is also calculated (the CDIST program module). Finally the size of every pipe used in the distribution system is determined so that the peak annual flow will be less than a specified maximum flow rate. Thus, by means of the HCLOAD and CDIST program modules, the entire community is reduced to an hourly schedule of water and electric power requirements, and the cost of all community components (heat pumps, cooling coils, and pipelines) is known.

DISCUSSION

COOLING. Water at 40°F is distributed through pipes that extend throughout the community and is then passed through cooling coils in the various buildings. Leaving these cooling coils at a temperature of about 60°F, the water is returned to a central ice deposit where it is again cooled to 40°F prior to being repumped through the flow loop. The heat imparted to the water when it is used for cooling is saved within the system until needed or until it can be rejected without an energy-consuming heat pump. This is in contrast to conventional air-conditioning systems that remove heat from buildings and eject it by means of a heat pump (air conditioner) into the atmosphere, where it is lost.

HEATING. The community is heated by water-source heat pumps. Conventional air-source heat pumps become inefficient when the outside air temperature falls below 32°F, but the heat pumps used in CASES remain highly efficient because 60°F water distributed from the central CASES plant is always available as a source of heat. The heat pumps extract thermal energy from the water, lowering its temperature to 40°F. The 40°F water is returned to the central facility in the same 40°F mainline used for cooling water, thus avoiding additional piping. Likewise, the pipeline used to supply 60°F heat-source water to the heat pumps is the same 60°F pipeline used to return water to the central ice store during the cooling cycle. Thus, CASES has only two uninsulated pipelines, one for 40°F water and one for 60°F water, yet both heating and cooling are always available to all users.

Part of the heat that is used to warm the 40°F water to 60°F for recirculation to the community comes from the recovery of excess heat as discussed above. The remainder comes from the central plant and will be simulated in future CASES work. The central plant feels only the net demand for pipeline water. A significant fraction of the heating and cooling demand is satisfied by the synergistic interaction among the diverse buildings of the community.

COMMUNITY. It is necessary to specify the community in order to evaluate quantitatively the extent of synergistic interaction among the various buildings of the community and to predict the cost of heat pumps, cooling coils, and pipelines. The selected model community is similar to Wilde Lake Village in Columbia, Maryland. It has 8000 residents (2500 households) and 866 buildings in three neighborhoods (NE, NW, and N), which share a common village center, all on 2500 acres of land. There is a job in the community for each worker. The physical layout of the community is shown in Fig. 1. Table 1 gives the demography and distribution of residential units. Each neighborhood has its own elementary school and civic-commercial center. The middle school, high school, office buildings, factory, village shopping center, and CASES facility are centrally located, as shown in Fig. 1. A detailed study of the demographics of the community was conducted so that the relative number of employment and residential facilities could be determined.

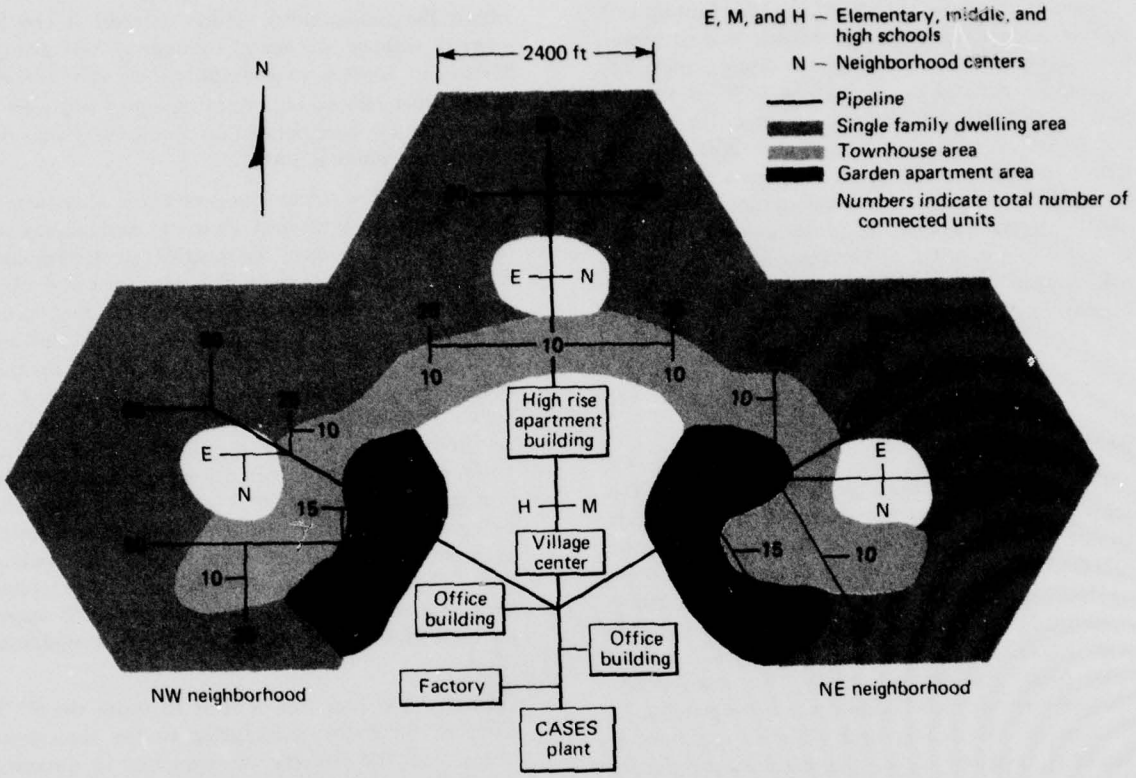

Fig. 1 Pipeline layout route for hypothetical CASES community.

RESULTS

There were interesting results from the simulation of only the community and the distribution system. An 866-building community almost identical to that described in Fig. 1 required 3.2×10^{11} Btu of heating and 8.8×10^{10} Btu of cooling in Washington area weather in 1967. Almost half of the cooling demand could be met by "waste-cold recovery" (chilled water produced by heat pumps used to heat other buildings), and about one-eighth of all heating was met by waste-heat recovery. The heating and cooling equipment required 6.3×10^{10} Btu of electrical energy. Thus, the combined seasonal coefficient of performance was 6.5, not counting central plant effects. The total CASES capital investment required for this community was $7.4 million (89% in heat pumps, 4% in cooling coils, and 7% in the distribution system). This is less than half the capital required to expand a winter-peak electric power plant to provide electrical heat to the same community (a plant cost of $700/kWe was assumed).

No effort has been made to optimize these CASES results, and it must be emphasized that the central CASES facility is not included in the simulation. However, both the cost and the losses of electrical energy during transmission have also been neglected in the analysis of the electric heating alternative.

CASES optimization will proceed when the central plant simulation (CAPS program module) has been completed.

Authors: *W. R. Powell, S. E. Ciarrocca, D. L. Thayer, and C. E. Williams*

Support: *Department of Energy, Argonne National Laboratory Contract 31-109-38-3995*

FUNDAMENTAL RESEARCH

INTRODUCTION

APL's continuing vitality as an institution stems in part from its dual role as a technology center for solving national problems and as a division of the University. This duality has provided a perspective on defense and civil concerns of national importance that looks to the fundamental issues and trends underlying the immediate pressing problems.

Institutionally, APL's university origins are reflected in its continuing support for research in the basic sciences of physics, chemistry, biology, and mathematics. Much of the work is relevant to the technologies used in Laboratory programs concerned with national defense, energy, and biomedicine. However, the motivation reflects a desire to understand the basic physical principles involved. This attitude provides continuing links with the academic and medical divisions of Johns Hopkins as well as with the international science community. At the same time, APL's competencies in these areas are a reservoir for technological innovation and a resource for solving specific problems where the application of current technology or engineering practice is inadequate. Research interests include topics in materials sciences, biology, chemistry, physics, and mathematics. Several notable contributions to these fields are summarized in the articles that follow.

In materials science, the work on corrosion processes in aluminum constitutes an attempt to understand the basic electrochemical and surface reaction mechanisms responsible for one important type of corrosion. Such an understanding should provide a guide for a more general understanding of this technologically important topic. In fluid flow, a closed-form solution is presented for a problem in the detachment of flow at a boundary. This work has direct application in aerodynamics and in arterial flow. In the area of applied

mathematics, large classes of problems can be solved only approximately. The next article is an example of new developments in the construction of general methods to obtain approximate solutions. Methods now under study at APL could find wide application in many areas of science and engineering.

Chemical physics is represented by two articles. The work on chemically induced polarization effects describes the development of a general analytical representation of reactions that produce electron and nuclear spin polarizations. These processes are important conceptually for understanding the mechanisms of an unusual class of reactions. For example, nuclear spin polarized targets are now used to enhance the yield of certain reactions in accelerator physics. They could also be important technologically. The next article sheds new light on energy levels and bonding in XeCl. These molecules arouse considerable theoretical interest and also are technologically important, since they constitute the active medium in the rare gas halide excimer laser now under development as an ultraviolet source.

Finally, the article on intensity correlation spectroscopy provides a view of work now in progress in the area of biological physics. It describes the development of analytical tools needed to apply optical correlation spectroscopy to the measurement of the properties of fluid suspensions.

These articles represent larger programs that include problems in hydrodynamics, energy conversion, reaction processes at solid surfaces (including corrosion), and biomedicine. Other major problem areas concern the electronic and optical properties of technologically important organic and metallic organic compounds and the development of high-energy laser devices.

LOCALIZED CORROSION OF ALUMINUM: BLISTER FORMATION AS A PRECURSOR OF PITTING

Various localized corrosion processes are thought to begin by similar mechanisms. A previously unkown step in the localized corrosion of aluminum known as pitting has been discovered in our laboratory; the passivating oxide on aluminum has been observed to blister and break prior to the onset of pitting corrosion.

BACKGROUND

The cost of corrosion in the United States has been estimated to be $20 to 30 billion. As much as 90% of this loss has been associated with localized corrosion processes such as stress-corrosion cracking, pitting, fatigue, and crevice corrosion. These processes are thought to have similar initiation mechanisms. That is, the first events are probably the same, even though the eventual gross manifestation of each corrosion type has distinct characteristics (for many articles on localized corrosion and initiation mechanisms, see Ref. 1). Our research has dealt with pitting corrosion, which takes the form of pits in the surface of the metal.

Associated with pitting is an electrical potential called the pitting potential. If the potential of a metal in a corrosive environment, such as aqueous chloride solution, rises above the pitting potential, pitting corrosion begins. Blisters in the oxide film on the metal have been observed in our laboratory before the onset of gross pitting. Our observations indicate that such blisters can be initiated by short-duration (less than 1 ms), low-voltage pulses. The blisters grow and eventually rupture, at which time pitting corrosion begins. Thus, blisters are experimentally demonstrable precursors of pits in this instance (Ref. 2).

DISCUSSION

The study of localized corrosion in aluminum requires the investigator to characterize the oxide film that covers and passivates the metal. This oxide can be grown in air as a nonporous film 2 to 4 nm thick. Films of greater thickness can be grown in solution by a process known as anodization. The films can be of various porosities, depending on the current and the chemicals. For our investigation, nonporous films 20 to 200 nm thick were grown.

The experimental configuration was similar to that shown schematically in Fig. 1. A light microscope was focused on the electrode to observe any visible phenomena. The potential on the aluminum electrode with respect to the reference electrode was maintained above aluminum's pitting potential. A very short potential pulse was applied to the aluminum electrode. This pulse initiated the growth of blisters.

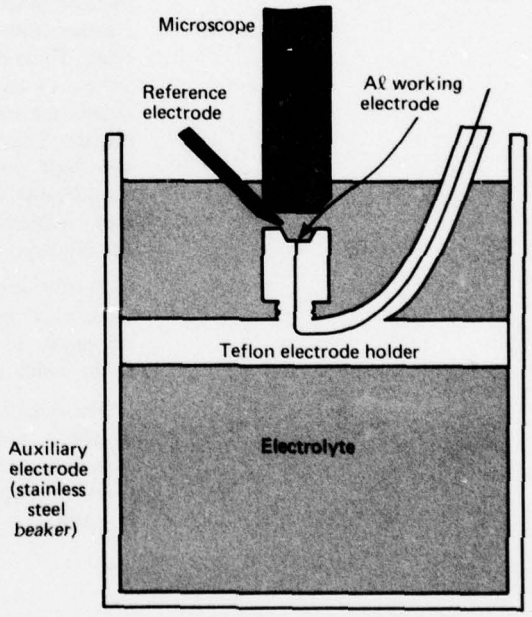

Fig. 1 The experimental configuration.

A typical unbroken blister 80 μm in diameter is shown in Fig. 2. The thickness of the specimen's oxide layer was 80 nm. Blisters usually have a circular shape, although their morphology can be influenced by grain boundaries and other topographical features. They appear under the low-power light microscope a few seconds after the voltage pulse is applied. Blister growth typically is somewhat jerky; that is, the blister boundary does not move steadily outward but rather increases by irregular increments with pauses in the boundary motion. During growth

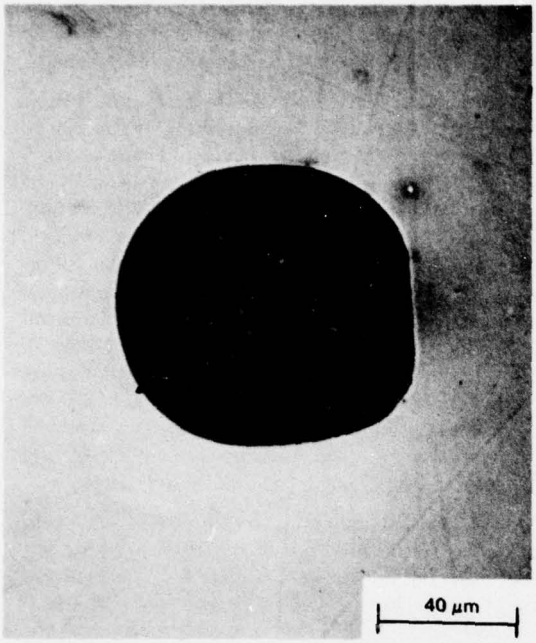

Fig. 2 A scanning electron micrograph of an unbroken blister. The beam voltage was 20 keV and the stage tilt was 30°.

there is an observable frontal region extending outside the blister periphery in which there appears to be activity or stress of some type. In the scanning electron microscope (SEM), the circumference of the blister frequently shows signs of stress. The shape, manner of growth, and stressed regions are all indicative of pressurized gas under the blistering oxide. The gas apparently is formed by a chemical reaction that attacks laterally along the oxide/metal interface as opposed to penetrating into the metal, although the dark spots seen in the blister are etch marks caused by a minor penetrating attack.

The micrograph shown in Fig. 2 was taken at 20 keV beam voltage. Micrographs taken at 2.5 keV do not reveal the etch marks; therefore, the marks are in the metal under the oxide. There are much larger amounts of chloride in the light contrast annulus about the blister periphery than inside the blister where chloride is occasionally detectable or outside the blister where it is usually not detectable in our apparatus. Close examination of the oxide over the blister in Fig. 2 revealed no detectable cracks or holes. The SEM has a resolution of 7 nm, but the nonconducting oxide reduces this resolution somewhat.

Several conditions must be met if one wishes to observe growing blisters initiated by a single pulse of 1-ms duration or less. A smooth surface is favorable. On rough surfaces, the oxide frequently breaks soon after pulsing. The anodized layer thickness also plays a role, as might be expected. The thinner layers break more easily; thus, blisters usually break at smaller diameters. The aluminum electrode potential must be above the pitting potential. Also, the pulse amplitude must be large enough. The amplitude depends on oxide thickness and is somewhat variable from specimen to specimen. In general, 2- to 3-V amplitudes are required for 20-nm oxides; 4- to 5-V amplitudes for 80-nm oxides; and greater than 10-V amplitudes for 200-nm oxides. If amplitudes much greater than these are used, the oxide usually breaks immediately. Pulse duration was not varied much in our tests; however, if the potentiostat is set at 2 V (referred to a saturated calomel electrode) for a period of a few seconds, many blisters form and grow under 80-nm films. Some of the blisters break and become pits.

Both intragranular and grain boundary sites have been observed as points of blister initiation on the aluminum surface.

Although blisters can grow to sizes on the order of 100 μm on smooth surfaces, they eventually rupture. Upon breaking, there is a considerable increase in the current (see Fig. 3). The time at which the specimen was pulsed is also indicated in the figure. In the case of a breaking blister, the current increases

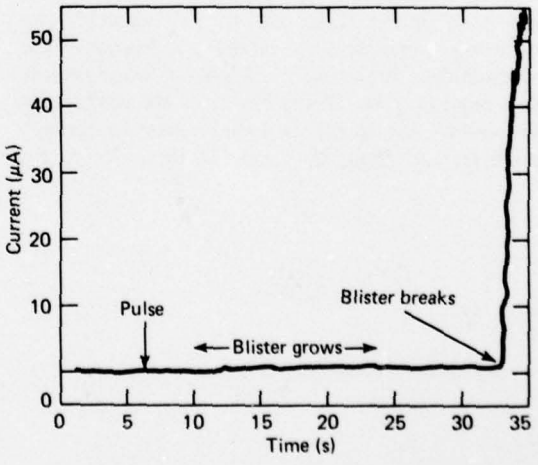

Fig. 3 A plot of current versus time showing the time of pulsation, the growth period, and the time of rupture.

because there is a greater area of unpassivated aluminum exposed to the electrolyte.

A question of considerable significance is that of the transport of materials across the oxide to the aluminum. No cracks or holes could be found in blistered oxide that had not broken catastrophically. A possibility is that such defects are below the resolution of our SEM. The oxide over a growing blister supports pressurized gas that would probably favor crack propagation. This does not usually happen immediately; when it finally does occur, the cracks often are outside the perimeter within which the blister was confined most of its lifetime.

Suppose that the voltage pulse has created (or opened) some holes of approximately circular cross section in the oxide. Since the oxide is reasonably hydrophilic, the following relationship holds:

$$p = 4T_s/d\,, \qquad (1)$$

where p is the gas pressure in the blister, T_s is the surface tension of the solution against the gas, and d is the pore diameter. Using $T_s = 75$ dyn/cm, if $d \leq 20$ nm, then p must exceed about 150 atmospheres to force gas bubbles through the pores into the bulk electrolyte. Thus, the gas remains trapped in the blister until the oxide itself ruptures, at which time many bubbles appear.

There is evidence that the same reactions that occur in pitting corrosion also proceed during blistering. Recall that blisters will not grow unless the aluminum's electrode potential is greater than the pitting potential. This elementary connection between blistering and pitting leads one to suppose that all the necessary reactants for the pitting reaction reach the bare metal during blister growth. An important step in pitting is considered to be the acidification of the pit electrolyte due to the hydrolysis of the metal ion. This requires water. The pathway of the reactants to the reaction site in this hypothesis must be through the holes and along the inside of the oxide to the periphery of the blister, which then becomes the prominent reaction site because elsewhere the film and the electrolyte are separated from the metal.

Although capillary forces probably play a role in transporting materials along the inside of the film to the reaction site, electrical forces could also be effective in this regard because the blister growth rate increases with increasing bias potential. The pressure within the blister may also be a factor in breaking open new pores near the periphery as the blister grows. As a result of the reaction occurring around the perimeter, the adhesion of the oxide to the metal in that region is lessened, allowing the blister to grow. It does so in an irregular incremental fashion because the detachment proceeds in a non-uniform spatial manner until the adhesion weakens sufficiently. The gas pressure then finishes the separation and reestablishes the roughly circular morphology.

Many relevant questions remain to be answered before the full significance of the blistering phenomenon can be appreciated. Certainly a demonstration of generality to other types of localized corrosion processes would be very important. Nevertheless, the discovery of an unknown step in a particular process is significant because it provides a helpful insight into a complex problem together with a new direction for future experimentation.

REFERENCES

1. "Localized Corrosion," B. F. Brown, J. Kruger, and R. W. Staehle (eds.) *NACE-3, Proceedings of Third Conference on Corrosion*, National Association of Corrosion Engineers, Houston, 1974.
2. C. B. Bargeron and R. B. Givens, "Localized Corrosion of Aluminum: Blister Formation as a Precursor of Pitting," *J. Electrochem. Soc.* 124, 1977, p. 1845.

Authors: C B. Bargeron and R. B. Givens

Support: NAVSEASYSCOM

SEPARATION FROM ALL CURVED SURFACES

Analytic descriptions of steady two-dimensional laminar separation from cylindrical surfaces, concave or convex, reveal universal 3:2:1 slope relations among a triplet of curves associated with separation. The curves are the streamfunction $\Psi = 0$, the along-wall velocity component $u = 0$, and the vorticity $\zeta = 0$.

BACKGROUND

The separation of fluid flow from the bounding walls is a recurrent problem in many technical areas. Conventional approximate boundary layer theory of the flow process, even for laminar two-dimensional flow, is incomplete, and any definitive statement is welcome. The demonstrated regularity of two-dimensional viscous flow separation (in contrast to the singularities of boundary layer theory) generalizes to all curved surfaces the result first enunciated for flat walls by the German aerodynamicist, Oswatitsch, in 1957 (Ref. 1).

DISCUSSION

It has been nearly 75 years since Ludwig Prandtl (Ref. 2) showed that the separation of a viscous boundary layer from a body in a flowing fluid made a significant difference in the expected inviscid pressure field about the body. Designers of aerodynamic control surfaces, turbine manufacturers, and artificial heart valve specialists are but a few of the people who are concerned about predicting and understanding the separation phenomenon. It is illustrated schematically for two-dimensional laminar flow in Fig. 1. Although the bulk of the fluid is flowing smoothly to the right, there is a region of reversed flow (leftward) along the wall. It bends outward and ultimately also flows to the right. The curve that contains this turning flow is the separation streamline, $\Psi = 0$, and the point, S, on the wall is called the separation point. Sometimes the separation streamline turns downward and intersects the solid wall at a reattachment point, but more usually the free shear layer becomes turbulent if the flow Reynolds number, Re, is high, (Re is UL/ν, where U is the oncoming flow velocity, L a characteristic length, and ν the fluid's kinematic viscosity.)

Prandtl showed that the criterion for two-dimensional separation on a fixed wall was zero wall shear,

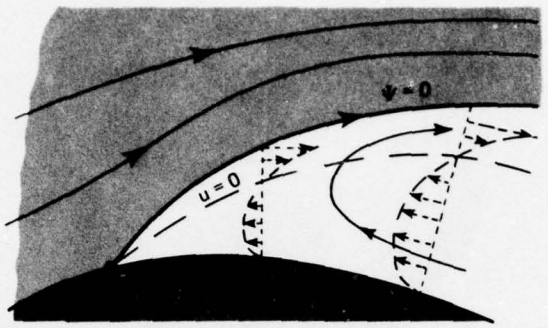

Fig. 1 Steady laminar two-dimensional separation.

or $(\partial u/\partial y)_s = 0$, where u is the velocity component parallel to the surface and y is the coordinate normal to the surface. Figure 1 shows several velocity profiles, $u(y)$, near the stagnation point. Also shown is the curve $u = 0$, which lies entirely within the separated flow region.

Within the boundary layer, viscous effects are very important. At the solid smooth wall, the viscous condition of nonslip must obtain for ordinary incompressible flow. Restricting the flow analysis to a local region near the separation point on a flat wall, Oswatitsch (Ref. 1) showed the angular relationship between the three important curves: the two-dimensional separation streamline $\Psi = 0$, the curve $u = 0$, and the curve $\zeta = 0$, where the vorticity, ζ, is the magnitude of the curl of the velocity vector ($\boldsymbol{\zeta} = \nabla \times \mathbf{q}$, $\mathbf{q} = u\hat{\imath}_x + v\hat{\imath}_y$). At S, where the curves all intersect the wall, $\zeta = \partial u/\partial y$, so this is in accord with the Prandtl criterion. Near S on the flat wall, the curves $\zeta = 0$, $u = 0$, and $\Psi = 0$ have slopes 1:2:3.

Although the practical concern for separation often is related to high midstream Reynolds number, separation can also occur at very low Reynolds number (so-called Stokes flows). Two such cases that might occur near rotating shafts are illustrated in Fig. 2. In Fig. 2a the outer cylinder of a pair of eccentric cylinders is rotating with constant angular velocity, Γ; the inner cylinder is stationary. Note the separation streamline, $\Psi = 0$, which intersects the convex fixed cylinder at the separation point, S, and the reattachment point, S'. In Fig. 2b the inner cylinder is

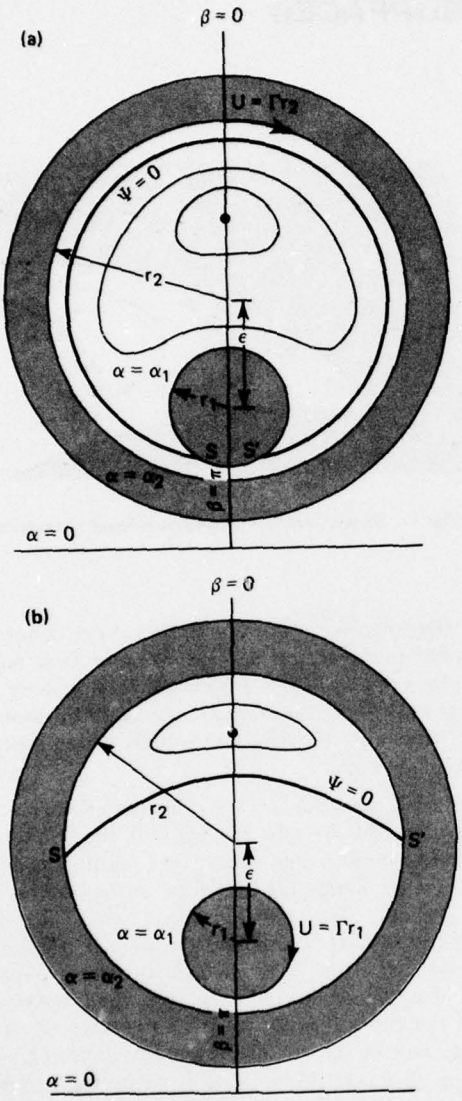

Fig. 2 Eccentric cylinder Stokes flows. (α, β) are bicylindrical coordinates. (a) Outer cylinder rotating (Re = $Ur_2/\nu << 1$); (b) inner cylinder rotating (Re = $Ur_1/\nu << 1$).

rotating and the outer cylinder is fixed. The stagnation points, S and S', now occur on the outer concave cylinder. The exact closed-form analytic expressions in bicylindrical coordinates for the respective Stokes flows are known, and the details near S and S' have been investigated (Ref. 3).

The two cases illustrated are complementary, for it can be shown that on the convex surface (Fig. 2a) or the concave surface (Fig. 2b), the angular relationships between each of the three intersecting diagnostic curves and the wall are exactly the same. The angle of departure of the separating streamline depends on the relative size of the circular cylinders and the eccentricity, but the relationship of that angle to those of the other two curves is the universal rule.

Locally, near the stagnation point (either separation or reattachment), let $\eta = \ln r/r_i$ $(i = 1,2)$ and let θ be the angle measured from the wall surface at S. The conformal flow domain corresponding to Fig. 2a is the upper part of Fig. 3; that corresponding to Fig. 2b is the lower part, as indicated. Either way, the diagnostic curves have the 1:2:3 slope relationship near S (or S'). Therefore, the concavity or convexity of the surface has no effect on the viscous relationships near the stagnation points. Neither does the real radius of curvature, since it is used for the normalizing length, L, in the analysis. Cavitation can occur within the lubricating fluid where separated regions are indicated in incompressible flow.

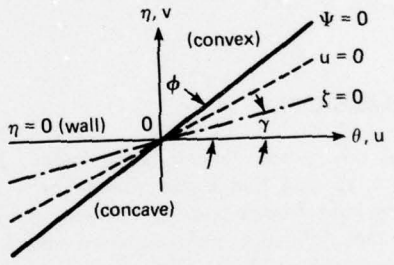

Fig. 3 The three important analytic curves near separation. (η, θ) are local orthogonal coordinates (a conformal transformation).

Also, the two-dimensional normalized pressure field, p', is orthonormal to the vorticity field, ζ; i.e.,

$$\frac{\partial p'}{\partial \eta} = \frac{\partial \zeta}{\partial \theta}; \quad \frac{\partial p'}{\partial \theta} = -\frac{\partial \zeta}{\partial \eta}, \tag{1}$$

where $p' = pL/(\mu U)$. Since the dimensional wall shearing stress, τ, is proportional to vorticity, other relationships at separation (Ref. 1) generalized to curved surfaces are

$$\tan \gamma = \frac{(\partial \zeta/\partial \eta)_s}{(\partial \zeta/\partial \theta)_s} = \frac{(\partial \tau/\partial \eta)_s}{(\partial \tau/\partial \theta)_s} = -\frac{(\partial p'/\partial \theta)_s}{(\partial p'/\partial \eta)_s}. \tag{2}$$

The exact Stokes analysis shows how the location and angle of the departing separation streamline from a given rounded surface (concave or convex) depend

on the relative size and eccentricity of the driving cylinder. In pressure terms, the recirculation region on a curved wall depends on the induced pressure gradients, *not on the wall curvature per se*. The angle of departure is determined by the local ratio of normal and tangential pressure gradients.

As Re increases from nearly zero, the flow patterns in the eccentric cylinder flows are modified. Within a given geometry, one can expect the two-dimensional separation streamlines to change shape and the attachment (and reattachment) points to migrate from those of Stokes flow; yet locally near the stagnation points where the convection term goes to zero, the balance is still between dissipation and pressure forces, and the local flow is a Stokes flow. Therefore, on all curved boundaries the local detaching/reattaching two-dimensional flows resemble those discussed here; only the intersection angles can change, not the relationships among the characteristic curves.

The analytic singularity found near the separation point by ordinary two-dimensional boundary layer theory on flat or curved bodies under a prescribed external streamwise pressure gradient signals theoretical difficulty. The singularity corresponds to a normal departure of the separation streamline, inconsistent with the acute angle departure usually found when the total momentum equation is used. The analysis of the local stagnation region must incorporate other local flow information as well as an upstream flow having a similar high Reynolds number to ensure the universal regularity of separating laminar flow shown by the viscous angular relations.

REFERENCES

1. K. Oswatitsch, "Die Ablösungsbedingung von Grenzschichten" ("The Detachment of Boundary Layers"), *Symposium on Boundary Layer Research*, H. Gortler (ed.), Springer-Verlag, Berlin, 1958, pp. 357–367.
2. L. Prandtl, "On Fluid Motions with Very Small Friction," *Proceedings Third International Mathematical Congress*, Heidelberg, 1904, pp. 484–491 (see NACA Technical Memo 452).
3. V. O'Brien, "Analytic Description of Steady Separation from Curved Surfaces," *Phys. Fluids* **20**, No. 7, 1977, pp. 1045–1049.

Author: *V. O'Brien*

Support: *NAVSEASYSCOM*

EXPLICIT L_2 INEQUALITIES FOR PARABOLIC EQUATIONS WITH NEUMANN BOUNDARY CONDITIONS

Explicit integral inequalities are presented for second-order diffusion equations with Neumann boundary conditions. Such inequalities are used to approximate solutions to partial differential equations by the method of a priori inequalities.

BACKGROUND

Suppose one wishes to determine the distribution of temperature, $u(x,y,t)$, over a region, R, subject to the *initial* condition,

$$u(x,y,0) = F(x,y) \qquad (1)$$

for time $t = 0$, and the Neumann-type *boundary* condition for which the rate of temperature change on the boundary, ∂R, is given by

$$\frac{\partial u(x,y,t)}{\partial n} = G(x,y,t),$$

$$(x,y) \in \partial R, \qquad 0 < t < T, \qquad (2)$$

where $\partial/\partial n$ is the outer normal derivative on R. If the rate at which heat is put into R is $H(x,y,t)$, we find the temperature, $u(x,y,t)$, by solving the second-order parabolic partial differential equation,

$$\frac{\partial^2 u}{\partial x^2} + \frac{\partial^2 u}{\partial y^2} - \frac{\partial u}{\partial t} = H(x,y,t),$$

$$(x,y) \in R, \qquad 0 < t < T, \tag{3}$$

along with the initial conditions (Eq. 1) and boundary conditions (Eq. 2). Equation 3 is the heat or diffusion equation.

Except when R is very simple, the system (Eqs. 1, 2, and 3) cannot be solved exactly but must be approximated. The most commonly used methods of approximation are the finite-difference method and the finite-element method. In the finite-difference method, the differential operator is replaced by a difference operator on a network of points over R. This results in a system of linear equations (necessarily a large system to obtain accurate approximations) that is solved algebraically on a computer.

In the finite-element method, the solution is sought in the form of the minimum of a certain functional. The functional is minimized over a finite set of elements that usually are piecewise polynomials over a network of small triangles covering R. This also results in a system of linear equations that is solved by computer. The number of equations needed for accuracy compared to the finite-difference method is generally smaller, but the savings are offset somewhat by the need for more preliminary computations.

We wish to describe an alternate method of approximating the solution to the system (Eqs. 1, 2, and 3) that is not as well known as the above methods but which has more convenient features. This is the method of *a priori* inequalities.

DISCUSSION

As the name implies, this method requires that we use a certain type of integral inequality related to the system and called an *a priori* inequality because it is to hold for any sufficiently differentiable function, v, defined on the region, R. The appropriate *a priori* inequality to use for the system is

$$\iiint_C v^2\,dxdydt \le \alpha_1 \iint_B v^2\,dxdy + \alpha_2 \iint_S \left(\frac{\partial v}{\partial n}\right)^2 dsdt + \alpha_3 \iiint_C (Lv)^2\,dxdydt \tag{4}$$

where C is the time cylinder $R \times (0,T)$; B is the base of the time cylinder R at $t = 0$; and S is the side of the time cylinder $\partial R \times (0,T)$; and where v is any sufficiently differentiable function, with the notation

$$Lv = \frac{\partial^2 v}{\partial x^2} + \frac{\partial^2 v}{\partial y^2} - \frac{\partial v}{\partial t}\ .$$

The constants α_1, α_2, and α_3 depend only on the geometry of R and are independent of the function v. Explicit values for α_1, α_2, and α_3 have been obtained by us (Ref. 1).

Once we have the *a priori* inequality (Eq. 4), we may take any approximation, ψ, to the solution, u, and set $v = u - \psi$ in Eq. 4 to get the L_2 error estimate:

$$\iiint_C (u - \psi)^2\,dxdydt \le \alpha_1 \iint_B (F - \psi)^2\,dxdy + \alpha_2 \iint_S \left(G - \frac{\partial \psi}{\partial n}\right)^2 dsdt + \alpha_3 \iiint_C (H - L\psi)^2\,dxdydt\ . \tag{5}$$

Notice that the right-hand side depends only on the known quantities, ψ, F, G, and H. In particular, we can let

$$\psi = \sum_{i=1}^{m} a_i \varphi_i\ ,$$

a linear combination of some simple trial functions such as polynomials, where the coefficients, a_i, are chosen to minimize the right-hand side of the equation.

CONCLUSIONS

Using the method of *a priori* inequalities to approximate a solution to the system (Eqs. 1, 2, and 3) also results in a system of linear equations to be solved on a computer. The number of equations required for a stated accuracy will generally be even fewer than for the finite-element method. However, the trial functions in the method of *a priori* inequalities do not need to satisfy any particular boundary conditions, and the amount of preliminary calculations needed is generally less than for the finite-element method. The method presented here should be more efficient numerically in that fewer preliminary calculations and less computer time will be needed to solve a given problem to an accuracy comparable to those of the finite-difference or finite-element methods.

We are currently in the process of implementing this method as the basis of a computer software system.

REFERENCES

1. J. R. Kuttler and V. G. Sigillito, "Explicit L_2 Inequalities for Parabolic and Pseudoparabolic Equations with Neumann Boundary Conditions" (to be published in *Bull. Calcutta Math. Soc.*).
2. V. G. Sigillito, "Explicit *a Priori* Inequalities with Applications to Boundary Value Problems," *Research Notes in Mathematics Series*, No. 13, Pitman Publishing Ltd., London, 1977.

Authors: *J. R. Kuttler and V. G. Sigillito*

Support: *NAVSEASYSCOM*

REFINEMENT OF THE RADICAL-PAIR MECHANISM OF CHEMICALLY INDUCED ELECTRON POLARIZATION: VECTOR MODEL AND AN ANALYTIC SOLUTION

It has been shown that the evolution of the electron spin state of a radical pair may be described simply as the rotation of a three-dimensional vector representation of the spin state, where the rotation rate and axis are determined by the magnetic interactions within the radicals and by the electron-spin-dependent valence (i.e., chemical bonding) interaction between the radicals. The model yields a clear qualitative picture of how these interactions in chemically reacting radicals yield nuclear spin polarization of the reaction products and electron spin polarization of the radicals themselves (Ref. 1). Also, an analytic solution has been obtained to the Stochastic-Liouville equations for electron polarization. These equations are obtained by combining the vector equation for temporal evolution of the radical-pair electron spin with a diffusion term describing the spatial evolution of the pair (Ref. 1).

BACKGROUND

The radical-pair model of chemically induced magnetic polarization (Ref. 2) shows that the polarizations result from the combined effects of the interactions described in the following Hamiltonian:

$$\begin{aligned}\mathcal{H}(r) = &-J(r)\,(\tfrac{1}{2} + 2\mathbf{S}_1 \cdot \mathbf{S}_2) \\ &+ \mu_\beta(g_1\mathbf{S}_1 \cdot \mathbf{H} + g_2\mathbf{S}_2 \cdot \mathbf{H}) \\ &+ A_1\mathbf{I}_1 \cdot \mathbf{S}_1 + A_2\mathbf{I}_2 \cdot \mathbf{S}_2 . \qquad (1)\end{aligned}$$

The first term in Eq. 1 is the valence interaction where, as shown in Fig. 1, $J(r)$ is a short-range function of inter-radical separation, r, and $\mathbf{S}_1$ and $\mathbf{S}_2$ are the spins of the two radicals. The remaining terms are the Zeeman interaction of the electron magnetic moments, $\mu_\beta g_1\mathbf{S}_1$ and $\mu_\beta g_2\mathbf{S}_2$, with the external magnetic field, $\mathbf{H}$, and the electron-nuclear hyperfine interactions where $\mathbf{I}_1$ and $\mathbf{I}_2$ are nuclear spins on radicals

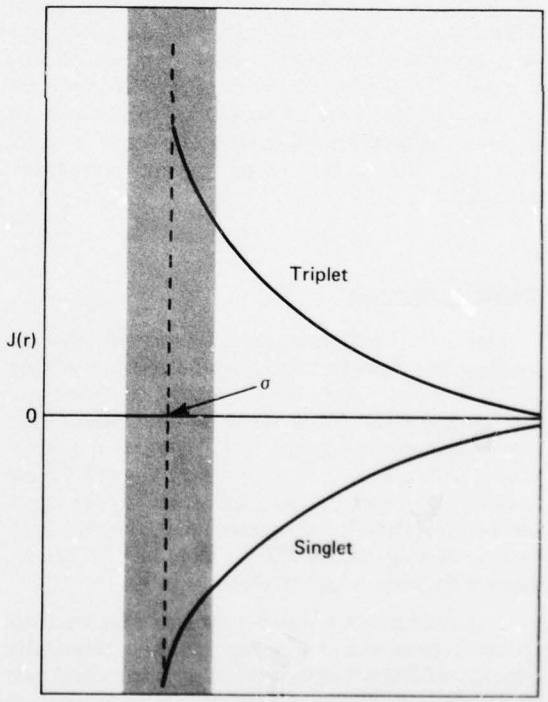

Fig. 1 Typical exchange interaction with a rigid sphere barrier at $r = \sigma$.

AD-A064 389 JOHNS HOPKINS UNIV LAUREL MD APPLIED PHYSICS LAB F/G 5/2
DEVELOPMENTS IN SCIENCE AND TECHNOLOGY.(U)
1977 N00017-72-C-4401
UNCLASSIFIED APL/JHU/DST-5 NL

2 OF 2
AD
A064389

END
DATE FILMED
4-79
DDC

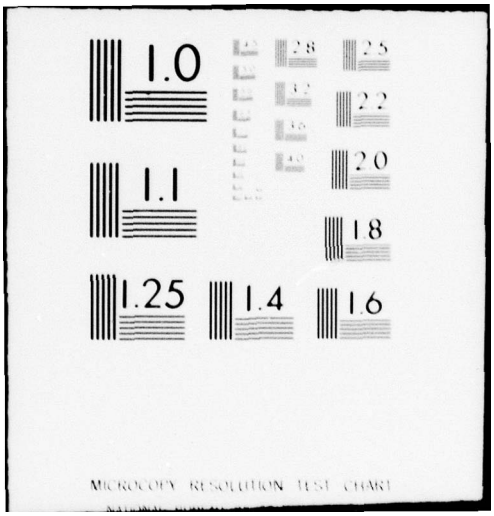
1.0
1.1
1.25
1.4
1.6
2.0
2.2
2.5
MICROCOPY RESOLUTION TEST CHART

1 and 2 and A_1 and A_2 are the corresponding hyperfine constants.

These nuclear-spin-dependent magnetic interactions can mix the chemically reactive singlet and chemically unreactive triplet electron spin states of the radical pair. This leads to nuclear polarization since certain nuclear spin states acquire or lose singlet character faster than others and are correspondingly more or less abundant in the radical-pair reaction products. This singlet-triplet mixing combined with the spin-selective valence interaction also leads to electron polarization; however, no suitable qualitative picture of this process was available until the development of the vector model described in this report.

Diffusion plays an essential role in the radical-pair polarization mechanism. Specifically, it enables some pairs to separate and subsequently reencounter each other after an intervening period of diffusion that is long enough to allow for significant singlet-triplet mixing by the weak, slowly acting magnetic interactions (Refs. 2 and 3). Quantitative treatment of diffusion is difficult because it requires the time-dependent Schrodinger equation to be solved for the radical-pair spin function with $J(r)$ a random function of time because of the diffusive motion. Previous treatments of this problem were either highly approximate or required numerical solution and none gave a really clear qualitative picture of the electron polarization process.

DISCUSSION

The radical-pair spin state is conveniently described by a density matrix whose components are $\rho_{ij}(t) = C_i C_j^*$, where the C's are the coefficients of the singlet and triplet states of the radical pair wave function, i.e., $\psi_{RP} = C_S(t)|S\rangle + C_T(t)|T\rangle$. Thus, $\boldsymbol{\rho}$ is a 2×2 matrix where C_S and C_T are complex quantities. ψ_{RP} is determined by the time-dependent Schrodinger equation $\mathcal{H}\psi_{RP} = i\partial\psi_{RP}/\partial t$, where $\mathcal{H}$ is given by Eq. 1; from this it can be shown that $\mathcal{H}\boldsymbol{\rho} - \boldsymbol{\rho}\mathcal{H} = i\partial\boldsymbol{\rho}/\partial t$.

It is convenient to transform $\boldsymbol{\rho}$ so that its components have the following real and physically significant forms at all times (since the radical pair is always a singlet, a triplet, or some combination thereof): $\rho_0 = \rho_{SS} + \rho_{TT}$, $x = \rho_{ST} + \rho_{TS}$, $y = -i(\rho_{ST} - \rho_{TS})$, $z = \rho_{SS} - \rho_{TT}$, $\rho_0 = 1$. The term z gives the relative amounts of singlet and triplet character. It can be shown that x is the electron spin polarization of the pair, where polarization means an excess of "up" spin on one radical and a matching excess of "down" spin on the other.

In the absence of diffusion, the time evolution of the components of this density matrix is given by the following simple vector equation:

$$\frac{d\hat{\boldsymbol{\rho}}}{dt} = \boldsymbol{\Omega}(r) \times \hat{\boldsymbol{\rho}}; \qquad \hat{\boldsymbol{\rho}} = \begin{pmatrix} x \\ y \\ z \end{pmatrix};$$

$$\boldsymbol{\Omega} = -2\begin{pmatrix} a \\ 0 \\ J(r) \end{pmatrix} \tag{2}$$

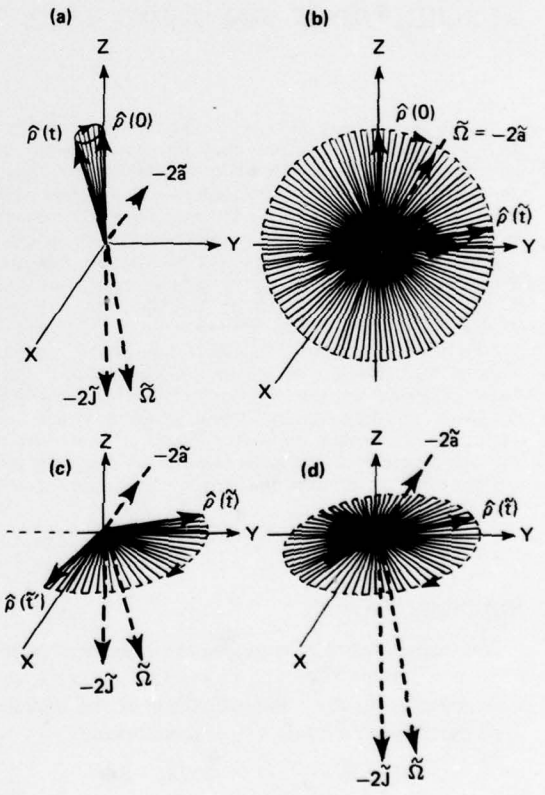

Fig. 2 Vector model of chemically induced nuclear polarization (CIDNP) and chemically induced electron polarization (CIDEP). (a) $S - T_0$ mixing quenched when $J \gg a$. (b) $S - T_0$ mixing when $a \geq J$. (c) CIDEP results from exposure to a sizable exchange interaction, $J > a$, after a period of $S - T_0$ mixing as shown in (b). (d) Electron polarization destroyed by spin exchange if radical pair remains too long in region of large J.

Here, × denotes the vector cross product and a is the singlet-triplet mixing rate given by

$$a = \tfrac{1}{2}\mu_\beta H(g_1 - g_2) + \tfrac{1}{2}A_1M_1 - \tfrac{1}{2}A_2M_2$$

where M_1 and M_2 denote the spin states of the nuclei.

According to Eq. 2, the rate of change of $\hat{\rho}$ at any time is a rotation of magnitude, $\Omega[r(t)]$, about an axis in the direction of Ω. As depicted in Fig. 2a, when the radicals are close together, J is much greater than a and the rotation of $\hat{\rho}$ is about the z axis; thus, the z component, which determines the relative amounts of singlet and triplet character of the pair, is unvarying.

As the radicals separate, $J(r)$ approaches 0, and $\hat{\rho}$ begins to rotate above the x axis, as shown in Fig. 2b. This changes the z component and corresponds to singlet-triplet mixing at rate a. However, this process alone cannot give $\hat{\rho}$ a component along the electron polarization axis, x. As shown in Fig. 2c, an x component can be achieved from the usual starting point of a pure singlet or triplet state (i.e., $\hat{\rho} = (0,0,\pm 1)$) if, after a period of singlet-triplet mixing, the radicals come close together again, whereupon the $\hat{\rho}$ vector (which is now in the yz plane) begins to rotate about the z axis at rate $J(r)$, thereby acquiring an x component.

Finally, as shown in Fig. 2d, if the radicals approach too closely, $J(r)$ becomes very large and $\hat{\rho}$ makes a number of complete revolutions about the z axis, thereby yielding an average value of zero for the x component. This last effect, known as spin exchange, occurs because the electrons become delocalized between the strongly interacting radicals and any electron spin polarization on one radical is distributed between the two radicals. Since the polarization in our case is an excess of up spins on one radical and a matching excess of down spins on the other, the polarization is averaged to zero by the spin exchange process.

Equation 2 is converted to the Stochastic-Liouville equations by adding a diffusion term (Ref. 4):

$$\frac{\partial\hat{\rho}(r,t)}{\partial t} = D\left(\frac{\partial^2\hat{\rho}(r,t)}{\partial r^2}\right) + \Omega(r) \times \hat{\rho} \quad . \qquad (3)$$

Since we are interested in the steady-state ($t \to \infty$) polarization, the time dependence can be eliminated from this equation by taking the Laplace transform and using the relation

$$\lim_{t\to\infty} f(t) = \lim_{s\to 0} s\bar{f}(s)$$

where $\bar{f}(s)$ is a Laplace transform. The resulting system of coupled differential equations can be transformed into a single integral equation for the electron polarization component x. For slow singlet-triplet mixing, which is the usual case, the kernel of this integral equation is positive-definite, symmetric, and compact. The kernel therefore has a complete set of eigenfunctions that happen to be zero-order Bessel functions, and the integral equation may be solved by expanding in these eigenfunctions. The solution for the usual case of a strong, exponentially decaying exchange interaction, $J(r) = J_0e^{-\lambda r}$, has the simple form:

$$\text{Polarization} = \frac{\pi}{2\lambda}\frac{J_0}{|J_0|}\sqrt{\frac{a}{D}} \quad .$$

This result agrees well with previous numerical calculations (Ref. 5).

REFERENCES

1. L. Monchick and F. J. Adrian, "On the Theory of Chemically Induced Electron Polarization (CIDEP): Vector Model and an Asymptotic Solution" (to be published in *J. Chem. Phys.*).
2. G. L. Closs and A. D. Trifunac, "Theory of Chemically Induced Nuclear Spin Polarization," *J. Am. Chem. Soc.* **92**, 1970, p. 2183; R. Kaptein and L. J. Oosterhoff, "Chemically Induced Dynamic Nuclear Polarization," *Chem Phys. Lett.* **4**, 1969, p. 214.
3. F. J. Adrian, "Role of Diffusion Controlled Reaction in Chemically Induced Nuclear Spin Polarization," *J. Chem. Phys.* **53**, 1970, p. 3374.
4. F. J. Adrian, "Theory of Anomalous Electron Spin Resonance Spectra of Free Radicals in Solution. Role of Diffusion-Controlled Separation and Reencounter of Radical Pairs," *J. Chem. Phys.* **54**, 1971, p. 3918.
5. J. B. Pedersen and J. H. Freed, "Theory of Chemically Induced Dynamic Electron Polarization," *J. Chem Phys* **58**, 1973, p. 2746.

Authors: ***L. Monchick and F. J. Adrian***

Support: ***Indirectly Funded R&D***

VALENCE-BOND STUDY OF HYPERFINE INTERACTIONS AND STRUCTURE OF THE NOBLE GAS MONOHALIDES

It has been shown that a semiempirical valence-bond (VB) model of the noble gas monohalides that includes electron correlation effects can account for the observed electron-nuclear magnetic hyperfine structure (hfs) interactions in these molecules (Ref. 1). The VB wave function is a linear combination of neutral and ionic VB structures, that is,

$$\Psi_{NX}(^2\Sigma) = \chi\Psi(N \quad X\cdot) + \sqrt{1-\chi^2}\,\Psi(N^+\cdot \quad X^-) \quad (1)$$

when N denotes the noble gas, X is the halogen, χ is the charge distribution parameter, and typically $\sqrt{1-\chi^2}$ is much less than 1. The dot denotes the location of the unpaired electron in a given VB structure. Electron correlation is included in this wave function by using different atomic orbitals for a neutral atom and the corresponding ion, and by considering the polarizing effects of van der Waals interactions in the neutral VB structure ($N \quad X\cdot$) and coulomb interactions in the ionic structure ($N^+\cdot \quad X^-$). The bond distance, R, and χ in the molecules XeF, KrF, and XeCl are determined as those values that give the best agreement between the observed and the calculated hyperfine structure constants (hfc).

BACKGROUND

The noble gas monohalides are a very interesting example of a class of molecules known as hypervalent radicals, so called because they contain an unpaired electron that cannot be accommodated by VB structures satisfying the classical Lewis octet rule. This rule predicts that noble gas atoms will not form chemical bonds because they already have a filled outer shell of eight electrons. In addition to their importance in terms of chemical bonding theory, their strong ultraviolet emission from an excited state corresponding to the ($N^+\cdot \quad X^-$) VB structure gives them practical importance as lasers.

The unpaired electron of these molecules makes them paramagnetic; consequently, much important structural information, especially the hfs interactions, can be obtained from experiments in electron spin resonance spectroscopy. Transitions are observed between energy levels associated with the interaction of the electron spin magnetic moment with an external magnetic field and with the magnetic nuclei. In order to translate the observed hfc into information about the electron charge distribution and chemical bonding, it is necessary to construct a model wave function for the system.

DISCUSSION

The hyperfine data for a given nucleus consist of an isotropic and an anisotropic hfc, denoted a and $B_\parallel$ respectively (Refs. 2 to 4). The value of a is determined by the unpaired electron density in the spherically symmetric s orbitals of the atom to which the nucleus belongs, whereas $B_\parallel$ is determined by the unpaired electron density in the nonspherically symmetric atomic orbitals, in this case the p orbitals. In molecules such as the noble gas monohalides, which contain heavy atoms, the spin-orbit interactions are large enough that the hfc contain a contribution from the orbital magnetic moment of the electron as well as from its spin moment. It is fairly straightforward to determine the pure spin hfc by subtracting an estimate of the orbital contribution from the experimental values (Ref. 1).

The calculation of $B_\parallel$ from the wave function of Eq. 1 is relatively straightforward because the unpaired electron is primarily located in valence p orbitals of the noble gas cation $N^+\cdot$ and the halogen atom $X\cdot$. Accordingly, $B_{\parallel,N}$ is approximately proportional to $(1-\chi^2)$, which is the weight factor of the ($N^+\cdot \quad X^-$) structure in Eq. 1, whereas $B_{\parallel,X}$ is approximately proportional to χ^2, which is the weight factor of the ($N \quad X\cdot$) structure. There is, however, an additional contribution to both $B_{\parallel,X}$ and $B_{\parallel,N}$ from a cross term involving the two VB structures. This term, whose weight factor is $\chi\sqrt{1-\chi^2}\,S$ (where S is an overlap integral with an order of magnitude of 0.1 to 0.2), is especially important for $B_{\parallel,N}$ because the direct term proportional to $1-\chi^2$ is usually small. Thus, the parameter χ can be determined with good accuracy from the anisotropic hfc alone.

The origin of the isotropic hfc is more subtle because, at the level of approximation denoted by Eq. 1, neither of the VB structures provides an unpaired electron density in the atomic s orbitals. The s-orbital density, and consequently the isotropic hfc, results from the following refinements to the model depicted by Eq. 1.

OVERLAP. In the VB structure ($N \quad X\cdot$), a small amount of the unpaired electron density in the valence pz orbital of X (i.e., a p orbital directed along the molecular bond) is transferred to the s orbitals of N via the overlap of the X_{pz} and N_s orbitals. Similarly the overlap of the N^+_{pz} and X^-_s orbitals in the VB

structure ($N^{+}\cdot \quad X^{-}$) transfers unpaired electron density from the *p* orbital of the noble gas cation to the halogen *s* orbital.

POLARIZATION. In the neutral VB structure ($N \quad X\cdot$), the polarizing interactions involve the effect of the instantaneous dipole moment of one atom on the other. This van der Waals interaction exists even though the average dipole moment of the atoms (obtained by averaging over the instantaneous moments associated with various electron positions) is zero. In the ionic VB structure, the polarization is due to the coulomb interaction between the electrons of one ion and the charge on the other. The polarization of the electronic charge clouds of the open-shell species $N^{+}\cdot$ and $X\cdot$ is spin selective and leads to the following isotropic hfs interactions. First, the polarization of the *pz* orbitals containing the unpaired electron involves a deformation of these orbitals, which gives them a small amount of spherically symmetric or *s*-orbital character. Second, the polarization-induced deformation of the closed-shell *s* orbitals, occupied by a pair of electrons of opposite spin, is spin dependent, thereby creating unpaired electron density in these orbitals. This occurs because the Pauli exclusion principle, which states that electrons of the same spin may not occupy identical orbitals, requires that the deformation of the *s* orbital with the same spin as the *pz* orbital not give it any of the shape characteristics of the *pz* orbital, whereas the deformation of the other *s* orbital is unrestricted.

OVERLAP-POLARIZATION. This is a contribution to the isotropic hfs from a combination of the aforementioned overlap effect and the polarization of the closed-shell *s* orbitals.

ATOMIC. This is the isotropic hfc of the isolated $N^{+}\cdot$ ion and the $X\cdot$ atom. The hfs term results from spin-dependent interactions between the closed-shell *s* orbitals and the unpaired electron in the valence *pz* orbital. The atomic hfc are known from experiment for the halogen atoms and have been estimated for the noble gas cations by extrapolation from the halogen values.

The calculated results are illustrated for XeF in Fig. 1, which gives the isotropic Xe and F hfc as functions of R and χ. As expected, the calculated values of hfc decrease rapidly with increasing interatomic distance, which reduces the overlap and polarization interactions. Comparison of the calculated and experimental isotropic hfc for XeF, also shown in Fig. 1, shows that theory and experiment agree well for $R = 4.70a_0$ and $\chi = 0.800$. R and χ were similarly determined for KrF and XeCl; all results and a comparison of theory and experiment are given in Table 1. The resulting values of interatomic distance

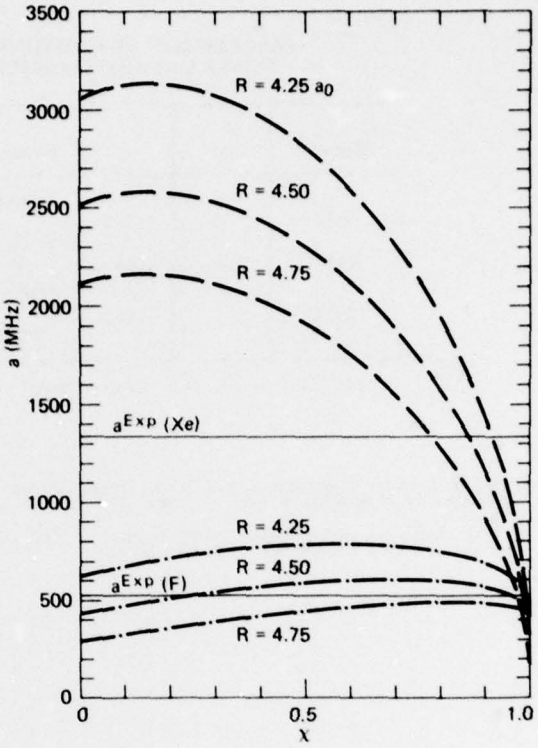

Fig. 1 Isotropic hyperfine constants for XeF as functions of χ and R.

are consistent with the relative sizes of the atoms, i.e., Xe > Kr and Cl > F. The values of χ show that the weight of the ($N^{+}\cdot \quad X^{-}$) state is greater in XeF than in either KrF or XeCl. It is reasonable that the $Xe^{+}F^{-}$ state plays a greater role in XeF than does $Kr^{+}F^{-}$ in KrF because the ionization potential of Xe is less than that of Kr. Similarly, the $Xe^{+}F^{-}$ state is more important in XeF than is the $Xe^{+}Cl^{-}$ state in XeCl because the F^{-} anion is considerably smaller than the Cl^{-} anion; hence the coulomb stabilization of $Xe^{+}F^{-}$ is greater than that of $Xe^{+}Cl^{-}$.

REFERENCES

1. F. J. Adrian and A. N. Jette, "Valence Bond Study of Hyperfine Interactions and Structure of the Noble Gas Monohalides," *J. Chem Phys.* 68, 15 May 1978.
2. J. R. Morton and W. E. Falconer, "Electron Spin Resonance Spectrum of XeF in X-Irradiated Xenon Tetrafluoride," *J. Chem. Phys.* 39, 1963, p. 427.

TABLE 1

COMPARISON OF COMPUTED HYPERFINE CONSTANTS OF THE NOBLE GAS MONOHALIDES WITH EXPERIMENTAL VALUES

Molecule	R (a_0)	χ	Nucleus	$a^{(Th)}$ (MHz)	$a^{(Exp)}$ (MHz)	$B_0^{(Th)}$ (MHz)	$B_0^{(Exp)}$ (MHz)
XeF	4.70	0.800	^{129}Xe	1340	1330	1227	1290
			F	509	523	2125	2126
KrF	4.00	0.98	F	552	549	2925	3093
XeCl	6.50	0.955	^{129}Xe	270	265	425	424
			^{35}Cl	37	37	260	305

Note: Th = theory, Exp = experimental

3. W. E. Falconer, J. R. Morton, and A. G. Streng, "Electron Spin Resonance Spectrum of KrF," *J. Chem. Phys.* 41, 1964, p. 902.
4. F. J. Adrian and V. A. Bowers, "ESR Spectrum of XeCl in Argon at 4.2K," *J. Chem. Phys.* 65, 1976, p. 4316.

Authors: ***F. J. Adrian and A. N. Jette***

Support: ***Indirectly Funded R&D***

LIGHT-SCATTERING MEASUREMENT OF PARTICLE SIZE DISTRIBUTIONS

Intensity correlation spectroscopy (ICS) is the most rapid and accurate method of obtaining macromolecular diffusion coefficients. In addition, it provides valuable measures of sample polydispersity. A method has been developed to extract size distribution parameters from ICS data and is applied to data on very low density lipoproteins (VLDL) from human serum.

BACKGROUND

One goal of our present research is to determine the size distribution of various classes of human serum lipoproteins in certain patients. We are examining these lipoproteins using ICS. Molecular diffusion coefficients and therefore particle sizes are determined from the autocorrelation function of the time-dependent intensity fluctuations in the light scattered from the particles as they diffuse in solution. This autocorrelation function can be analyzed by an expansion technique in which the coefficients, called cumulants, provide a general description of sample polydispersity (Ref. 1). If the form of the size distribution is specified, then the values of the parameters that characterize this form can be obtained directly from the cumulants (Refs. 2 to 4). Although this approach is less general, it is of great potential use in our research.

Our preliminary studies of VLDL, which are spherical particles with diameters ranging from 30 nm to more than 90 nm, indicated that the Gaussian distribution we deduced from the cumulants was physically unrealistic and that a rectangular distribution was impossible (Ref. 2). This finding established a clear need to extend our method to other, more useful, size distributions.

DISCUSSION

The general form of the intensity correlation function from a system of scatterers is $C(\tau) = A|g^{(1)}(\tau)|^2 + B$, where A, B, and τ are the amplitude, background, and delay time, respectively. For a single-sized molecular species, $g^{(1)}(\tau) = \exp(-Dq^2\tau)$, where the translational diffusion coefficient, D, is inversely proportional to the size of the scatterers. The factor q^2 is an instrumental parameter related to the laser wavelength and scattering angle.

In polydisperse systems, $g^{(1)}(\tau)$ is a sum of many such exponentials. Cumulant analysis provides the most general description of the autocorrelation function in such systems. In theory, the cumulants, K_m, are found from the Maclaurin series for $\ln g^{(1)}(\tau)$:

$$\ln g^{(1)}(\tau) = -\tfrac{1}{2} \ln A + \sum_{m=1}^{\infty} K_m \frac{(-\tau)^m}{m!} \quad .$$

In practice, the cumulants are computed approximately from a truncated series, where m is limited to 2 or 3 due to scatter in the experimental data. The first cumulant is related to the z-average diffusion coefficient of the scatterers by $K_1 = \langle D_z \rangle q^2$, and K_2 is related to the normalized variance of the distribution of diffusion coefficients by $K_2/K_1^2 = (\langle D_z^2 \rangle - \langle D_z \rangle^2)/\langle D_z \rangle^2$ (Ref. 1).

In addition to providing this general characterization of polydispersity, we have shown that cumulants can also be used to find the parameters of postulated distributions of model size. Three statistical functions that were useful in characterizing VLDL in this way are known as the Pearson V, the Pearson III, and the Schulz distributions (Ref. 4). Each of these functions has the form of a skewed, bell-shaped curve (Fig. 1) and is a function of parameters that are related rather simply to such quantities of interest as average size and the standard deviation of sizes. Using the explicit expressions for the first two cumulants, K_1 and K_2, we also showed that the ratio K_2/K_1^2 has distinct upper bounds for each of these distributions as well as for the Gaussian and rectangular distributions treated in Ref. 3. This property can often be used to rule out a distribution, as in the case of the rectangular distribution for VLDL. The usefulness of the method for describing VLDL sizes is illustrated in Fig. 1. The three

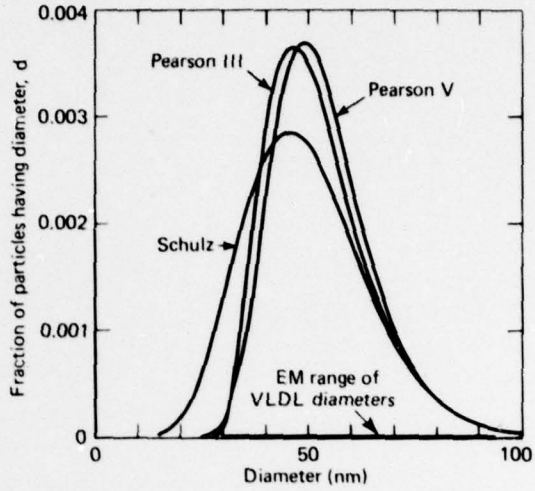

Fig. 1 The experimentally determined size distributions for VLDL. The expected range of VLDL sizes based on EM studies is shown on the baseline.

size distributions compare very favorably with the reported electron microscopic (EM) size range of VLDL. Experiments are presently under way to compare the size distributions obtained with EM and ICS measurements on the same samples.

REFERENCES

1. D. E. Koppel, "Analysis of Macromolecular Polydispersity in Intensity Correlation Spectroscopy: The Method of Cumulants," *J. Chem. Phys.* **57**, 1972, pp. 4814–4820.
2. C. B. Bargeron, R. L. McCally, and M. H. Friedman (APL) and S. Margolis (JHMI), "Particle Size Distributions of Human Plasma Lipoproteins by Intensity Correlation Spectroscopy," *Biophys. J.* **15**, Part 2, 1975, p. 251a.
3. C. B. Bargeron, "Measurement of a Continuous Distribution of Spherical Particles by Intensity Correlation Spectroscopy: Analysis by Cumulants," *J. Chem. Phys.* **61**, 1974, pp. 2134–2138.
4. R. L. McCally and C. B. Bargeron, "Application of Intensity Correlation Spectroscopy to the Measurement of Continuous Distributions of Spherical Particles," *J. Chem. Phys.* **67**, 1977, pp. 3151–3156.

Authors: ***R. L. McCally and C. B. Bargeron***

Support: ***U.S. Public Health Serice Grant HL-19095 and NAVSEASYSCOM***

JHU EVENING COLLEGE CENTER AT APL

THE APL GRADUATE EDUCATION CENTER

During its thirty-five years of existence, APL has used various methods to help its staff members maintain and improve skills needed to carry out their technical assignments in the most effective manner. The methods include financial support for pertinent programs at educational institutions and specialized short courses taught both inside and outside the Laboratory.

In 1964, in order to make some of APL's in-house courses available to all qualified persons regardless of whether they were employed by the Laboratory, the Evening College of The Johns Hopkins University and APL cooperated to establish a Graduate Center at APL oriented to the educational needs of employed scientists and engineers.

Under the academic sponsorship of the Evening College and with faculty members drawn primarily from APL's Senior Staff, the Center offers a variety of courses in scientific and engineering areas. Current programs lead to master of science degrees in Applied Physics, Computer Science, Electrical Engineering, Numerical Science, and Space Technology. Classes meet in the R. E. Gibson Library (Fig. 1).

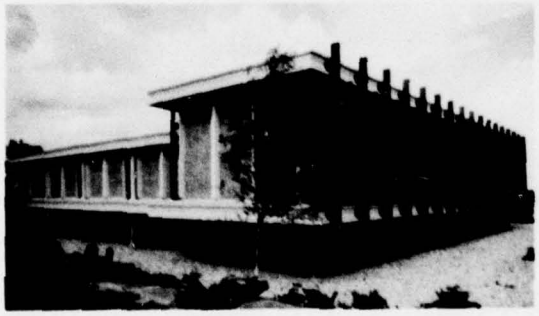

Fig. 1 The R. E. Gibson Library where Graduate Center classes meet.

During Fiscal Year 1977, class registrations for APL Center programs were as follows: Fall 1976, 748; Spring 1977, 700; Summer 1977, 224; and Fall 1977, 868.

Because some students take more than one course, the number of individual students is slightly less than the number of class registrations. For example, in the Fall of 1977, 621 individuals made up the 868 class registrations shown. Of these, 538 (87%) were not APL staff members. The individuals were employed as follows:

Private industry	254
Government institutions	173
Educational institutions	71
Not employed or did not reply	40

It is evident that the Center is a substantial resource in the technical and educational community.

Eighty-four persons completed their programs and received master's degrees in 1977. Seven hundred and forty-seven APL Center students have received master's degrees. Of that number, 139 were APL staff members and 608 were not. These individuals constitute 72% of all those who received master of science degrees in technical areas from the various JHU Evening College centers during that time. The number of recipients in each area of specialization is:

Numerical Science	280
Electrical Engineering	271
Computer Science	137
Applied Physics	34
Space Technology	25

When the Center began operation, all courses were taken from the existing JHU curriculum. In Fiscal Year 1977, however, only 16% of the offerings were derived from that curriculum. In fact, most courses (62%) were originated and taught by APL staff members. Another 16% were created expressly for the Center by JHU faculty members of the Baltimore campus, and 6% were originated by Center instructors who are primarily employed by other organizations.

In our continuing effort to maintain the leadership that the APL Center has attained, we are constantly analyzing curricula and making revisions. In Fiscal Year 1977, APL Center instructors originated and taught six courses for the first time: Detection and Estimation Theory, Hardware Architecture of Digital Systems, Digital Simulation, Computer Systems Engineering Management Applications, Microprocessor Applications, and Fault Tolerant Digital Systems. Three new courses are planned for Fiscal Year 1978.

Figure 2 discloses that records were set in Fiscal Year 1977 for class roll totals, number of individuals enrolled, number of outside participants, number of participants from private industry, number of participants from Government facilities, and number of candidates for master's degrees offered at APL.

Although the physical facilities are modern and the audiovisual aids are excellent, the primary strength of the Center is its faculty. (Figure 3 shows a typical class.) Some full-time faculty members from the Baltimore campus instruct in this program, but 70% of the Center's faculty are members of the APL Senior

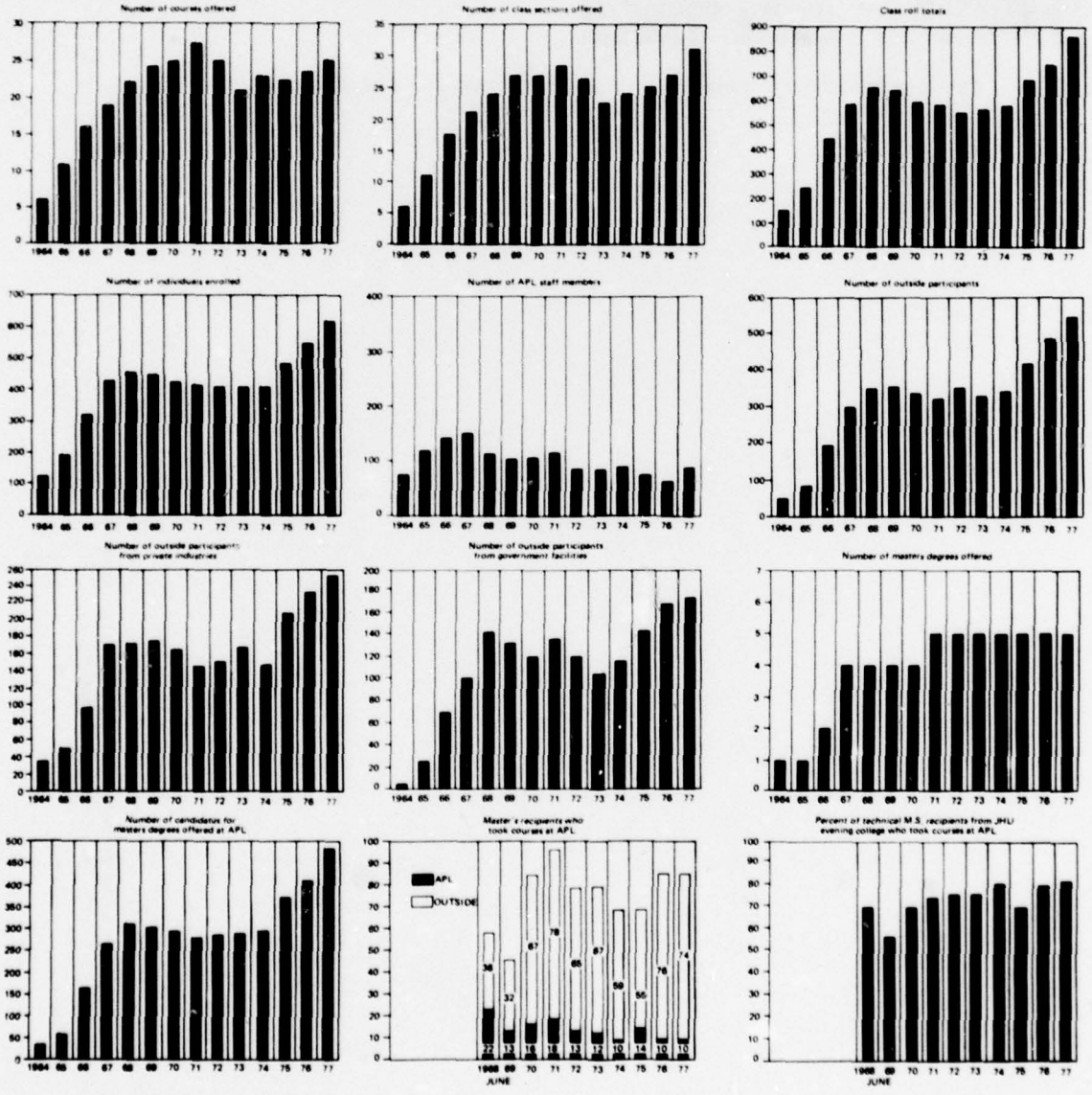

Fig. 2 Data on the APL Graduate Education Center.

Fig. 3 A typical class in session.

Staff and 15% are members of similar staffs of other scientific or engineering organizations. The students appreciate and appear to benefit from studying under academically qualified instructors who are actively involved with the subjects they teach and who understand the needs of part-time students who work in research and development organizations.

Author: P. B. Edwards

PATENTS

PATENTS ACTIVITIES

The APL Patents Office is responsible for ensuring compliance with contract and grant requirements relative to patent and data rights, as imposed by the various governmental agencies that sponsor work at the Laboratory. In addition to preparing formal disclosures of inventions for the appropriate sponsors, the Patents Office prepares and prosecutes patent applications on behalf of both the University and the Navy Department.

The following lists indicate the invention disclosures submitted to sponsors, the patent applications prepared and filed in the United States Patent Office, and the previously filed applications that were successfully prosecuted to issuance as patents, during Fiscal Year 1977.

INVENTION DISCLOSURES

Minimal Distortion Video Bandpass Filter
F. N. Sansone

Quick Release Hook
J. D. Steinberg

Trigger Circuit with Noise Controlled Adaptive Threshold for Detection of Tone-Burst Signals
J. H. Kuck

Circuit for Sorting Direct Path Signals from Reflected Signals
J. H. Kuck

Pattern Match Circuit
J. H. Kuck

Tone Burst Signal Detection System
J. H. Kuck

Submersible Non-Explosive Acoustic Generator (SNAG)
G. S. Bittings

Cell for Measurement of Passive Membrane Transport Coefficients
R. A. Meyer and M. H. Friedman

Oblique Folding Wing
R. M. Rivello and A. S. Polk

Velocimeter with Acoustical Sensor
G. S. Bittings and W. J. Eresian

Optical Detector
G. S. Bittings, W. J. Eresian, and R. E. Walker

Toroid Turns Tester
F. T. Marcellino

RF and IF Circuitry of an Uplink Receiver
R. C. Gipe

Bonding Agent for HMX
J. F. Kincaid and R. Reed

Low Level (Dry) Circuit Continuity Tester
F. T. Marcellino

Switching Voltage Regulator
D. Qualkinbush

Tape Recorder Sequencer
J. S. Lombardo

Programmable Tone Burst (PTB) Generator
S. R. Osborne

Planned View Display (PVD) Raster Scan Generator
S. R. Osborne

Fire Detector-Extinguisher
R. M. Fristrom

Programmable Mechanical Associative Processor
L. R. Gieszl

Clock Invariant Synchronization for Random Binary Sequences
C. Philippides

Harmonic, Digital Sine Generator
S. R. Osborne

Programmable Linear FM (LFM) Generator
S. R. Osborne

Thermistor Chain
G. S. Bittings

Time Transfer Receiver RF Circuitry
G. G. Whitworth

Digital AGC Amplifier
J. H. Kuck

Method of Fabricating Toroid Inductors and Transformers Using Toroidalgrams
J. F. Adams, Jr.

Code Converter
P. Klose and T. G. Calhoon

Method of Determining Sea Forces Acting on a Hovering Submarine
S. A. Fogel, W. F. Kujawa, I. D. Rapport, P. C. Smith, and J. J. Wosniak

Firing Control Circuit for Resistance Welder
F. T. Marcellino

Fire Atmosphere Badge Structure
R. M. Fristrom, D. Shapiro, and V. Esch

High-Speed, Glitch-Free, Digital-to-Analog Converter
P. J. Grunberger

Integral Rocket-Scramjet
J. L. Keirsey

Time Optimal Geomagnetic Spacecraft Maneuvering Technique
B. E. Tossman

Recovery of a Remotely Piloted Vehicle (RPV) Along a Kite Suspended Wire
M. L. Hill

Vertical Relative Landing of a Remotely Piloted Vehicle (RPV) Using Wire Terminal Guidance
M. L. Hill

Net Retrieval of a Remotely Piloted Vehicle (RPV)
M. L. Hill

War-At-Sea Graphical Analysis Model (WASGRAM) Game Including an Air Battle Package
T. P. Modelski, R. A. Freeman, and Jen-Yih Wang

Vacuum Probe for Water Pickup and Handling
J. L. Abita and H. K. Charles, Jr.

Miniature Probe Block
H. K. Charles, Jr.

Apparatus and Method for the Simultaneous Measurement of Passive Membrane Transport Properties
M. H. Friedman and R. A. Meyer

Sensor for Measuring Pitch and Yaw Angular Orientation Between a Spacecraft and an Attached Magnetometer
F. W. Schenkel and A. Finkel

Sensor for Measuring the Relative Twist Between a Spacecraft and an Attached Magnetometer by Means of a Dihedral Mirror
F. W. Schenkel and A. Finkel

Continuous Loop Flywheel
D. W. Rabenhorst

Apparatus for Identifying Missile Codes Without Internal Clock Synchronization
C. Philippides and W. H. Zinger

Missile Identification and Data Entry Apparatus
C. Philippides

Rotor Balancing Apparatus
D. W. Rabenhorst

Kite String Wound Flywheel Rotor
D. W. Rabenhorst

Laser Interferometric System
J. C. Murphy and R. C. Cole

Logarithmic Time Variable Gain Circuit
J. H. Kuck

No Pump Flow System
J. H. Panesci

Submarine Launched Expendable Flashing Buoy
G. S. Bittings

Laser Beam Folding Device
G. S. Bittings

Communication Line Switch
A. W. Currano

Natural Ice Collection Device and System
W. R. Powell

Spoked Multi-Ring Filament Rotor
D. W. Rabenhorst

Antenna Alignment Indicator
J. R. Butler

Weight Release Mechanism
R. A. Mattey and D. C. Wenstrand

High Density Digital Magnetic Recording Using a (5, 6) Alternating Disparity Block Code
M. Davidson and J. L. Machamer

Differential Screw Locking Mechanism for Finely Adjustable Optical Mount
R. H. Lapp

Cartridge Tape Formatter and Interface
T. G. Boland

Long-life Source for Thermal Vacuum Deposition
J. L. Abita and J. G. Bebee

PATENT APPLICATIONS

Human Tissue Stimulation Electrode Structure
R. E. Fischell

Epidural Lead Electrode and Insertion Needle
R. E. Fischell and W. R. Powell

Low Axial Force Servo Valve Spool
W. Seamone

Digital Beamsteering for a Parametric Scanning Sonar System
J. W. Follin and R. E. Miller

Pressure Responsive Switch
R. T. Cusick and W. J. Fleagle

Ionic Air Speed Indicator
M. L. Hill

Rechargeable Body Tissue Stimulator with Back-Up Battery and Pulse Generator
R. E. Fischell

Solar Panel Deployment Mechanism
L. E. Stillman and T. B. Coughlin

Photoacoustic Radiometer
J. C. Murphy and L. C. Aamodt

Single-Axis Disturbance Compensation System
R. E. Fischell, A. C. Sadilek, F. F. Mobley, and G. H. Fountain

Method for Correcting Navigation Errors Due to Water Currents
R. H. Bauer and M. C. Osborne

A Clock Invariant Synchronization Technique for Random Binary Sequence
C. Philippides

PATENTS ISSUED

No. 4,000,665
Woven Filament Rotor Structures
D. W. Rabenhorst

No. 4,001,728
Digital Method of Pulse Width Modulation
W. Schneider

No. 4,005,415
Automated Radar Data Processing System
A. Kossiakoff and J. R. Austin

No. 4,011,559
Universal Binary Code Converter
D. L. Sharp and E. A. Frekko

No. 4,011,564
Phase Modulated Monopulse System
J. F. Gulick

No. 4,016,560
Fractional Binary to Decimal Converter
R. W. Fowler

No. 4,019,032
X–Y to Range-Bearing Converter
E. J. McDevitt

No. 4,020,714
Filament Connected Rim Rotor
D. W. Rabenhorst

No. 4,023,437
Filament Rotor Having Elastic Sheaths Covering the Filamentary Elements of the Structure
D. W. Rabenhorst

No. 4,025,917
Simplified Time Code Reader with Digital PDM Decoder
J. M. DuBrul

No. 4,026,276
Intracranial Pressure Monitor
J. G. Chubbuck

No. 4,041,500
Line Scan Radar Antenna Using a Single Motor
R. H. Lapp

No. 4,042,933
Antenna Line Scan System for Helicopter Wire Detection
R. H. Lapp

No. 4,047,170
Monotrack Radar Recording/Playback System
R. E. Miller

No. 4,048,569
Carrier-Modulated Coherency Monitoring System
E. F. Osborne

No. 4,050,533
Powered Wheelchair
W. Seamone

No. 4,065,771
Random Scanning Receiver
J. F. Gulick and D. R. Marlow

PUBLICATIONS AND PRESENTATIONS

PUBLICATIONS

L. C. Aamodt, J. C. Murphy, and J. G. Parker, "Size Considerations in the Design of Cells for Photoacoustic Spectroscopy," *J. Appl. Phys.* **48**, No. 3, Mar 1977, pp. 927–933.

R. C. Adams (APL) and J. M. Cohen (Univ. of Pennsylvania, Philadelphia), "Analytic Supernova Models and Black Holes," *Int. J. Theoret. Phys.* **16**, No. 1, 1977, pp. 35–52.

F. J. Adrian and V. A. Bowers, "ESR Spectrum of XeCl in Argon at 4.2K," *J. Chem. Phys.* **65**, No. 10, 1976, pp. 4316–4318.

A. Arnold, "A Lapse Rate Depiction for Clear-Air Convection," *J. Appl. Meteorol.* **15**, No. 11, 1976, pp. 1189–1192.

———, "Observations of Development of Individual Clear Air Convective Cells," *AMS 17th Conf. on Radar Meteorology*, 1976, pp. 338–341.

———, and J. R. Rowland, "Fine Scale Observations of Free Convection in the Atmospheric Boundary Layer," *AMS Third Symp. on Atmospheric Turbulence, Diffusion and Air Quality*, 1976, pp. 1–8.

C. B. Bargeron and R. B. Givens, "Source of Oscillations in the Anode Current during the Potentiostatic Pitting of Aluminum," *J. Electrochem. Soc.* **124**, No. 8, Aug 1977, pp. 1230–1232.

R. J. Bartlett (Battelle Memorial Institute) and D. M. Silver (APL), "Numerical Infinite-Order Perturbation Theory," *Quantum Science*, J.-L. Calais, O. Goscinski, J. Linderberg, and Y. Ohrm (eds.), Plenum Press, New York, 1976, pp. 393–408.

R. C. Benson, "Sodium chemiluminescence in the Na + N_2O and Na-catalyzed N_2O+CO reactions," *J. Chem. Phys.* **66**, No. 9, 1 May 1977, pp. 3879–3885.

H. D. Black, R. E. Jenkins, and L. L. Pryor, *The Transit System, 1975*, APL/JHU TG 1305, Dec 1976.

B. I. Blum, "Training Engineers to Work in the Clinical Setting," *Proc. 23rd Annual Meeting of the Institute of Environmental Sciences*, Los Angeles, 23–27 Apr 1977.

——— and R. E. Lenhard, Jr. (JHMI), "A Prototype Clinical Patient Management System," *Proc. Washington ACM Technical Symp.*, 2 Jan 1977.

N. A. Blum, C. Feldman, and F. G. Satkiewicz, "Infrared Absorption of Amorphous Boron Films Containing Carbon and Hydrogen," *Phys. Status Solidi* **41**, Jun 1977, pp. 481–486.

J. Bohandy and B. F. Kim, "An Electron Spin Resonance Study of Copper Porphin," *J. Magn. Reson.* **26**, 1977, pp. 341–349.

P. F. Bohn, R. J. Keenan, and J. Prowznik, *Hybrid Computer Vehicle Handling Program*, APL/JHU CP 049, Sep 1977.

C. A. Boyles, "Theory of the spherical, compliant-tube Luneburg lens," *J. Acoust. Soc. Am.* **61**, No. 2, Feb. 1977, pp. 338–352.

S. J. Brown, Jr., *Point-Follower Automatic Vehicle Control: A Generic Analysis*, APL/JHU CP 057/TPR 025, May 1977.

F. R. Castella, "Sliding Window Detection Probabilities," *IEEE Trans. Aerosp. Electron. Syst.*, Nov 1976, pp. 815–819.

H. K. Charles, Jr., C. Feldman, and F. G. Satkiewicz, "p–n Junctions in Vacuum Deposited Polycrystalline Silicon Thin Films," *Technical Digest 1976 International Electron Devices Meeting*, 1976, pp. 71–74.

H. Y. Chiu, G. B. Stupp, Jr., and S. J. Brown, Jr., *Vehicle Follower Controls for Short Headway AGT Systems—Functional Analysis and Conceptual Designs*, APL/JHU CP 051/TPR 035, Dec 1976.

———, ———, and ———, "Vehicle-Follower Control with Variable-Gains for Short Headway Automated Guideway Transit Systems," *J. Dyn. Syst. Meas. Control* **99**, Sep 1977, pp. 183–189.

T. D. Cradduck (Ontario Cancer Foundation, Victoria Hospital) and L. G. Knowles (APL), "Computers in Nuclear Medicine," *Nuclear Medicine Physics, Instrumentation and Agents*, F. D. Rollo (ed.), C. V. Mosby Co., St. Louis, 1977.

E. B. Dobson (APL) and J. E. Kalshoven, Jr. (NASA Goddard), "The Evaluation of Satellite-Borne Weather Radar System Designs Using Real Ground-Based Radar Data," *AMS Seventh Conf. on Aerospace and Aeronautical Meteorology and Symp. on Remote Sensing from Satellites*, 1976, pp. 253–259.

DoD Weapon Systems Software Management Study, Appendix A, Findings and Recommendations of Previous Studies, APL/JHU SR 75-3A, Jun 1975; also *Appendix B, Shipborne Systems*, APL/JHU SR 75-3B, Jun 1975.

J. P. Doering and W. K. Peterson (The Johns Hopkins Univ.) and T. A. Potemra and C. O. Bostrom (APL), "Characteristic Energy Spectra of 1– to 500–eV Electrons Observed in the High-Latitude Ionosphere from Atmosphere Explorer C," *J. Geophys. Res.* **81**, No. 31, 1976.

G. L. Dugger, "Ocean Thermal Energy Conversion," *Energy Technology Handbook*, D. M. Considine (ed.), 1977, pp. 6–118 to 6–136.

———, H. L. Olsen, P. P. Pandolfini, and W. H. Avery, "Experiments on and Design of Low-Cost Aluminum Heat Exchangers for OTEC Plant Ships," *Proc. Fourth Annual Conference on Ocean Thermal Energy Conversion, OTEC*, New Orleans, 22–24 Mar 1977, pp. VI–111 to VI–123.

C. R. Edwards, R. C. Moore, and G. E. Baer, *St. Marys River COGLAD Navigation System Final Report*, APL/JHU CP 053, Feb 1977.

L. W. Ehrlich and M. H. Friedman, "Particle Paths and Stasis in Unsteady Flow Through a Bifurcation," *J. Biomech.* **10**, 1977, pp. 561–568.

——— and ———, "Steady Convective Diffusion in a Bifurcation," *IEEE Trans. Biomed. Eng.* **BME24**, No. 1, Jan 1977, pp. 12–18.

——— and V. O'Brien, "Forced Convection Within Straight Noncircular Ducts," *Trans. ASME* **99**, No. 3, Aug 1977, p. 485.

A. Elcrat (Wichita State Univ.) and V. G. Sigillito (APL), "An Explicit *a priori* Estimate for Parabolic Equations with Applications to Semilinear Equations," *SIAM J. Math. Anal.* 7, No. 5, 1976, pp. 746–753.

L. F. Fehlner, T. W. Jerardi, T. A. McCarty, and R. G. Roll, *Experimental Research on the Propagation of Loran-C Signals, Vol. A: Summary Report,* APL/JHU TG 1298A, Oct 1976; also *Vol. D: Data and Analysis,* APL/JHU TG 1298D, Jan 1977.

C. Feldman, F. G. Satkiewicz, and H. K. Charles, Jr., "Evaluation of Vacuum Deposited Silicon Films and Junctions for Solar Cell Applications," *Proc. National Workshop on Low-Cost Polycrystalline Silicon Solar Cells,* Dallas, Dec 1976, p. 267.

R. W. Flower, "A System for *in vivo* Measurement of Oxygen in Intraocular Tissue," *Oxygen Transport to Tissue—II,* J. Grote, D. Reneau, and G. Thews (eds.), Plenum Press, New York, 1977, p. 417.

———, "Simple adaptors for fast conversion of a fundus camera for rapid-sequence ICG fluorescence choroidal angiography," *J. Biol. Photogr. Assoc.* 45, No. 2, Apr 1977, pp. 43–47.

——— and B. F. Hochheimer, "Quantification of Indicator Dye Concentration in Ocular Blood Vessels," *Exp. Eye Res.* 25, 1977, p. 103.

——— and P. Speros and K. R. Kenyon (JHMI), "Electroretinographic Changes and Choroidal Defects in a Case of Central Retinal Artery Occulsion," *Am. J. Ophthalmol.* 83, No. 4, Apr 1977, pp. 451–459.

J. W. Follin, Jr., and K. Yu, "Use of ELF Measurements to Supplement VLF and Magneto Telluric Signals in Electromagnetic Prospecting," *Trans. Geotherm. Resour. Coun.* 1, May 1977, pp. 97–98.

D. W. Fox and J. T. Stadter, "An Eigenvalue Estimation of Weinberger and Weinstein's Intermediate Problems," *SIAM J. Math. Anal.* 8, No. 3, May 1977, p. 491.

E. J. Francis (APL) and J. Seelinger (U.S. Maritime Administration), "Forecast Markets, Economics and Shipbuilding Program for OTEC Industrial Plant-Ships in Tropical Oceans," *Proc. of A Solar World and A Solar Market, International Solar Energy Society Meeting,* Orlando, FL, 6–10 Jun 1977.

——— and ———, "Market Definition, Commercial Development Plan, and OTEC Financing: A Summary of 1976 APL Work for the U.S. Maritime Administration," *Proc. Fourth Annual Conference on Ocean Thermal Energy Conversion, OTEC,* New Orleans, 22–24 Mar 1977, pp. III–58 to III–66.

S. K. Ghatak (Institute for Theoretical Physics, Berlin) and K. Moorjani (APL), "Equivalence Between the Edwards-Anderson and Luttinger Models of a Spin Glass," *Solid State Commun.* 23, Aug 1977, pp. 399–400.

J. Goldhirsh, "Attenuation of Propagation Through Rain for an Earth-Satellite Path Correlated with Predicted Values Using Radar," *IEEE Trans. Antennas Propag.* AP–24, No. 6, 1976, pp. 800–806.

———, "Path Attenuation Statistics Influenced by Orientation of Rain Cells," *IEEE Trans. Antennas Propag.* AP–24, No. 6, 1976, pp. 792–799.

E. P. Gray, R. W. Hart, and R. A. Farrell, "A New Variational Approach to Scattering by Random Media or Rough Surfaces," *Proc. Open Colloq., Commission F, URSI,* 28 Apr–6 May 1977, pp. 111–116.

S. Green (NASA Institute of Space Studies), L. Monchick (APL), and R. Goldflamm and F. Kouri (Univ. of Houston), "Configurational Tests of Angular Momentum Decoupling Approximation for Pressure Broadening Cross Sections," *J. Chem. Phys.* 66, No. 4, 15 Feb 1977, p. 1409.

R. W. Hart (ed.), *Indirectly Funded Research and Exploratory Development at the Applied Physics Laboratory, Fiscal Year 1975,* APL/JHU SR 76–2, Jun 1976.

——— and R. A. Farrell, "A Variational Principle for Scattering from Rough Surfaces," *IEEE Trans. Antennas Propag.* AP–25, No. 5, Sep 1977, pp. 708–710.

P. L. Hazan, "March of the Microprocessors," *Johns Hopkins Mag.,* Nov 1976, pp. 9–15.

B. F. Hochheimer, "Radiation pattern for a diffuse wall cavity, nonuniform in temperature and emissivity," *Appl. Opt.* 16, No. 8, Aug 1977, pp. 2038–2039.

——— and J. L. Calkins (JHMI), "The Integrated Radiance of Flashbulbs," *Opt. Eng.* 16, No. 2, Mar–Apr 1977, pp. 212–213.

B. B. Holland, A. Eisner, and S. M. Yionoulis, *The Effect of WGS–72 Geopotential in the Navy Navigation Satellite System on Station Surveys,* APL/JHU TG 1311, Aug 1977.

L. W. Horowitz, *Analysis of a Single-Bit Digital Receiver for Carrier and Code Tracking,* APL/JHU TG 1283, Jul 1976.

L. W. Hunter, H. Schacke, C. Grunfelder, and R. M. Fristrom, "Surface Temperature Measurements in the Moving Wire Technique," *Combust. Sci. Tech.* 15, Jan 1977, pp. 41–48.

T. Iijima and T. A. Potemra, "Field-Aligned Currents in the Dayside Cusp Observed by Triad," *J. Geophys. Res.* 81, No. 34, 1976, pp. 5971–5979.

E. P. Irzinski, "The input admittance and near-field coupling of a TEM-driven concentric annular slot array," *Radio Sci.* 12, No. 2, Mar-Apr 1977, pp. 213–222.

E. C. Jarrell, D. R. Marlow, and H. B. Tetens, *Target Seeker Simulator Developed for Five-Inch ASMD Missile Flight Tests,* APL/JHU TG 1302, Sep 1976.

R. E. Jenkins and A. D. Goldfinger, *High-Resolution Clock Control for the TIP Satellite,* APL/JHU TG 1301, Sep 1976.

A. N. Jette, "The *ab initio* calculation of the spin-rotational coupling in the metastable $c^3\Pi_u$ (1s,2p) state of molecular hydrogen," *J. Chem. Phys.* 65, No. 10, 1976, pp. 4325–4327.

——— and F. J. Adrian, "Theoretical Investigation of the Hyperfine-Structure Constants of the V_K and $(XY)^-$ Centers Using a Valence-Bond Wave Function for the Halogen-Molecule Anions," *Phys. Rev. B* 14, No. 8, 1976, pp. 3672–3681.

C. J. Johns (JHMI), D. W. Simborg (Univ. of California, San Francisco), B. I. Blum (APL), and B. H. Starfield (JHMI), "A Minirecord: An Aid to Continuity of Care," *Johns Hopkins Med. J.* 140, Jun 1977, pp. 277–284.

R. I. Joseph (The Johns Hopkins Univ.) and R. A. Farrell (APL), "High-Temperature Series for the Spin-One

Ising Model for Arbitrary Biquadratic Exchange Field and Anisotropy," *Phys. Rev. B* **14**, No. 11, 1976, pp. 5121–5124.

S. W. Kahng, *Macro Instructions and Their Processor for Structured Programming with Assembly Languages*, APL/JHU TG 1308, Jun 1977.

J. E. Kain (Analytical Sciences Corp., Reading, MA) and D. J. Yost (APL), "Command to Line-of-Sight Guidance: A Stochastic Optimal Control Problem," *J. Spacecr. Rockets* **14**, No. 7, Jul 1977, pp. 438–444.

I. Katz, "A Rain Cell Model," *AMS 17th Conf. on Radar Meteorology*, 1976, pp. 442–447.

G. S. Keys and B. F. Hochheimer, "The Design of a Simple Fluorometer for Underwater Detection of Rhodamine Dye," *Sea Tech.* **18**, No. 9, Sep 1977, pp. 24–28.

B. F. Kim and J. Bohandy, "Single Site Spectra of Zn Porphin in Triphenylene," *J. Mol. Spectrosc.* **65**, 1977, pp. 90–101.

E. Kirsch and S. M. Krimigis (APL), E. T. Sarris (Max-Planck Institute), R. P. Lepping (NASA Goddard), and T. P. Armstrong (Univ. of Kansas), "Possible Evidence for Large, Transient Electric Fields in the Magnetotail from Oppositely Directed Anisotropies of Energetic Protons and Electrons," *Geophys. Res. Lett.* **4**, No. 4, Apr 1977, pp. 137–140.

W. C. Klingensmith III (Johns Hopkins School of Medicine), M. G. Lotter (Univ. of Orange Free State, Republic of South Africa), L. G. Knowles (APL), and A. Motazedi and H. N. Wagner, Jr. (Johns Hopkins School of Medicine) "Physiological Interpretation of Time-Activity Curves from Cerebral Flow Studies," *Proc. Symp. Computer-Assisted Data Procesing in Nuclear Medicine*, Atlanta, 16–17 Jan 1977, ERDA Conf. 770101.

L. G. Knowles, "Book Review of *Holography in Medicine*," *J. Nucl. Med.* **18**, 1977, p. 502.

T. G. Konrad, *Statistical Models of Summer Rain Showers Derived from Fine-Scale Radar Observations*, APL/JHU CP 056, Apr 1977.

H. A. Kues and C. E. Teague, "Thin-Layer Chromatography of Some Cyanine Dyes," *J. Chromatogr.* **135**, 1977, pp. 221–225.

T. R. Larsen (Norwegian Defence Research Establishment), T. A. Potemra (APL), and W. L. Imhof and J. B. Reagan (Lockheed Palo Alto Research Laboratory), "Energetic Electron Precipitation and VLF Phase Disturbances at Middle Latitudes Following the Magnetic Storm of December 16, 1971," *J. Geophys. Res.* **82**, No. 10, 1 Apr 1977, p. 1519.

C. S. Leffel, Jr., and R. A. Eisenberg, *Geothermal Handbook*, APL/JHU SR 77-1, Jun 1977.

——— and C. A. Wingate (APL) and C. Balas (Philips Laboratories, Briarcliff Manor, NY), "Performance of a Stirling Cycle Cryogenic Refrigerator for Spacecraft," *Proc. 25th National IRIS*, San Francisco, 14–16 Jun 1977.

M. G. Lotter (Univ. of Orange Free State, Republic of South Africa), K. H. Douglass (Johns Hopkins School of Medicine), L. G. Knowles (APL) and E. L. Nickoloff and H. N. Wagner, Jr. (Johns Hopkins School of Medicine), "A Technique for the Evaluation of Global and Regional Ventricular Function," *Proc. Symp. Computer-Assisted Data Processing in Nuclear Medicine*, Atlanta, 16–17 Jan 1977, ERDA Conf. 770101.

E. F. Lucero, "Subsonic Stability and Control Characteristics of Configurations Incorporating Wrap-Around Surfaces," *J. Spacecr. Rockets* **13**, No. 12, 1976, pp. 740–745.

A. I. Mahan (APL) and H. Osterberg (American Optical Co., Southbridge, MA) "Diffraction Properties of Absorbing Cylinders Suspended in Outside Absorbing Media," *Opt. Acta* **24**, No. 9, 1977, pp. 949–963.

J. H. Manley, *Encyclopedia of Computer Science and Technology* 5, J. Belzer, A. G. Holzman, and A. Kent (eds.), Marcel-Dekker, Inc., New York, 1976, pp. 174–186.

———, "Management Discipline, An Essential Ingredient for Reliable Software," *Proc. NSIA Conf., Software Quality-Reliability*, Arlington, VA, 30 Mar 1977.

F. F. Mark, C. B. Bargeron, O. J. Deters, and M. H. Friedman, "Experimental Investigations of Steady and Pulsatile Laminar Flow in a 90° Branch," *Trans. ASME* **44**, No. 3, Sep 1977, pp. 372–377.

R. L. McCally and R. A. Farrell, "Effect of Transcorneal Pressure on Small Angle Light Scattering from Rabbit Cornea," *Polymer* **18**, No. 5, May 1977, pp. 444–448.

R. A. Meyer, "Light Scattering from Red Blood Cell Ghosts: Sensitivity of Angular Dependent Structure to Membrane Thickness and Refractive Index," *Appl. Opt.* **16**, No. 8, Aug 1977, pp. 2036–2038.

D. G. Mitchell (Univ. of New Hampshire) and E. C. Roelof (APL), "A Mathematical Analysis of the Theory of Interplanetary Scintillation in the Weak Scattering Approximation," *J. Geophys. Res.* **81**, No. 28, 1976, pp. 5071–5082.

T. P. Modelski, R. A. Freeman, and J. Wang, *Computerized Air Battle Using Interactive Graphics Techniques*, APL/JHU TG 1306, Apr 1977.

L. Monchick, and L. W. Hunter, "A Kinetic Theory of Quantum State Diffusion," *J. Chem. Phys.* **66**, No. 9, 1 May 1977, pp. 4141–4148.

——— and S. Green (NASA Institute of Space Studies), "Validity of Approximate Methods in Molecular Scattering. III. Effective Potential and Coupled States Approximations for Differential and Gas Kinetic Cross Sections," *J. Chem. Phys.* **66**, 1 Apr 1977, p. 3085.

——— and L. A. Viehland, E. A. Mason, and T. H. Stevens (Brown Univ.), "Test of the H_2^+ + He Interaction Potential, Comparison of the Interactions of He with H^+, H_2^+ and H_3^+," *Chem. Phys. Lett.* **44**, No. 2, Dec 1976, pp. 360–362.

K. Moorjani and C. Feldman, "V. Amorphous Boron Films," *Boron and Refractory Borides*, V. I. Matkovich (ed.), Springer-Verlag, Berlin, 1977.

——— and S. K. Ghatak (Institute for Theoretical Physics), "Critical Behavior of a Structurally and Chemically Disordered Ferromagnet," *J. Phys. C.* **10**, Apr 1977, pp. 1027–1038.

J. C. Murphy and L. C. Aamodt, "Photoacoustic Spectroscopy of Luminescent Solids: Ruby," *J. Appl. Phys.* **48**, No. 8, 1977, pp. 3502–3509.

B. H. Nall, "Use of a hot wire anemometer as a particle velocity detector in standing sound waves," *Rev. Sci. Instrum.* **48**, No. 4, Apr 1977, pp. 449–453.

R. R. Newton, *A Canon of Lunar Eclipses for the Years −1500 to −1000*, APL/JHU CP 054, Feb 1977.

J. T. Nolte and A. S. Krieger (American Science and Engineering) and E. C. Roelof and R. E. Gold (APL), "High Coronal Structure of High Velocity Solar Wind Stream Sources," *Sol. Phys.* **51**, 1977, pp. 459–471.

———— and E. C. Roelof (APL), "Solar Wind, Energetic Particles, and Coronal Magnetic Structure: The First Year of Solar Cycle 20," *J. Geophys. Res.* **82**, No. 16, 1 Jun 1977, pp. 2175–2186.

R. B. North (APL), T. A. Fischell (Cornell Univ.), R. E. Fischell (APL), and D. M. Long (Johns Hopkins Hospital), *A Clinical Study of Spinal Epidural Stimulation for the Treatment of Intractable Pain*, APL/JHU CP 052, Mar 1977.

V. O'Brien, "Analytic description of steady separation from curved surfaces," *Phys. Fluids* **20**, No. 7, Jul 1977, pp. 1045–1049.

————, *Developed Convective Thermal Fields in Noncircular Ducts*, APL/JHU TG 1303, Sep 1976.

————, "Steady and Unsteady Flow in Noncircular Straight Ducts," *J. Appl. Mech.* **44**, No. 1, Mar 1977, pp. 1–6.

———— and L. W. Ehrlich, "Pulsatile Flow Through Stenosed Arteries," *Proc. ASME–AMD 1977 Biomechanics Symp.* **23**, 1977, pp. 113–116.

D. E. Olsen, "Estimating Reliability Growth," *IEEE Trans. Reliab.* **R–26**, No. 1, Apr 1977, pp. 50–53.

P. P. Pandolfini, H. L. Olsen, and R. A. Makofski, "Two-Phase Flow Heat Transfer in Large Diameter Tubes for OTEC," *Proc. of Condensed Papers, Two-Phase Flow and Heat Transfer Symposium-Workshop*, Ft. Lauderale, FL, 18–20 Oct 1976, pp. 265–268.

W. K. Peterson and J. P. Doering (The Johns Hopkins Univ.), T. A. Potemra and C. O. Bostrom (APL), L. H. Brace (NASA Goddard), and R. A. Heelis and W. B. Hanson (Univ. of Texas, Dallas), "Measurement of Magnetic Field Aligned Potential Differences Using High Resolution Conjugate Photoelectron Energy Spectra," *Geophys. Res. Lett.* **4**, No. 9, Sep 1977, pp. 373–376.

————, ————, ————, R. W. McEntire, and C. O. Bostrom (APL), "Conjugate Photoelectron Fluxes Observed on Atmosphere Explorer C," *Geophys. Res. Lett.* **4**, No. 3, Mar 1977, p. 109.

————, ————, ————, ————, ————, R. A. Hoffman and R. W. Janetzke (NASA Goddard), and J. L. Burch (NASA Marshall), "Observations of 10-eV to 25-keV Electrons in Steady Diffuse Aurora From Atmosphere Explorer C and D," *J. Geophys. Res.* **82**, No. 1, 1 Jan 1977, p. 43.

V. L. Pisacane and J. L. MacArthur, *A Lunar Polar Orbiter Subsatellite Tracking Experiment*, APL/JHU CP 048, Oct 1976.

K. T. Plesser (APL) and T. O. Field (ARINC Research, Annapolis, MD), "Cost-Optimized Burn-In Duration for Repairable Electronic Systems," *IEEE Trans. Reliab.* **R–26**, No. 3, Aug 1977, pp. 195–197.

T. O. Poehler (APL) with A. N. Bloch, D. O. Cowan, and T. Carruthers (The Johns Hopkins Univ.), "The Organic Metallic State: Chemical Aspects; Some Physical Aspects and Chemical Trends," *Proceedings of the NATO Conference on Physics and Chemistry of One-Dimensional Metals*, H. J. Keller (ed.), Plenum Press, New York, 1977.

P. R. Popick, *A Case Study of a Program Library Technique*, APL/JHU TG 1310, May 1977.

T. A. Potemra, "Aurora borealis, the greatest light show on Earth, may help explain climatic changes, the ozone shield," *Smithsonian* **7**, No. 11, Feb 1977, pp. 64–73.

A. J. Pue, *A State-Constrained Approach to Vehicle-Follower Control for Short-Headway AGT Systems*, APL/JHU CP 058/TPR 038, Aug 1977.

————, "A State Constrained Approach to Vehicle Follower Control for Short Headway Automated Transit Systems," *Proc. 1977 Joint Automatic Control Conf.*, San Francisco, 22–24 Jun 1977, pp. 401–407.

R. C. Rand and W. Avery, "Applications of New Systems to Urban Transportation," *Traffic Q.*, Jan 1977, pp. 97–117.

J. C. W. Rogers, *An Algorithm for a Hyperbolic Free Boundary Problem*, APL/JHU TG 1309, May 1977.

————, *Some Exact Hydrodynamic Flows with Free Surfaces*, APL/JHU TG 1307, Apr 1977.

J. M. Ross, "Sea Spider: An Ocean-Floor Oil Wellhead Monitoring and Maintenance System," *MTS J.* **10**, No. 8, 1976, pp. 26–31.

J. R. Rowland, "Comparison of Two Different Raindrop Disdrometers," *AMS 17th Conf. on Radar Meteorology*, 1976, pp. 398–405.

H. Schacke, L. W. Hunter, R. M. Fristrom, and C. Grunfelder, "Combustion of Poly(vinyl chloride) Studied by the Moving Wire Technique," *Sixteenth Symp. (International) on Combustion*, The Combustion Institute, Sep 1977, pp. 1317–1327.

F. W. Schenkel and A. Finkel, *The APL MAGSAT Attitude Transfer System Concept*, APL/JHU CP 055, Apr 1977.

V. G. Sigillito, *Explicit a priori Inequalities with Applications to Boundary Value Problems*, Pittman Pub. Ltd., Belmont, CA, Jul 1977.

D. M. Silver and S. Wilson (APL) and R. J. Bartlett (Battelle Memorial Institute), "Modified Potentials in Many-Body Perturbation Theory: Three-Body and Four-Body Contributions," *Phys. Rev. A* **16**, No. 2, Aug 1977, pp. 477–483.

P. C. Smith, S. A. Fogel, and I. D. Rapport, "Deterministic Estimation of Sea Forces Acting on a Hovering Submarine," *Proc. 1977 Summer Computer Simulation Conf.*, Chicago, Jul 1977, pp. 325–332.

J. T. Stadter and R. O. Weiss, "A New Method for Analyzing Structural Contact Problems," *Proc. Sixth Canadian Congress of Applied Mechanics*, 29 May—3 Jun 1977, Vancouver, B. C., pp. 1017–1018.

W. D. Stanbro, "The Chemistry of Amino Acids and Peptides in Power Plant Cooling Towers," *Chesapeake Sci.* **18**, No. 1, Mar 1977, pp. 126–128.

A. C. Stucki, "What Goes Up Must Come Down," *Build. Oper. Manage.*, Mar 1977, p. 16.

I. Sugai, "Partial Differentiations of Vis-Viva and Lambert

Equations," *J. Astronaut. Sci.* **XXV**, No. 1, Jan–Mar 1977, pp. 63–74.

———, "Problem 76–4, Geometric Probability," *SIAM Rev.* **19**, No. 1, Jan 1977, pp. 152–154.

R. J. Taylor and W. J. Toth, "Ammonia Absorption Geothermal District Heating and Air-Conditioning System," *Trans. Geotherm. Resour. Coun.* **1**, May 1977, pp. 287–288.

A. A. Westenberg and N. deHaas, "A flash photolysis-resonance fluorescence study of the $O+C_2H_2$ and $O+C_2H_3Cl$ reactions," *J. Chem. Phys.* **66**, No. 11, 1 Jun 1977, pp. 4900–4905.

——— and ———, "Rates of $H+CF_3Br$ and $Cl+NH_3$," *J. Chem. Phys.* **67**, 1977, pp. 2388–2390.

S. Wilson and D. M. Silver, "Algebraic Approximation in Many-Body Perturbation Theory," *Phys. Rev. A* **14**, No. 6, 1976, pp. 1949–1960.

——— and ———, "Diagrammatic perturbation theory: many-body effects in the $X^1\Sigma^+$ of first-row and second-row diatomic hydrides," *J. Chem. Phys.* **66**, No. 12, 15 Jun 1977, pp. 5400–5411.

——— and ———, "Diagrammatic perturbation theory: $N_2X^1\Sigma^+g$," *J. Chem. Phys.* **67**, No. 4, 15 Aug 1977, pp. 1689–1697.

——— and ———, and R. J. Bartlett (Battelle Memorial Institute), "Many-body effects in the $X^1\Sigma$ states of the hydrogen fluoride, lithium fluoride and boron fluoride molecules," *Molec. Phys.* **33**, No. 4, 1977, pp. 1171–1193.

PRESENTATIONS

F. J. Adrian, "Basic Diffusion Processes," NATO Advanced Study Institute on Chemically Induced Magnetic Polarization, Urbino, Italy, 17–30 Apr 1977.

———, "Chemically Induced Magnetic Polarization: A Semipermanent Record of a Rapid Free Radical Reaction," Argonne National Laboratory Chemistry Division, Argonne, IL, 17 Mar 1977. Also presented to Univ. of Chicago Chemistry Department, Chicago, 18 Mar 1977.

———, "Electron Polarization and CIDNP," NATO Advanced Study Institute on Chemically Induced Magnetic Polarization, Urbino, Italy, 17–30 Apr 1977.

———, "Radical Pairs Concepts: Qualitative Aspects," NATO Advanced Study Institute on Chemically Induced Magnetic Polarization, Urbino, Italy, 17–30 Apr 1977.

———, "Radical Pairs Concepts: Quantitative Theory," NATO Advanced Study Institute on Chemically Induced Magnetic Polarization, Urbino, Italy, 17–30 Apr 1977.

——— and A. N. Jette, "Hyperfine Interactions and Structure of the Noble Gas Monohalides," VI International Symp. on Magnetic Resonance, Banff, Canada, 21–27 May 1977.

T. P. Armstrong and G. Chen (Univ. of Kansas), E. T. Sarris (Max-Planck Institute), and S. M. Krimigis (APL), "Acceleration and Modulation of Electrons and Ions by Propagating Interplanetary Shocks," XXth COSPAR Meeting, Tel Aviv, 7–18 Jun 1977.

C. Balas (Philips Laboratories, Briarcliff Manor, NY) and C. S. Leffel and C. A. Wingate (APL), "The Stirling Cycle Cooler: Approaching One Year of Maintenance-Free Life," Cryogenic Engineering Conf., Boulder, CO, 2–5 Aug 1977.

E. R. Bernheisel, "The Writing Process as a Design Tool," 24th International Technical Communication Conf., Chicago, 11–14 May 1977.

B. I. Blum, "Low-Cost Mixed-Media Picture Data Retrieval," Workshop on Picture Data Description and Management, Chicago, 20–22 Apr 1977.

——— and K. E. Richeson, "Inexpensive Computer Assisted Software Engineering for Moderate Sized Programs," Spring COMPCON 77, San Francisco, 1–3 Mar 1977.

J. Bohandy, "EPR of Iron Porphin in Triphenylene," VI International Symp. on Magnetic Resonance, Banff, Canada, 21–27 May 1977.

H. K. Charles, Jr., C. Feldman, F. G. Satkiewicz, and N. A. Blum, "Evaporated Polycrystalline Silicon Films for Photovoltaic Applications—Grain Size Effects," Nineteenth Electronic Materials Conf., Ithaca, NY, 1 Jul 1977.

L. W. Ehrlich, "Applications to Fluid Problems," Applied Matrix Computations Meeting, Baltimore, 18 Aug 1977.

F. T. Erskine (Univ. of Maryland), W. M. Cronyn and S. D. Shawhan (Univ. of Iowa), and E. C. Roelof and B. L. Gotwols (APL), "Interplanetary Scintillation at Large Elongation Angles: Response to Solar Wind Density Structure," American Geophysical Union Meeting, San Francisco, 6–10 Dec 1976.

R. A. Farrell, "Collagen Organization in Corneal Transparency," Macromolecular Science Colloq., Case Western Reserve Univ., Cleveland, 22 Oct 1976.

C. Feldman, "Polycrystalline Silicon Solar Cells," Indian Institute of Technology Meeting, Kanpur, India, 8–9 Nov 1976.

D. W. Fox, "An Error Estimate for Definite Relative Eigenvalue Problems," Math-Sciences Department Seminar, The Johns Hopkins Univ., Baltimore, 18 Nov 1976.

———, "Bounds for Perturbation Eigenvalues of Relative Matrix Problems," American Mathematical Society, Evanston, IL, 15 Apr 1977. Also presented at Department of Applied Mathematics Colloq., Northwestern Univ., Evanston, IL, 13 Apr 1977.

———, "The Convexity of the Graph of Three Hermitian Forms and the Numerical of Sesquilinear Forms," Math-Sciences Department Seminar, The Johns Hopkins Univ., Baltimore, 9 Dec 1976.

———, "The Convexity of the Range of Three Hermitian Forms," American Mathematical Society Summer Meeting, Seattle, 17 Aug 1977.

———, "Rayleigh-Ritz Bounds for Eigenvalues on the Wrong Side," Math-Sciences Department Seminar, The Johns Hopkins Univ., Baltimore, 28 Apr 1977.

M. H. Friedman, "Analysis of Ion Transport Across and Electrical Properties of Rabbit Corneal Epithelium,"

Association for Research in Vision and Ophthalmology, Sarasota, FL, 25–29 Apr 1977.

R. E. Gold, B. L. Gotwols, S. M. Krimigis, and E. C. Roelof, "Propagation of Relativistic Jovian Electrons to Earth and to Pioneer 10," American Geophysical Union Meeting, San Francisco, 6–10 Dec 1976.

———, E. P. Keath, and E. C. Roelof (APL) and R. Reinhard (European Space and Technology Research Center, The Netherlands), "Coronal Structure of the April 10, 1969 Solar Flare Particle Event," 15th International Cosmic Ray Conf., Plovdiv, Bulgaria, 13–26 Aug 1977.

R. E. Gold, S. M. Krimigis, and E. C. Roelof, "Spatially Dominated Solar Particle Events, 1972–1976," 15th International Cosmic Ray Conf., Plovdiv, Bulgaria, 13–26 Aug 1977.

———, ———, and ——— (APL) and R. W. Fillius (Univ. of California, San Diego), "The Relationship Between Jovian Electrons and Solar Wind Stream Structure," 15th International Cosmic Ray Conf., Plovdiv, Bulgaria, 13–26 Aug 1977.

B. L. Gotwols, D. G. Mitchell, and E. C. Roelof (APL) and W. M. Cronyn (Univ. of Iowa), "Power Spectra of Interplanetary Radio Scintillations Observed at 34.3 MHz," American Geophysical Union Meeting, San Francisco, 6–10 Dec 1976.

E. P. Gray, "A New Variational Approach to Scattering by Random Media or Rough Surfaces," Colloq., Commission F, URSI, La Baule, France, 2 May 1977.

———, "Scattering of a Surface Wave by a Submerged Sphere," APS Fluid Dynamics Meeting, Eugene, OR, 22–24 Nov 1976.

A. N. Jette and J. G. Parker, "Earth Surface Displacement Generated by Propagation of Acoustic Plane Waves Within Gas-Filled Buried Pipe (Theoretical)," Acoustic Society of America, State College, PA, 6–8 Jun 1977.

C. J. Johns (The Johns Hopkins Univ.), B. I. Blum (APL), and D. W. Simborg (The Johns Hopkins Univ.), "The Minirecord Approach to Continuity of Care for a Large Population of Ambulatory Patients," Third Illinois Conf. on Medical Information Systems, Chicago, 4–5 Nov 1976.

E. P. Keath, S. M. Krimigis, and E. C. Roelof, "Statistical Analysis of Magnetospheric Emission of >0.3 MeV Protons Observed by IMP-7 and IMP-8," American Geophysical Union Meeting, San Francisco, 6–10 Dec 1976.

R. J. Keenan and P. F. Bohn, "Hybrid Computer Handling Program—Prediction of Vehicle Dynamics," Mini-Conf. on Transportation, Univ. of Michigan, Ann Arbor, 20–22 Apr 1977.

E. Keppler and E. T. Sarris (Max-Planck Institute) and S. M. Krimigis (APL), "The Interplanetary Shock Wave Event of Nov. 1975 Observed by Helios-A and IMP-7, 8," American Geophysical Union Meeting, San Francisco, 6–10 Dec 1976.

E. Kirsch and E. T. Sarris (Max-Planck Institute), S. M. Krimigis (APL), R. P. Lepping (NASA Goddard), and T. P. Armstrong (Univ. of Kansas), "Evidence for a DC Electric Field in the Magnetotail from Observations of Oppositely Directed Anisotropies of Energetic Protons and Electrons," American Geophysical Union Meeting, San Francisco, 6–10 Dec 1976.

J. W. Kohl and S. M. Krimigis (APL), E. T. Sarris (Max-Planck Institute), and T. P. Armstrong (Univ. of Kansas), "On the Occurrence of High-Energy Proton ($E_p \geq 1.85$ MeV) and Electron ($E_e \geq 500$ keV) Bursts in the Magnetotail," American Geophysical Union Meeting, San Francisco, 6–10 Dec 1976.

S. M. Krimigis and E. C. Roelof (APL), E. T. Sarris (Max-Planck Institute), and T. P. Armstrong (Univ. of Kansas), "The Unusual Solar Particle Event of April 29, 1973," American Geophysical Union Meeting, San Francisco, 6–10 Dec 1976.

———, R. D. Zwickl, and J. W. Kohl (APL) and T. P. Armstrong (Univ. of Kansas), "The Quiet Time Low Energy Nucleon Spectrum During 1975," 15th International Cosmic Ray Conf., Plovdiv, Bulgaria, 13–26 Aug 1977.

R. E. Lenhard, Jr. (JHMI) and B. I. Blum (APL), "A Comprehensive Clinical Data System for an Oncology Center," American Society for Clinical Oncology, Denver, 18–21 May 1977.

M. G. Lotter (Univ. of Orange Free State, Republic of South Africa), H. N. Wagner, Jr. (Johns Hopkins School of Medicine), L. G. Knowles (APL), and K. H. Douglass and E. L. Nickoloff (Johns Hopkins School of Medicine), "Cardiac Function Evaluation with Radionuclides," Annual Congress, South African Association of Physicists in Medicine and Biology, Capetown, 7–10 Mar 1977.

———, ———, ———, ———, and ———, "Computers in Nuclear Medicine," Annual Congress, South African Association of Physicists in Medicine and Biology, Capetown, 7–10 Mar 1977.

R. L. McCally and C. B. Bargeron, "Intensity Correlation Spectroscopy: Application to Measurement of Continuous Distributions of Spherical Particles," American Physical Society, San Diego, 21–24 Mar 1977.

———, J. L. Cox (JHMI), and R. A. Farrell (APL), "The Effect of Intraocular Pressure on Stromal Structure," Association for Research in Vision and Ophthalmology, Sarasota, FL, 25–29 Apr 1977.

——— and R. A. Farrell, "Changes in Small Angle Light Scattering from Rabbit Cornea with Transcorneal Pressure," American Physical Society, San Diego, 21–24 Mar 1977.

——— and ———, "The Effect of Intraocular Pressure on Small-Angle Light Scattering from Rabbit Cornea," Cleveland Symp. on Macromolecules, Structure and Properties of Biopolymers, Case Western Reserve Univ., Cleveland, 11–15 Oct 1976. Also presented to Johns Hopkins Medical Association, Baltimore, 25 Feb 1977.

L. Monchick, "An Asymptotic Solution to the Chemically Induced Dynamic Electron Polarization (CIDEP) Problem," Statistical Physics Seminar, Univ. of Maryland, College Park, 6 Sep 1977. Also presented to Univ. of Erlangen-Nurnberg Department of Theoretical Physics, Erlangen-Nurnberg, West Germany, 30 Sep 1977.

———, "Kinetic Theory of Quantum State Diffusion," Third Washington-Area Statistical Physics Symp., Washington, DC, 23 Nov 1976.

———, "Some Recent Calculations on Helium HCl Collisions," Univ. of Leiden, The Netherlands, 21 Sep 1977.

K. Moorjani, "Competing Exchange Interactions in Solids," Institute of Theoretical Physics, Berlin, 5 Aug 1977.

———, "Disordered Magnetism," Institute of Theoretical Physics, Berlin, 20 Jul 1977.

———, "Effective Field Theories in Disordered Magnetic Systems," Catholic Univ. of America Colloq. Series on Properties of Amorphous Magnetic Materials, Washington, DC, 13 Jan 1977.

———, "Spin Glasses," Institute of Theoretical Physics, Berlin, 27 Jul 1977.

J. C. Murphy, "Active Acoustic Detection of Leaks in Underground Natural Gas Distribution Lines (Theoretical)," Hazard Prevention Symp., Institute of Gas Technology, Chicago, 28 Jun 1977.

———, "Photoacoustic Spectroscopy," Wake Forest Univ. Seminar, Winston-Salem, NC, 14 Apr 1977.

J. T. Nolte and A. S. Krieger (American Science and Engineering) and E. C. Roelof and R. E. Gold (APL), "High Coronal Structure of High Velocity Solar Wind Stream Sources," American Geophysical Union Meeting, San Francisco, 6–10 Dec 1976.

J. B. Oakes (APL) and J. C. Aller (National Science Foundation), "Present Status and Future Prospects of Accreditation, Certification and Licensing in Clinical Engineering," AAMI Twelfth Annual Meeting, San Francisco, 13–17 Mar 1977.

V. O'Brien, "Convective Field Theory to Predict Dialysis Efficiency," 29th ACEMB, Boston, 6–10 Nov 1976.

———, "Convective Transport in Non-Circular Ducts," APS Fluid Dynamics Meeting, Eugene, OR, 22–24 Nov 1976.

———, "Pulsatile Flow Through Stenosed Arteries," ASME Summer Meeting, New Haven, CT, 15–17 Jun 1977.

J. G. Parker, "Active Acoustic Detection of Leaks in Underground Natural Gas Distribution Lines (Experimental)," Hazard Prevention Symp., Institute of Gas Technology, Chicago, 28 Jun 1977.

D. P. Peletier, S. A. Gary, and A. F. Hogrefe, "Mariner-Jupiter-Saturn Low Energy Charged Particle Experiment," 1976 Nuclear Science Symp., New Orleans, 20–22 Oct 1976.

W. K. Peterson and J. P. Doering (The Johns Hopkins Univ.) and T. A. Potemra and C. O. Bostrom (APL), "Characteristics of 1–500 eV Electrons Observed in the Earth's Thermosphere from the Photoelectron Spectrometer Experiment on the Atmosphere Explorer Satellites," NATO Advanced Study Institute on Dynamical and Chemical Coupling of Neutral and Ionized Atmosphere, Norway, 12–22 Apr 1977.

T. A. Potemra, "Large-Scale Characteristics of Field-Aligned Currents Determined from the Triad Magnetometer Experiment," NATO Advanced Study Institute on Dynamical and Chemical Coupling of Neutral and Ionized Atmosphere, Norway, 12–22 Apr 1977.

S. Qureshi, H. N. Wagner, Jr., and P. O. Alderson (Johns Hopkins School of Medicine), M. G. Lotter (Univ. of Orange Free State, Republic of South Africa), K. H. Douglass (Johns Hopkins School of Medicine), and L. G. Knowles (APL), "Characteristics of Left Ventricular Time-Activity Curves in Patients with Heart Disease," Twenty-fourth Annual Meeting, Society of Nuclear Medicine, Chicago, 21–24 Jun 1977.

D. Rabenhorst, "Modern Flywheel Technology," Graduate Seminar, Howard Univ., Washington, DC, 15 Oct 1976.

R. Reinhard (European Space and Technology Research Center, The Netherlands) and R. E. Gold, E. P. Keath, and E. C. Roelof (APL), "Coronal Control of Plasma and Energetic Particle Emission from the April 10, 1969 Solar Flare," American Geophysical Union Meeting, San Francisco, 6–10 Dec 1976.

E. C. Roelof and E. P. Keath (APL) and R. P. Lepping (NASA Goddard), "Magnetic Signature of Large Proton Bursts Observed by IMP-7 Near the Plasma Sheet at 35 R_e," American Geophysical Union Meeting, San Francisco, 6–10 Dec 1976.

——— and S. M. Krimigis, "Solar Energetic Particles Below 10 MeV," XXth COSPAR Meeting, Tel Aviv, 7–18 Jun 1977.

J. C. W. Rogers, "Embedding Techniques for Free Boundary Problems," Numerical Analysis Seminar, Los Alamos, NM, 17 Jun 1977. Also presented at Partial Differential Equations Seminar, Univ. of Texas, 23 Sep 1977.

———, "Numerical Solution of Free Boundary Problems by Approximation of Semigroups of Nonlinear Operators," Symp. on Moving Boundary Problems, Gatlinburg, TN, 26–28 Sep 1977.

N. Rubinstein and W. C. Caywood, "Standard Missile Boost Phase Vibration Environments Defined from Static Tests on the Mk 12 Booster," 14th JANNAF Combustion Meeting, U.S. Air Force Academy, Colorado Springs, CO, Aug 1977.

N. A. Saflekos and T. A. Potemra, "Small-Scale Transverse Magnetic Variations in the Polar Regions from Triad," American Geophysical Union Meeting, San Francisco, 6–10 Dec 1976.

E. T. Sarris and D. J. Williams (Max-Planck Institute), S. M. Krimigis (APL), and L. A. Frank (Univ. of Iowa), "Correlative Studies of Energic Particles and Hot Plasmas During Magnetospheric Particle Bursts," American Geophysical Union Meeting, San Francisco, 6–10 Dec 1976.

F. G. Satkiewicz, "Relative Yields of Positive Ions Sputtered from Several Glasses," ASMS 25th Annual Conf. on Mass Spectrometry and Allied Topics, Washington, DC, 30 May—1 Jun 1977.

———, "Sputter Ion Source Mass Spectrometry of Several Glasses," National Bureau of Standards Meeting, Gaithersburg, MD, 9 Mar 1977.

V. G. Sigillito, "Bounds for Eigenvalues of Elliptic Applications," Applied Mathematics Colloq., Center for Applied Mathematics, Cornell Univ., Ithaca, NY, 1 Apr 1977.

D. M. Silver, "Electronic Structure of Molecules Using Many-Body Perturbation Theory," Chemistry Seminar, Univ. of Maryland, College Park, 3 Nov 1976.

———, "Interaction Potentials Between Closed-Shell Atoms and Molecules," Sixth Canadian Symp. on Theoretical Chemistry, New Brunswick, Canada, 19–25 Jun 1977.

D. W. Stowe, "An Electronically Steered Parametric Transducer with Variable Frequency," 92nd Acoustical Society Meeting, San Diego, 15–19 Nov 1976.

B. E. Tossman, "A Time Optimal Geomagnetic Maneuvering Technique for Orbit Correction Thrust Vectoring," 12th Symp. on Space Technology and Science, Tokyo, 17 May 1977.

H. N. Wagner, Jr. (Johns Hopkins School of Medicine), M. G. Lotter (Univ. of Orange Free State, Republic of South Africa), L. G. Knowles (APL), and T. K. Natarajan (Johns Hopkins School of Medicine), "Computer-Assisted Cinematic Displays in Nuclear Medicine," Twenty-fourth Annual Meeting, Society of Nuclear Medicine, Chicago, 21–24 Jun 1977. Also presented at Informatek European Users Group Meeting, Clermont-Ferrand, France, 19–21 May 1977.

D. J. Williams (NOAA/Boulder) and R. E. Gold and E. C. Roelof (APL), "Intense Fluxes of $>$ 50 keV Magnetospheric Protons Observed in Interplanetary Space Following an SSC," American Geophysical Union Meeting, San Francisco, 6–10 Dec 1976.

S. Wilson (Daresbury Laboratories, Warrington, England) and D. M. Silver and R. A. Farrell (APL), "Special Invariance Properties of the [N + 1/N] Approximants in Rayleigh-Schrodinger Perturbation Theory," American Physical Society, San Diego, 21–24 Mar 1977.

R. D. Zwickl, S. M. Krimigis, R. E. Gold, and E. C. Roelof (APL) and T. P. Armstrong (Univ. of Kansas), "Observations of Enhanced Abundances of He Through Fe Nuclei During Solar Flare Events," 15th International Cosmic Ray Conf., Plovdiv, Bulgaria, 13–26 Aug 1977.

——— and W. R. Webber (Univ. of New Hampshire), "The Interplanetary Scattering Mean Free Path from 1 to 3 $\times$ 10^3 MV," 15th International Cosmic Ray Conf., Plovdiv, Bulgaria, 13–26 Aug 1977.

AUTHOR INDEX

AUTHOR INDEX